Master of Science Thesis

The 3D separation behaviour of a micro-ramp controlled oblique shock-wave reflection

An experimental investigation

S Nayak Kallarbail

May 3, 2016

Aerodynamics

TU Delft

Faculty of Aerospace Engineering

Delft University of Technology

The 3D separation behaviour of a micro-ramp controlled oblique shock-wave reflection

An experimental investigation

Master of Science Thesis

For obtaining the degree of Master of Science in Aerospace Engineering
at Delft University of Technology

S Nayak Kallarbail

May 3, 2016

Faculty of Aerospace Engineering · Delft University of Technology

Delft University of Technology

DELFT UNIVERSITY OF TECHNOLOGY
DEPARTMENT OF AERODYNAMICS

The undersigned hereby certify that they have read and recommend to the Faculty of Aerospace Engineering for acceptance the thesis entitled **"The 3D separation behaviour of a micro-ramp controlled oblique shock-wave reflection"** by **S Nayak Kallarbail** in fulfillment of the requirements for the degree of **Master of Science**.

Dated: May 3, 2016

Supervisors:

Dr. ir. B. W. van Oudheusden

Dr. ir. F. F. J. Schrijer

Ir. R. H. M. Giepman

Dr. ir. A. Bohlin

".. you cannot learn a thing you think you know."

Dawn, Poets of the Fall

Abstract

Oblique Shock-Wave Reflections or Shock Wave-Boundary Layer interactions (SWBLI) are complex phenomena which commonly occur in high speed flight. SWBLIs can have catastrophic consequences on the aircraft due to shock induced separation and unsteadiness of the interaction. These adverse effects can be mitigated by manipulating the boundary layer, either before it enters the interaction, or in the interaction region itself.

Micro-ramp vortex generators or micro-ramps have been identified as promising boundary layer control methods in supersonic engine intakes. They are small ramp devices with heights less than the boundary layer thickness (typically 50% of boundary layer thickness). It is known that, micro-ramps generate a counter-rotating vortex pair, due to which a fuller and more separation resistant boundary layer is obtained upstream of the SWBLI. They successfully prevent separation at their centrelines and their effectiveness reduces away from their centrelines. Since a micro-ramp generates a highly 3D flow, the main aim of this study is to quantify the 3D velocity fields in the micro-ramp controlled interaction. Further, this study is motivated by the fundamental question whether the total volume of separated flow in the interaction is reduced by employing micro-ramp control.

The results from tomographic-PIV experiments confirm that micro-ramp control has a beneficial effect on SWBLI in reducing separation. For the experimental conditions and micro-ramp geometry used in this thesis, the total volume of separated flow is reduced to 31% compared to the interaction without control. Further, the maximum separation probability is also reduced by using micro-ramp control, with the largest reductions occurring along the micro-ramp centreline. Additionally, the findings indicate that a moderately negative correlation coefficient exists between separation bubble sizes at spanwise stations on either side of the micro-ramp centreline. This indicates that the separation bubble size at a particular spanwise location is coupled to its size at another spanwise location in the micro-ramp controlled interaction.

Along with the 3D velocity fields in the interaction, these results extend the knowledge on micro-ramp control significantly. It is conjectured that the spanwise correlation between the separation bubble sizes may play an important role while using micro-ramp arrays for applications in supersonic engine intakes. Therefore, an immediate possible investigation would involve studies of 3D effects of micro-ramp array control and the spanwise correlation of the separation bubble sizes.

Acknowledgement

First of all, I would like to thank Ir. R. H. M. Giepman for his guidance and patience during the course of this project. I would like to thank Dr. ir. B. W. van Oudheusden and Dr. ir. F. F. J. Schrijer for their advices and feedbacks on my results and reports. I would like to thank Dr. ir. A. Bohlin for taking the time to read my thesis and for being on my defense committee.

I am thankful to Dr. Kyle Lynch for his extensive support during the tomo-PIV experiments and data reduction. Thanks to Qingqing for her advices on the tomo-PIV data reduction. I express my gratitude to Frits Donker Duyvis, Peter Duyndam and Nico van Beek for their support during the experiments. I am especially thankful to Peter Duyndam, for his ever so cheerful attitude which is very inspiring.

I am thankful to Dhaarini, Sudarshan, Namrata, Nidhi, Disha, Swati and Lalitha for encouraging me especially in the last three years, irrespective of the many different time zones and bustle of work; and most importantly for being such wonderful friends. My stay in Delft has taught me the importance of company of highly inspiring and motivated people. Hence, I am thankful to Neola, Sudarshan and Arpan for their infectious optimism and determination. I have had the pleasure of studying with some wonderful people: Caddie, Luis, Karl, Eelco, I have learnt a lot from you guys! I greatly appreciate the time invested by Neola, Sudarshan and Samprajani in proof reading various parts of this report. I am grateful to Prasanna for her company during the late night report writing sessions in library.

Because of the people I have met from the many different walks of life here in the Netherlands, I feel truly fortunate and blessed to have had the opportunity to education. Through this experience in Delft, I have rediscovered my love for sketching and painting, and this has been a major milestone. Finally and most importantly, I am grateful for my family, especially my parents and sister; for their belief in me, their unconditional love and numerous sacrifices.

Shruthi Nayak
Delft, The Netherlands
May 3, 2016

Table of Contents

Nomenclature

List of Abbreviations

DEHS	Di-ethyl-hexyl-sebacat
FOV	Field of view
K-H	Kelvin-Helmholtz
LES	Large Eddy Simulation
LDA	Laser Doppler anemometry
PIV	Particle image velocimetry
SNR	Signal to Noise ratio
SWBLI	Shock wave-turbulent boundary layer interaction
TiO_2	Titanium dioxide
Tomo-PIV	Tomographic-PIV

List of Symbols

δ	Boundary layer thickness	[mm]
δ_i^*	Incompressible displacement thickness	[mm]
θ	Flow deflection angle (Micro-ramp's ramp angle)	[$^\circ$]
θ_i	Incompressible momentum thickness	[mm]
κ	Von Kármán constant	-
μ	Dynamic viscosity	[Ns/m^2]
ν	Kinematic viscosity	[m^2/s]
ξ	Dimensionless pressure gradient	-
ρ_w	Density at the wall	[kg/m^3]

τ_w	Wall shear stress	[N/m^2]
υ^*, u_τ	Wall-friction velocity	[m/s]
A_p	Semi angle of micro-ramp	[°]
B	Law of the wall intercept constant	-
c	Chord of the micro-ramp	[mm]
c_p	Specific heat capacity at constant pressure	[J/kgK]
C_f	Skin friction coefficient	-
h	Height of the micro-ramp	[mm]
H_i	Incompressible Shape factor	-
M_∞	Free stream Mach number	-
p_0	Total pressure in the stagnation chamber	[N/m^2]
P_{sep}	Separation probability	-
$Re_{\delta*}$	Reynolds number based on displacement thickness	-
Re_δ	Reynolds number based on boundary layer thickness	-
Re_∞	Unit Reynolds number	m^{-1}
Re_θ	Reynolds number based on momentum thickness	-
s	Spacing between two micro-ramp centrelines	[mm]
	Stokes number	-
T_0	Total temperature	[K]
T_e	Temperature in free stream	[K]
T_{aw}	Adiabatic wall temperature	[K]
$\overline{u}$	Local streamwise velocity component	[m/s]
u_{eq}	van Driest effective velocity	[m/s]
u^+, y^+	Law of the wall variables	-
U_∞	Free stream velocity	[m/s]
x	Streamwise coordinate	-
x_{MR}, x_p, d	Distance of micro-ramp from inviscid shock impingement location	[mm]
y	Wall Normal coordinate	-
z	Spanwise coordinate	-

Chapter 1

Introduction

Oblique Shock-wave Reflections or Shock-wave boundary layer interactions are interesting yet perplexing phenomena that occur commonly in high speed flight. Shock waves occur in many situations ranging from transonic wings, internal components of aircrafts like engine intakes and fast rotating turbine/ compressor blades to hypersonic vehicles. When these shock waves interact with the boundary layer, a complex multi-shock system is formed. Such Shock-wave boundary layer interactions or SWBLIs may have catastrophic consequences in the systems where they occur. The type of interaction considered in this thesis is that which typically takes place inside high-speed engine intakes.

Figure 1.1: Inlet spike of a Pratt & Whitney J-58 engine used on the SR-71 Blackbird [2].

High-speed engine intakes have to be designed carefully since turbojet compressors cannot handle supersonic flows [11]. The shock waves associated with supersonic speeds can cause dangerous vibrations or damage the compressor blades resulting in an engine failure. Hence, it is necessary to decelerate the flow to subsonic speeds before it enters the engine. Subsonic

flow can be achieved by using a mixed compression intake, where a series of oblique shock waves and a terminal normal shock wave are used to decelerate the supersonic flow to subsonic Mach numbers. The classic example of such a mixed compression intake is seen on the Pratt & Whitney J58 engine on the SR-71 Blackbird shown in figure (1.1). The inlet of the SR-71 consists of a cone-shaped inlet centre-body or spike which can be moved towards or away from the engine. By moving the inlet spike, the terminal shock wave can be repositioned for optimum efficiency during different flight conditions.

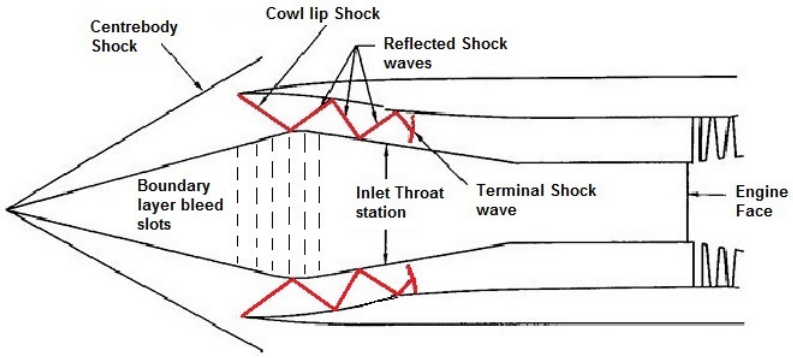

Figure 1.2: Inlet of SR-71 Blackbird showing shock reflections and boundary layer bleed system [3]

When the flow enters the intake, it experiences an abrupt change in flow angle and an oblique shock wave is formed. This oblique shock wave is reflected from the walls of the intake multiple times as shown in figure (1.2) and the flow turns subsonic. These multiple shock reflections pose a critical problem to performance since the shock waves interact with the turbulent boundary layer growing on the walls of the intake and the spike. Depending on the stability of the boundary layer and the strength of the shock wave, the boundary layer may separate due to the interaction.

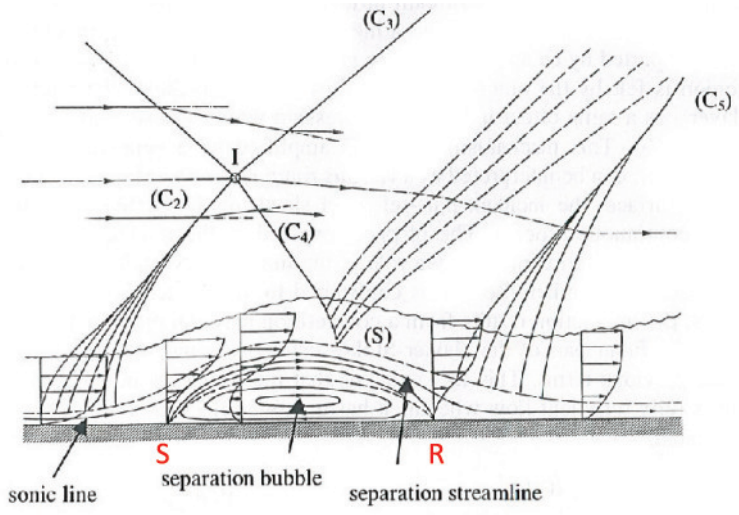

Figure 1.3: Shock-wave boundary layer interaction involving separation [10]

A typical shock-wave boundary layer interaction involving separation is shown in figure (1.3). A series of shock waves and a separation bubble form the principal features in the interaction. In figure (1.3), the incident shock wave is represented by 'C4' and curves as it penetrates through the boundary layer. The information of the adverse pressure gradient is transmitted to flow upstream through the subsonic part of the boundary layer. Therefore, the boundary layer separates upstream of the point where the inviscid incident shock would impinge on the wall. A bubble of recirculating fluid called as the separation bubble is formed between the separation point S and the re-attachment point R. The separated flow re-attaches and a re-attachment shock wave is formed.

Further, a shock-wave boundary layer interaction with separation is inherently unstable. The unsteady behaviour of the shock-wave boundary layer interaction exposes the compressor blades to fluctuating pressure and thermal loads which can lead to vibrations and structural failure [38]. Further, shock instability is a well known cause for air intake buzz which leads to large fluctuations in the thrust output [38]. In the worst case scenario, this can lead to an engine unstart, which has catastrophic consequences on the flight dynamics of the aircraft.

To prevent such undesirable effects of SWBLI, boundary layer control is employed. The conventional means of boundary layer control is through boundary layer bleed. Such a boundary layer bleed system is employed in the SR-71 intake and slots for the bleed mechanism on the inlet spike can be seen in figure (1.2). The low momentum fluid close to the wall is bled through these slots, and is vented overboard. The new boundary layer is much fuller and less prone to separation [11]. Additional instrumentation/ducting is required for the operation of the bleed mechanism. Importantly, the mass flow that is vented through the bleed mechanism is not typically re-injected anywhere and thus reduces the engine mass flow rate. This necessitates an increase in the frontal area of the engine, increasing the weight and drag of the aircraft [38]. Therefore, passive control devices such as micro-ramp vortex generators are a promising alternative to boundary layer bleed.

Micro-ramp vortex generators (or micro-ramps) are small wedge like ramp devices that are based on the same principle as conventional vortex generators. A typical micro-ramp vortex generator is shown in figure (1.4). Since these vortex generators feature a height smaller than the boundary layer thickness they are called as micro-ramp vortex generators (also sub-boundary layer or low-profile vortex generators). These devices improve the separation resistance of the boundary layer by generating vortices. These vortices enhance mixing between the boundary layer and the free stream, and generate a fuller boundary layer velocity profile [5].

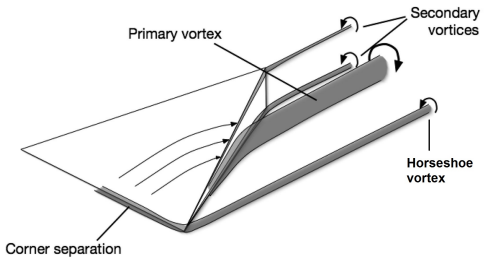

Figure 1.4: Typical micro-ramp vortex generator from Babinsky *et al* [6].

Micro-ramps are simple and low weight devices, however they pose a potential disadvantage due to their parasitic drag penalty at off-design conditions [5]. However, when compared to conventional vortex generators micro-ramps have some inherent advantages. Since they are inside the boundary layer and hence immersed in a fluid of lower dynamic pressure, they are associated with lower skin friction drag compared to conventional vortex generators [5]. Additionally, the vortices generated by the micro-vortex generators do not lift off from the wall very quickly and remain inside the boundary layer for a longer streamwise distance compared to conventional vortex generators [6]. Hence they bring about mixing and energize the boundary layer over a longer region.

Before micro-ramps make their way into intakes of jet fighters for practical application, it is necessary to clearly understand the micro-ramp fluid physics. To this end, many research efforts have been undertaken and many are in progress. The initial motivation for the study of micro ramps and their usefulness in supersonic intakes was provided by Anderson *et al* [4], who determined an optimal micro-ramp geometry [4]. Micro-ramp vortex generators are mounted upstream of the interaction such that boundary layer quality is improved before it enters the interaction.

Surface oil flow patterns have helped to identify that a pair of counter-rotating vortices form the principal flow features in micro-ramp control [6]. Due to their counter-rotating action, these vortices entrain higher momentum fluid from the outer parts of the boundary layer/freestrem and transport the higher momentum fluid to the near wall regions [6]. This results in a fuller boundary layer velocity profile which is more separation resistant. Due to the action of the micro-ramp, the shock induced separation bubble along its centreline is completely eliminated [19]. However, while moving away from the micro-ramp centreline, the effectiveness of micro-ramp reduces and separated flow regions are observed [19]. Thus the micro-ramp breaks up the separation bubble into smaller cells and creates a spanwise modulation of the separation bubble. Since the reflected shock unsteadiness is associated with separation bubble, micro-ramps also reduce the reflected shock unsteadiness. [19].

In conclusion, micro-ramps create a spanwise modulation of the flow and the flow generated by a micro-ramp is highly three-dimensional. However, existing literature is confined only to two-dimensional studies. Though numerical methods such as Large Eddy Simulations (LES) have been used to study the 3D features of the present problem, they are limited by their computing time. However, recent developments in Particle Image velocimetry (PIV) have demonstrated the successful application of Tomographic-PIV for three-dimensional studies of supersonic flows [35]. Given these developments in the field of experimental aerodynamics, substantial opportunity lies in determining the three-dimensional flow organization of a micro-ramp controlled oblique shock reflection by a tomographic-PIV investigation.

1.1 Thesis Aim and Research questions

The main aim of thesis project is to obtain the three-dimensional flow organization in the interaction region. The three-dimensional effects of a micro-ramp in the interaction region

will be investigated and this will provide useful insights into the physics of micro-ramp flow control. To the knowledge of the author, no such three-dimensional information is currently available and hence this thesis extends the available knowledge significantly.

The main of this thesis has been achieved by setting a series of research questions as follows:

- Does the total volume of separated flow decrease in a micro-ramp controlled interaction compared to the uncontrolled interaction?
- Does the separation probability decrease in a micro-ramp controlled interaction compared to the uncontrolled interaction?
- Is the size of the separation bubble at one spanwise location coupled to its size at another spanwise location?

An experimental methodology is followed to answer these research questions. Tomographic-PIV is used as the primary tool to study the micro-ramp controlled interaction region. Supplementary surface oil flow visualizations and schlieren visualizations are used for understanding the global flow features of the interaction.

Using these experimental techniques, the baseline configuration: SWBLI without micro-ramp control or uncontrolled interaction is studied first. This is followed by SWBLI controlled by a single micro-ramp or micro-ramp controlled interaction.

1.2 Thesis outline

This document mainly describes the procedure and results from the experimental investigations performed as a part of this thesis project, and is divided into nine chapters including this introductory chapter.

Chapter 2 provides a summary of relevant work from literature. This includes a discussion on turbulent boundary layers and shock-wave turbulent boundary layer interactions. The present knowledge on working principle and flow features generated by a micro-ramp are reviewed and summarized.

Chapter 3 provides a detailed discussion on the experimental techniques used in the present study. The experimental set-up and test matrices of the investigation form the main parts in this chapter.

In Chapter 4, the undisturbed boundary layer or boundary layer without shock wave and micro-ramp control is characterized.

Chapter 5 is dedicated to the surface oil flow patterns of a micro-ramp. The results from the surface oil flow visualization of a micro-ramp to study its flow features are presented. The oil flow patterns of micro-ramps of different geometries are also included in this chapter.

Chapter 6 is devoted to the discussion of the global flow features of the uncontrolled and micro-ramp controlled interaction. The results from surface oil flow and schlieren visualizations are discussed for both the interactions. Further, surface oil flow visualizations of micro-ramp arrays: single-row array and double-row staggered array are also presented.

Chapter 7 mainly discusses the mean flow organization of the uncontrolled and micro-ramp controlled interaction. The micro-ramp effects on the interaction are investigated through wall parallel and streamwise planes. Further, volumetric representation of both the interactions is also provided.

Chapter 8 focusses on the statistical analyses performed to study the effect of the micro-ramp on the interaction. The probability of separation, area of separated flow, and the total volume of separated flow are discussed in this chapter. This Chapter mainly answers the research questions.

Chapter 9 presents the conclusions of this thesis project. The scope for future work is also provided in this chapter.

This is followed by the appendices. Appendix A describes the steps taken to improve the PIV seeding conditions in the wind tunnel's test section. This involves the design of a new seeding rake to distribute seeding particles and a description of experiments to optimize the illumination and seeding in the wind tunnel.

Appendix B details the exact steps carried out for the tomographic-PIV data reduction. Appendix C deals with validation of the tomographic-PIV experiments. It provides a comparison between the velocity profiles of the present tomographic-PIV study with the planar-PIV results of Giepman et al. [19], for the uncontrolled and single micro-ramp controlled interactions.

Chapter 2

Literature Review

2.1 Introduction

This chapter primarily summarizes the relevant literature articles that are necessary to understand the working principle of micro-ramps, and the effects of a micro-ramp on shock wave-boundary layer interaction. Additionally, fundamental concepts about turbulent boundary layers and shock wave-boundary interactions are reviewed.

The first section (2.2) presents the basic properties of a compressible turbulent boundary layer. Section (2.3) presents a discussion on the features of an oblique shock reflection (or interaction of an oblique shock wave and a turbulent boundary layer), resulting in shock induced separation. The unsteadiness of the reflected shock wave and the mechanisms that are believed to cause such unsteadiness are also briefly discussed in this section.

In section (2.4), the working principle of micro-ramp vortex generators and micro-ramp flow features are discussed. The application of micro-ramps as boundary layer control devices are discussed.

2.2 Turbulent Boundary Layer

Turbulent flow is characterized by high unsteady, seemingly random motion and fluctuating velocities. A turbulent boundary layer is marked by unsteady mixing of the flow on a macroscopic scale which causes rapid diffusion of mass, momentum and energy. This is due to the presence of a wide spectrum of turbulent eddies in the boundary layer. Experimental observation shows that, a turbulent boundary layer profile has a 'composite' structure. The viscosity dependent region close to the wall and the turbulent stress dependent region away from the wall need different length scales. Therefore the turbulent boundary layer velocity

profile consists of an inner layer and an outer layer along with an intermediate overlap region between the two. The inner layer, outer layer and the overlap region are shown in figure (2.1).

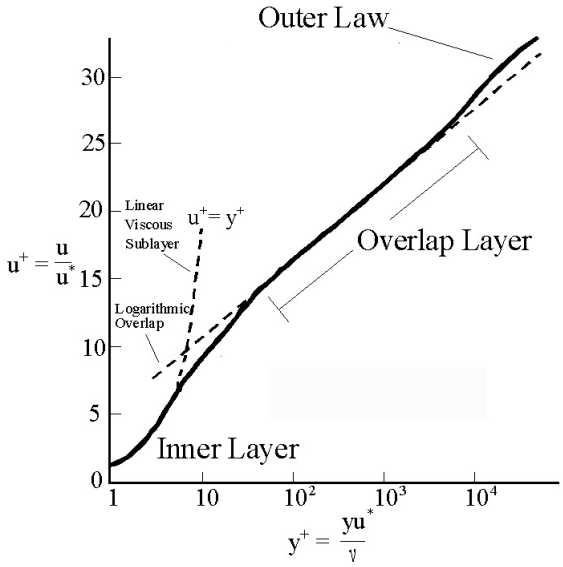

Figure 2.1: Inner layer, outer layer and overlap layer of a turbulent boundary layer in terms of inner variables [30].

- Inner layer: The flow in the inner layer depends on wall shear stress, fluid properties and the distance y from the wall but is not affected by the free stream parameters [46]. The inner law or 'law of the wall' can be written in the non-dimensional form as given by equation (2.1) using the inner variables defined as u^+ and y^+.

$$\frac{\overline{u}}{\upsilon^*} = f(\frac{y\upsilon^*}{\nu})$$

$$u^+ = f(y^+) \tag{2.1}$$

where $\overline{u}$ is the local velocity, ν is the viscosity and y is the wall normal co-ordinate. υ^* or u_τ is called the wall-friction velocity and is given by:

$$\upsilon^* = u_\tau = \left(\frac{\tau_w}{\rho_w}\right)^{1/2} \tag{2.2}$$

with τ_w being the wall shear stress and ρ_w being the density at the wall. The inner layer is further divided into:

1. Viscous sublayer $y^+ \leq 5$: This layer is dominated by viscous shear and a linear velocity profile exists in this region.

$$u^+ = y^+$$

2. Buffer layer $5 \leq y^+ \leq 30$: In this intermediate region, both the viscous and turbulent shear are relevant

3. Overlap layer or Logarithmic layer $y^+ \geq 30$: The overlap layer is dominated by turbulent stress and logarithmic law is valid in this region, therefore it is also called the 'Logarithmic layer'. The velocity profile in the overlap region can be written in terms of inner variables and outer variables as equation (2.3) and equation (2.4) respectively.

$$u^+ = \frac{1}{\kappa}\, ln\, y^+ + B \tag{2.3}$$

$$\frac{U_\infty - \overline{u}}{\upsilon^*} = -\frac{1}{\kappa}\, ln\, \frac{y}{\delta} + A \tag{2.4}$$

where U_∞ is the freestream velocity, δ is the boundary layer thickness, A is a constant which varies primarily with pressure gradient ξ and other flow parametrs, $\kappa = 0.41$ is the Von Kármán constant, B is the law of the wall intercept constant $B = 5.0$

- Outer layer: In the outer layer the turbulent (eddy) shear dominates. For the outer layer the wall acts merely as a source of retardation in reducing the local velocity below the free stream velocity, independent of viscosity μ but dependent on the wall shear stress, layer thickness and free stream pressure gradient [46]. The outer law is called the velocity defect law and can be written in the non-dimensional form as:

$$\frac{U_\infty - \overline{u}}{\upsilon^*} = g(\frac{y}{\delta}, \xi) \tag{2.5}$$

where $(U_\infty - \overline{u})$ is the velocity defect. At any position x the defect shape $g(y/\delta)$ will depend on the local pressure gradient ξ which is given by:

$$\xi = \frac{\delta}{\tau_w}\frac{dp_e}{dx}$$

where $\frac{dp_e}{dx}$ is the pressure gradient in the x direction.

For a compressible turbulent boundary layer, the Skin friction coefficient C_f can be determined using the law of the wall and the van Driest effective velocity concept. Van Driest defined an effective velocity u_{eq} given by:

$$u_{eq} = \frac{U_\infty}{a}\Big(sin^{-1}\frac{a\overline{u}}{U_\infty}\Big) = u_\tau\Big(\frac{1}{\kappa}y^+ + B\Big) \tag{2.6}$$

where $\overline{u}$ is the mean velocity in the boundary layer, κ and B are near constants discussed earlier . For adiabatic walls, a is given by:

$$a = \sqrt{\Big(1 - \frac{T_\infty}{T_{aw}}\Big)} \tag{2.7}$$

where T_∞ is the temperature in the freestream and T_{aw} is the adiabatic wall temperature. The adiabatic wall temperature is calculated as :

$$T_{aw} = T_\infty - r\frac{U_\infty^2}{2c_p} \tag{2.8}$$

where r = 0.89 is the recovery factor and c_p is the specific heat of the gas at constant pressure. The right hand side in equation (2.6) is the incompressible law of the wall and the left side is the effective velocity. From this the wall friction velocity can be determined. Using the wall friction velocity u_τ, the skin friction coefficient can be calculated as:

$$C_f = \frac{u_\tau^2 \rho_w}{\frac{1}{2}\rho_\infty U_\infty^2} \tag{2.9}$$

2.2.1 Boundary layer integral parameters

The turbulent boundary layer can be characterized by boundary layer properties such as: displacement thickness δ^*, momentum thickness θ and shape factor H.

Boundary layer thickness δ is defined as the distance from the wall where the velocity reaches 99% of the free stream velocity. The displacement thickness is the distance by which a surface needs to be moved away from a reference plane in inviscid flow, such that the same flow rate is obtained as in case of the real viscous flow. The compressible displacement thickness (δ^*) and incompressible displacement thickness (δ^*_{inc}) are calculated as:

$$\delta^* = \int_0^\infty \Big(1 - \frac{\rho u}{\rho_\infty U_\infty}\Big) dy \qquad\qquad \delta^*_{inc} = \int_0^\infty \Big(1 - \frac{u}{U_\infty}\Big) dy \tag{2.10}$$

where ρ is density in the boundary layer and ρ_∞ is the density in the freestream.

The momentum thickness is the distance by which a surface needs to be moved parallel to itself and towards the reference plane in inviscid flow, such that the same momentum is obtained as between the surface and the reference plane in real viscous flow. The compressible momentum thickness (θ) and incompressible momentum thickness (θ_{inc}) can be calculated as:

$$\theta = \int_0^\infty \frac{\rho u}{\rho_\infty U_\infty}\Big(1 - \frac{\rho u}{\rho_\infty U_\infty}\Big) dy \qquad\qquad \theta_{inc} = \int_0^\infty \frac{u}{U_\infty}\Big(1 - \frac{u}{U_\infty}\Big) dy \tag{2.11}$$

From this, the incompressible shape factor H_i can be calculated as the ratio of displacement thickness to momentum thickness.

$$H_i = \frac{\delta^*_{inc}}{\theta_{inc}} \tag{2.12}$$

The shape factor H_i indicates the fullness of a boundary layer and H_i = 1.3 - 1.4 for a fully turbulent boundary layer.

2.3 Shock wave - Boundary Layer interaction

The inviscid picture of an oblique shock reflection is shown in figure (2.2). When realities of a viscous flow is considered i.e the boundary layer, this inviscid shock reflection is replaced

by a highly complex system of shock waves. The following paragraphs provide a discussion of such shock wave-boundary layer interactions with shock induced separation and its associated detrimental characteristics.

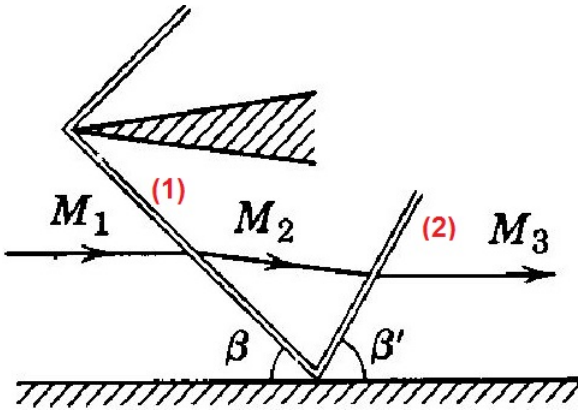

Figure 2.2: Inviscid Oblique shock reflection, (1) Incident shock wave (2) Reflected shock wave [27]

2.3.1 Shock Induced separation

The interaction resulting from an oblique shock reflection from a turbulent boundary layer is shown in figure (2.3). C_1 is the incident shock wave and its presence is felt upstream of the inviscid shock impingement location. This is due to the information of pressure rise being transmitted upstream through the subsonic part of the boundary layer [10]. Because of the dilatation of the subsonic region of the boundary layer, compression waves form and coalesce together forming the reflected shock C_2. The retardation due to the incident shock wave is larger in the inner part of the boundary layer (due to lower momentum). Therefore, the flow may be pushed in the upstream direction due to the adverse pressure gradient, leading to the formation of a separated region.

This separation process is basically a 'free interaction process' which results due to a local self-induced interaction between the boundary layer and the outer inviscid free-stream [9]. Therefore, it is independent of the downstream conditions and in particular the intensity of the incident shock wave, the pressure rise at separation $\triangle p_1$ being only a function of the incoming flow.

In figure (2.3), 'S' indicates the separation point and 'R' the re-attachment point. A detached shear layer emanates from the separation point S. A bubble of recirculating fluid, known as the 'separation bubble' exists between these two points bounded by the wall and the dividing streamline indicated by '(S)' . Due to the mixing between the detached shear layer and the outer high speed flow, energy is transferred from the outer high speed flow to the separated region. Due to this the local velocity along the dividing streamline increases with streamwise development leading to the commencement of the reattachment process [10]. The transmitted

shock wave C_3 penetrates into the viscous separated flow as C_4 and is reflected as an expansion wave. Due to this the flow is turned towards the wall where it re-attaches. The dividing streamline is decelerated and stagnates at R forming compression waves. The compression waves coalesce together to form the reattachment shock C_5.

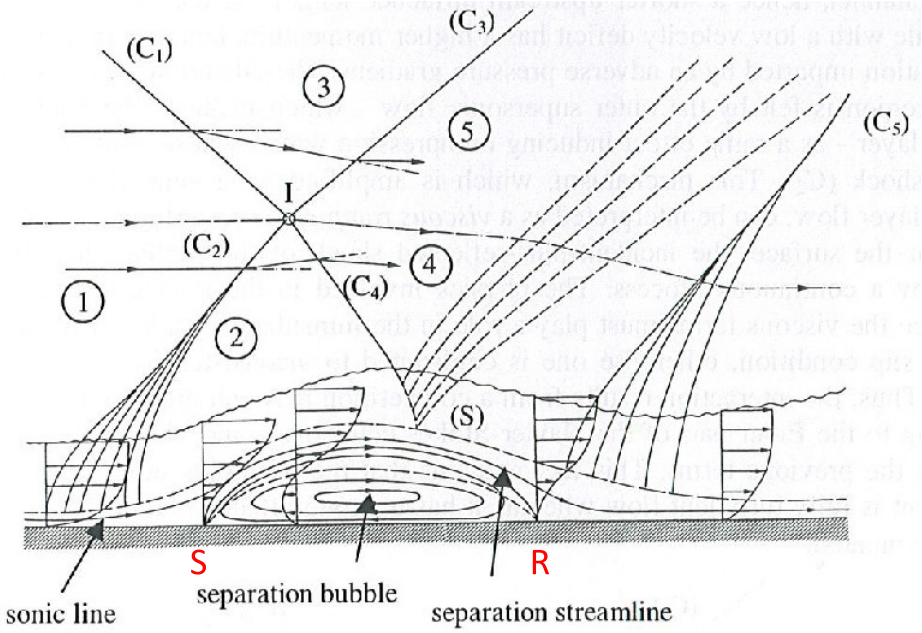

Figure 2.3: Physical features of an incident SWTBLI with separation based on Delery and Bur [10].

The pressure rise $\triangle p$ due to the shock reflection is thus divided into a first compression $\triangle p_1$ at separation associated with shock wave C_2 , and a second compression $\triangle p_2$ at re-attachment due to shock wave C_5 [10]. Since the pressure rise at separation is independent of the incident shock wave strength, an increase in the overall pressure rise is associated with a higher pressure rise at re-attachment. This can be achieved only by an increase in the maximum velocity reached on the discriminating streamline. This would entail greater mixing between the shear layer and the outer inviscid flow which is enabled by an increase in the shear layer length. Thus the length of the shear layer grows with increase in the pressure rise at re-attachment.

Thus a simple inviscid shock pattern of incident and reflected shock waves is replaced by a multi-shock system when viscous flow i.e the boundary layer is considered. The following section discusses the unsteadiness of the reflected shock wave, which is a major cause of performance degradation due to SWTBLIs.

2.3.2 Unsteadiness of the Reflected shock-wave

Experimental investigations have shown that the reflected shock wave is highly unsteady and causes fluctuating pressure loads [15] [7]. In an engine intake, the fluctuating pressure loads can lead to structural damage of the compressor blades due to fatigue [11]. In worst case scenario, these effects can lead to an engine unstart leading to catastrophic consequences [38]. To eliminate or mitigate these detrimental effects of SWTBLIs, it is important to first understand the mechanisms that drive this unsteady behaviour.

According to Erengil and Dolling [15], the reflected shock wave unsteadiness is composed of two components; the large-scale low-frequency shock foot movement and the small-scale high-frequency shock foot movement [15]. They observed a clear correlation between the upstream boundary layer pressure and the shock foot motion. The correlations suggested that the pressure fluctuations preceded the shock foot motion [15]. Thus Erengil and Dolling [15] suggested that the small-scale high-frequency motion is driven by the large scale turbulent fluctuations in the incoming boundary layer [15]. Additionally, they also found correlations between the pressure in the separated flow regions and the intermittent region, indicating that the separation bubble pressure fluctuation influenced the shock foot motion. Thus, the large-scale low-frequency shock oscillation is due to the expansion and contraction of the separation bubble. However, the process driving the expansion and contraction of the separation bubble is not yet completely understood.

Further, Ünalmis and Dolling [44] performed correlations between the upstream pitot pressure measurements and shock foot location rather than the shock foot motion. They found that high pitot pressure in the upstream boundary layer was correlated with the shock foot being located downstream of its mean position [45]. Similarly, a low pitot pressure in the upstream boundary layer was associated with the shock foot being located upstream [44]. According to them [44], the shock foot is driven by a low frequency thickening and thinning of the upstream boundary layer. Later Ünalmis and Dolling [45] found a correlation between the scale of the separated flow and spanwise variations in pitot pressure in the incoming boundary layer [45]. The spanwise pitot pressure variations indicate the presence of spanwise vortices which might be the cause or one of the causes of the low frequency pulsation of the separated flow regions [45].

Beresh *et al* [7] tested this model proposed by Ünalmis and Dolling [45]. They found that the shock foot has a tendency to move downstream when the velocity fluctuations in the incoming boundary layer are positive and the boundary layer velocity profile is momentarily fuller [7]. A fuller boundary layer velocity profile offers greater resistance to retardation due to the shock, hence pushes the shock downstream [7]. Similarly, when the velocity fluctuations are negative, the shock foot has a tendency to move upstream. Such continuous velocity fluctuations in the incoming boundary layer cause an unsteady shock foot motion [7]. A schematic showing the relationship between the upstream boundary layer velocity profile and shock position from Beresh *et al* [7] is shown in figure (2.4).

Furthermore, Beresh *et al* [7] indicate that the relationship between the velocity fluctuations and the shock motion may not explain the fundamental relationship behind the unsteadiness.

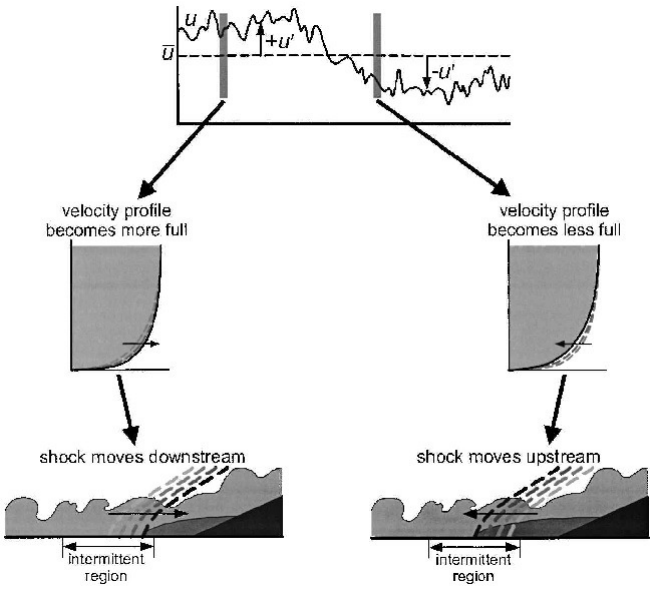

Figure 2.4: Relationship between upstream boundary layer velocity profile and shock position [7].

According to them, the rate of change of shape of the upstream velocity profile with respect to the mean profile may be the mechanism which drives the interaction unsteadiness [7]. Thus, shock movement upstream is due to an upstream velocity profile which has become fuller than it was earlier. This might be due to negative velocity fluctuations which have become less negative than the velocity fluctuations previously [7]. Another example explained by them is that of positive velocity fluctuations that remain constant for a relatively long period of time such that the velocity profile exhibits no change. In this case, the boundary layer resistance remains the same despite positive velocity fluctuations in the upstream boundary layer [7]. Like previous studies, Beresh *et al* [7] also found a mismatch in the frequency of shock motion and the upstream turbulent fluctuations. The characteristic turbulent frequencies in the upstream boundary layer from their investigations is about 40kHz while the shock foot motion frequency is about 0.1-4kHz [7].

It has been indicated by Ganapathisubramani *et al* [17] that the span wise modulation of the separation bubble size is related to low speed and high speed regions in the incoming boundary layer. The instantaneous separation point moves upstream in the presence of a low speed region in the incoming boundary layer and downstream in the presence of a high speed region [17]. Dussauge *et al* [13] have reported that the three dimensional structure of the separation bubble may be responsible for the low frequency unsteadiness of the reflected shock wave. It is suggested by them [13] that the vortical structures involved may have the same frequency scales as the leading frequencies of the shock motion. According to them, this underlines the importance of the conditions downstream of the shock which might cause the shock motions [13].

While the previous discussion deals with mainly compression ramp studies, Humble *et al* [23] performed tomographic-PIV investigations of an incident SWTBLI at Mach number $M_\infty = 2$

and visualized the three-dimensional instantaneous flow organization in the interaction region. Humble *et al* [23] found that when a relatively higher speed fluid enters the interaction region, it is able to negotiate with the adverse pressure gradient better and hence the reflected shock is displaced downstream of its mean position. For the case of the lower speed fluid entering the interaction region, the reflected shock wave is pushed upstream of its mean position [23]. The spatial organization of low speed and high speed strips in the incoming boundary layer leads to the streamwise translation and spanwise rippling patterns of the reflected shock wave [23]. While moving away from the wall, the spatial organization of the flow features in the incoming boundary layer becomes disorganized [23]. The shock wave pattern becomes more uniform in the spanwise direction undergoing smaller streamwise movement with increasing distance from the wall. A schematic of the three-dimensional physical model of incident SWTBLI proposed by Humble *et al* [23] is presented in figure (2.5).

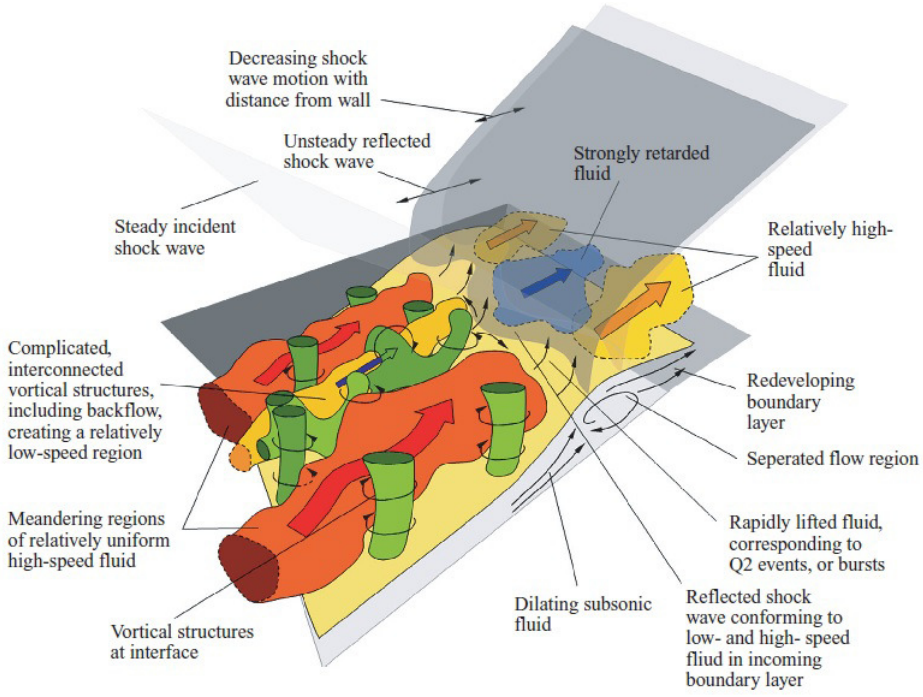

Figure 2.5: Three dimensional physical model of incident SWTBLI by Humble *et al* [23].

For the case of incident SWTBLI, Pirozzoli and Grasso [32] have indicated an acoustic feedback mechanism based on the internal dynamics of the separated flow regions. Additionally Dupont *et al* [12] suggested that the downstream part of the interaction i.e. the downstream recirculating zone is strongly linked to the reflected shock motion at a low frequency [12]. Therefore, several mechanisms are suspected to be associated with the large-scale low frequency unsteadiness of the interaction.

2.4 Micro-ramp vortex generators

Micro-ramp vortex generators are derivatives of conventional vortex generators, and feature a height smaller than the boundary layer. Typically their heights are 50% of the boundary layer thickness and are also called as sub-boundary layer vortex generators [33] or low profile vortex generators [5].

Micro-ramps and their usefulness in supersonic intakes were popularized by Anderson et al. [4] who performed an optimization study and determined an optimal geometry of micro-ramps. The geometry of micro-ramp vortex generators proposed by Anderson et al. [4] after their optimization study has been popular amongst researchers and is termed commonly as the standard micro-ramp or Anderson-type micro-ramp vortex generator.

2.4.1 Standard Micro-ramp geometry

Micro-ramps are characterized by their height (h), chord length (c) and their angle of incidence or semi-angle (A_p) and these parameters are shown in figure (2.6).

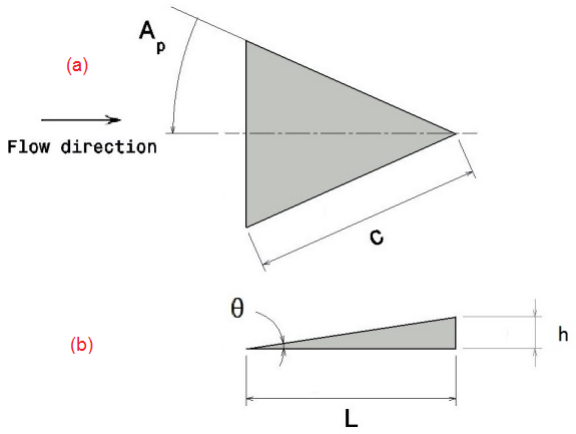

Figure 2.6: Micro-ramp geometry parameters (a) top view (b) side view

For a standard micro-ramp or Anderson type micro-ramp, the micro-ramp chord $c = 7.2h$, the semi-angle $A_p = 24°$ and the ramp angle $\theta = 8.6°$ where h is the height of the micro-ramp. The effectiveness of the micro-ramps is the ability of the micro-ramp to eliminate or reduce flow separation. With increase in height of the micro-ramp, its effectiveness also increases, i.e. larger micro-ramps are more effective than smaller micro-ramps [6], [19] .

2.4.2 Working principle and Flow features

The working principle of micro-ramps is essentially the same as for the conventional vortex generators. The surface oil flow visualizations by Ford and Babinsky [16] have revealed that two counter-rotating vortices form the principal flow features generated by a micro-ramp. The two counter-rotating vortices are commonly known as the 'primary vortex pair'. The surface oil flow visualization by Ford and Babinsky [16], showing the characteristic footprint of the primary-vortex pair has been shown in figure (2.7).

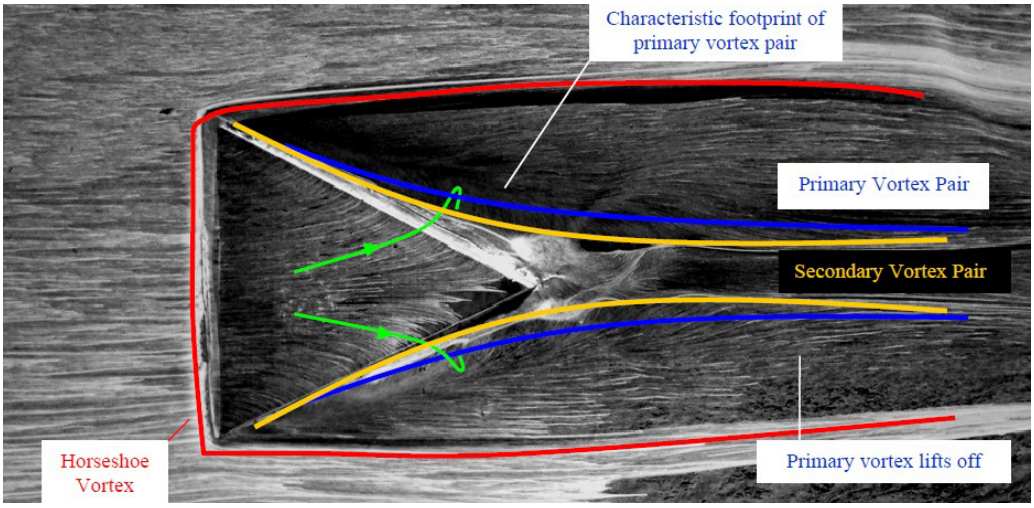

Figure 2.7: Surface oil flow pattern from Babinsky et al. [6] for h= 6mm micro-ramp in a $M_\infty = 2.5$ turbulent boundary layer showing the main flow features

The two counter-rotating vortices induce a mutual upwash on each other and hence they are lifted away from the wall as they move downstream . Due to this, their footprint fades while moving downstream. As they are lifted away from the wall, they transport higher momentum fluid from the outer parts of the boundary layer to the near wall regions. Due to this action of the counter-rotating vortices, the low momentum fluid from the near wall regions is transported to the outer parts of the boundary layer and/or outside the boundary layer. Due to the transport of higher momentum fluid to the near wall regions by the micro-ramp, a fuller boundary layer velocity profile is expected when a micro-ramp is used.

Figure (2.8) shows the spanwise velocity profiles for a h= 4 mm micro-ramp, 20 mm downstream of the micro-ramp trailing edge. In this figure the velocity profiles in the presence of the micro-ramp are fuller compared to the case without micro-ramps. While moving away from the micro-ramp symmetry plane (Z = 0), the velocity profile becomes 'less full'. The furthest outboard profile (Z = 12 mm) is very close to the clean tunnel profile. This suggests that the micro-ramp does not affect the flow beyond its span [6]. At the symmetry plane of the micro-ramp, a velocity deficit can be observed. This is representative of the low momentum region created due to the action of the counter-rotating vortices [6].

In addition to the primary vortex pair, other secondary vortices are also formed in the micro-ramp flow. One pair of secondary vortices is formed between the micro-ramp side wall and

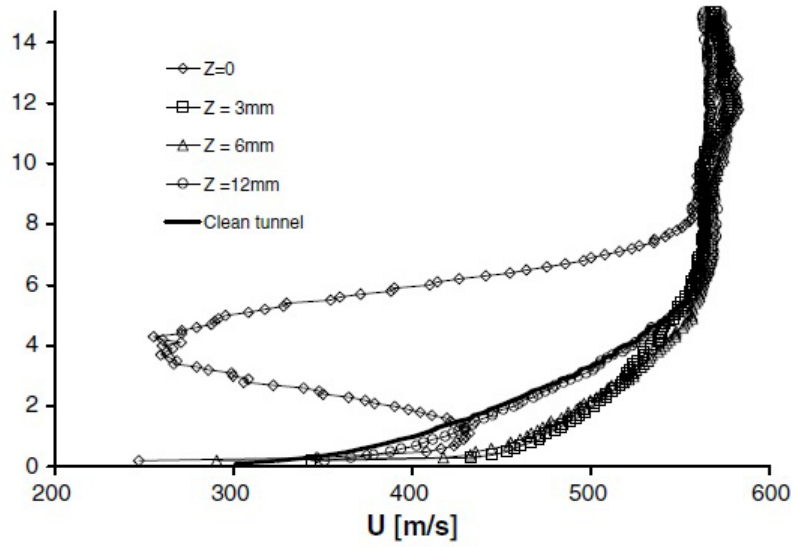

Figure 2.8: Boundary layer velocity profiles 20 mm downstream of the micro-ramp trailing edge at different span-wise locations [6]. z = 0 represents the centreline while z = 12 mm represents micro-ramp edge.

the floor junction as indicated in figure (2.7). Another pair of secondary vortices is formed at the top edges of the micro-ramp, but these vortices are not visible in this figure. Further according to Babinsky et al. [6], a small separated region is formed at the leading edge of the micro-ramp [6]. This separated flow forms a horseshoe vortex and is advected downstream [6]. The bright oil streaks on either side of the micro-ramp wake are attributed to the horseshoe vortex by Babinsky et al. [6].

In addition to the oil flow visualizations previously mentioned, Lu *et al* [28] also visualized the horseshoe vortex for a micro-ramp of $\theta = 8.6°$ and $M_\infty = 2.5$ in their ILES investigation. The horseshoe vortex has not been observed properly in many experimental and numerical studies. For example, the hybrid LES/RANS studies of Ghosh *et al* [18] at $M_\infty = 4$ does not show the presence of any horseshoe vortex. Similarly, tomographic-PIV studies of Sun *et al* [42] also does not show the presence of a horseshoe vortex(?). To conclude, it has mainly been recorded in oil flow studies.

It is important to note that the ramp angle of a standard micro-ramp is $\theta = 8.6°$. According to Kuehn [25], separated flow region is formed only if the flow deflection angle is above the incipient separation threshold, $\theta_{inc} \approx 15°$ [25]. Therefore, based on Kuehn's threshold [25], no separated region upstream of the micro-ramp leading edge is expected in both the cases of Babinsky *et al* [6] and Lu *et al* [28]

A schematic illustration of all the streamwise vortices in micro-ramp flow is shown in figure (2.9). Only one half of the symmetrical flow has been shown for clarity.

Further, according to Sun *et al* [42] the counter rotating vortex pair is symmetrical about the center plane of the micro-ramp. This can be seen in figure(2.10) at three streamwise locations

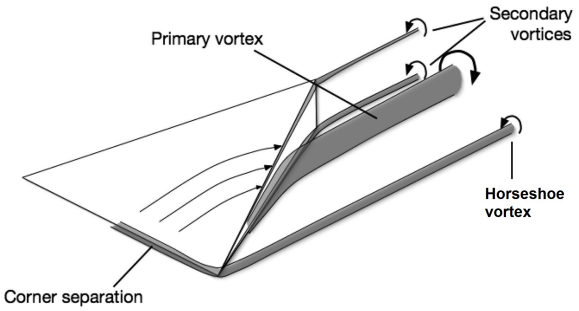

Figure 2.9: Main flow features shown only on one side of the micro-ramp for clarity[6]

downstream of the micro-ramp. While moving downstream, the counter rotating vortex pair is lifted off due to the mutual upwash induced on each other. Further, the streamwise vortices are contained in a circular wake and bounded by shear layer at the outer edge as shown in figure (2.10).

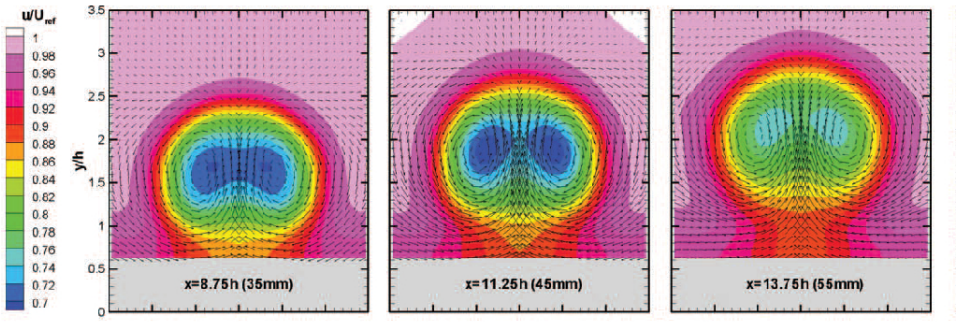

Figure 2.10: Two-dimensional cross sections showing u contours of the mean flow field at different stream wise locations [42].

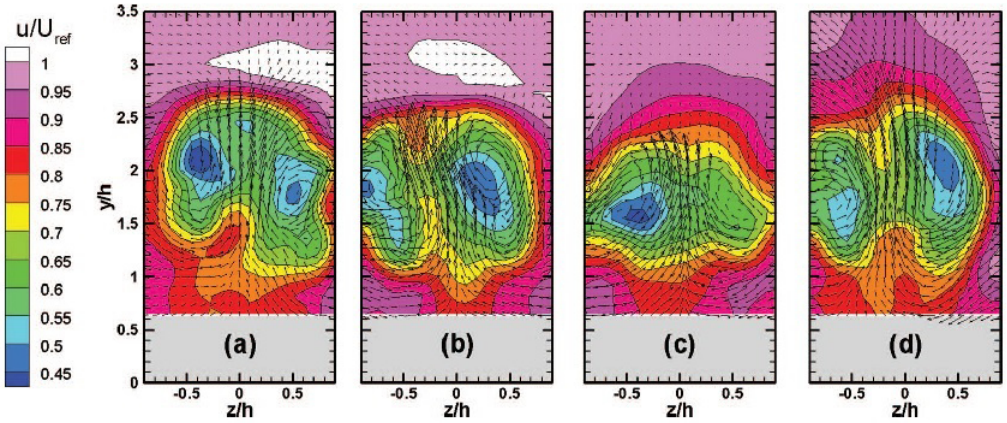

Figure 2.11: Two dimensional cross sections showing u contours of four instantaneous snapshots at a stream wise location of $x/h = 10.5$ [42].

The instantaneous flow results from Sun *et al* [42] showed that the stream wise vortex pair shows an undulating behaviour. Unlike the mean flow, significant variations in the span wise position of the counter-rotating vortices can be observed in figure (2.11). Further,the wake edge is not regular as in the mean flow results. The wake edge is irregular due to the imprint of the Kelvin-Helmholtz (K-H) type vortices which are seen at the interface between the wake region and the freestream [42]. These K-H vortices can be seen in figure (2.12) where the vectors are shown in a convective frame of reference.

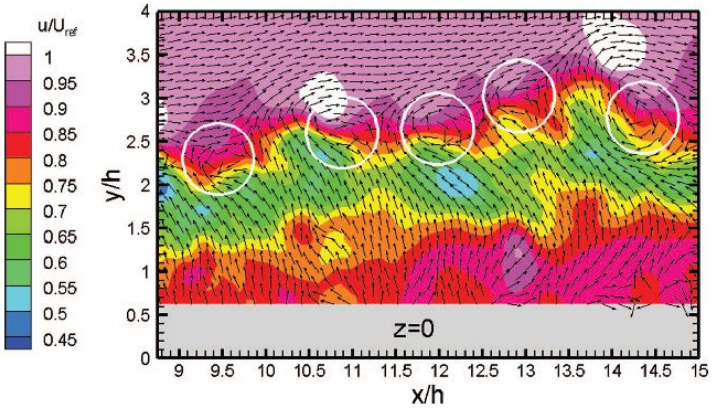

Figure 2.12: K-H vortices formed at the interface between the wake region and the free stream , velocity vectors shown in a convective frame of reference $U_{conv} = 0.83\ U_{\infty}$[42].

Under the head of a K-H vortex, the primary vortex cores appear to come closer to one another [42]. This can be seen in figure (2.13). While moving away from the micro-ramp centreline the K-H vortices curve towards the wall encompassing the top part of the counter rotating vortices [42]. Due to the generation of the K-H vortices the stream wise vortex filaments show upward and downward motion leading to connections with the legs of the K-H vortices [42]. In some cases, the legs of the K-H vortices also merge with the primary vortices. Downstream of the K-H vortex head, the primary vortices are highly stretched and titled, leading to interruption in the vortex filament.

Additionally, the numerical results of Li and Liu [26] also found K-H instabilities which become larger and irregular while moving downstream. Since they interact strongly with the shock wave, the K-H vortices appear to play an important role in micro-ramp flow control [26]. Further, according to the compression ramp study by Yan *et al* [48], the vortex rings are the main mechanism responsible for the effectiveness of the the micro-ramps. The vortex rings never break down even when they pass through the separation shock [48]. However, the separation shock itself is broken down due to the low pressure at the vortex cores and the adverse pressure gradient disappears due to this [48]. Thus the shock induced separation also disappears due to the vortex rings. In conclusion, though many investigations have confirmed the existence of these K-H vortices, it seems that their exact role in micro-ramp working mechanism is not fully understood.

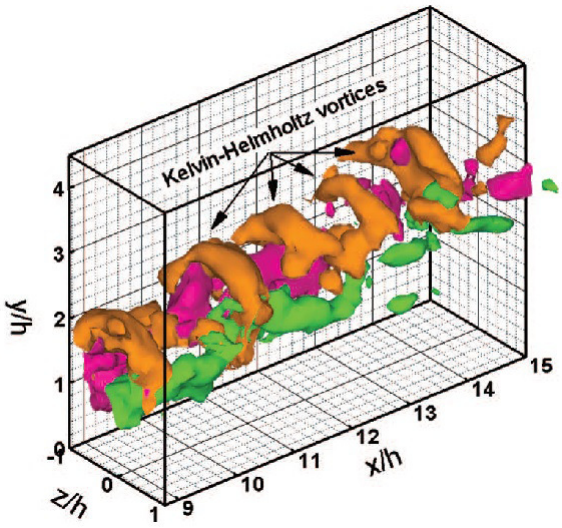

Figure 2.13: Iso-surface of vorticity showing the stream wise counter rotating vortex pair and the K-H vortices [42].

2.5 Micro-ramp control of SWBLI

For boundary layer control using micro-ramps, the micro-ramp is placed upstream of the inviscid shock impingement location such that the boundary layer entering the interaction region is more resistant to the adverse pressure gradient. Hence the location of the micro-ramp is an important parameter which governs the effectiveness of micro-ramps. Giepman *et al* [19] found that placing the micro-ramps too far away or too close to the interaction did not improve the performance of micro-ramps. They found that a micro-ramp must be placed atleast a minimum distance of $d = 5.7\delta$ upstream of the inviscid shock impingement location and for $d > 13.8\delta$ best performance is achieved [19].

The application of micro-ramps does not completely eliminate the separation bubble but breaks the separation bubble into individual smaller cells [16, 19]. When the mean flow field is considered, it appears that the micro-ramp completely eliminates the separation bubble along its centreline. However, its effectiveness is reduced when moving away from the centreline of the micro-ramp. This can be seen in the mean velocity distribution at different spanwise locations for a $h = 4$mm micro-ramp is shown in figure (2.14).

It is seen that at 50% span of the micro-ramp or $z = 2.3\delta$, the mean velocity distribution shows a large separation bubble unlike at the centreline of the micro-ramp. This clearly shows that the micro-ramp creates a spanwise modulation of the separation bubble. However, though micro-ramp eliminates the separation bubble at the centreline on average, instantaneously separated regions still exist along the centreline as seen [19]. This is due to the instantaneous meandering behaviour of the counter-rotating vortices.

Further, Giepman et al. [19] used the separation probability of the boundary layer as a metric

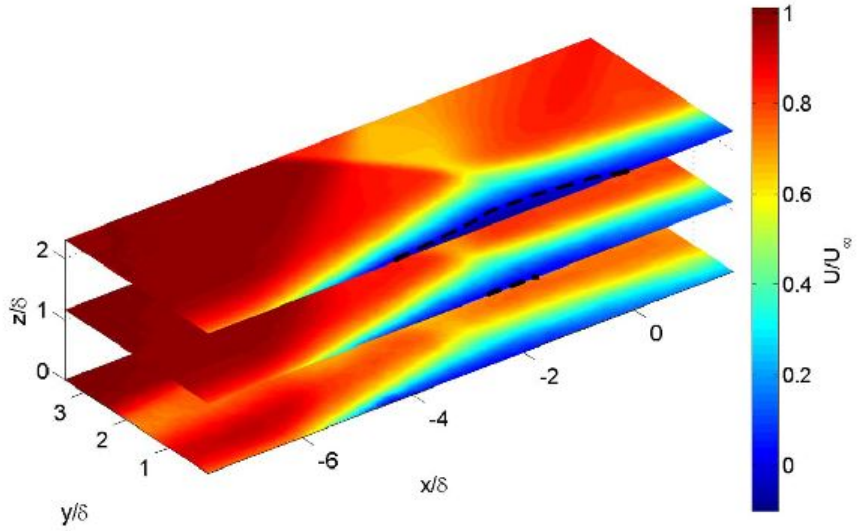

Figure 2.14: Mean streamwise velocity distribution at spanwise locations $z/\delta = 1.15$ and 2.3, for $h = 4$ mm micro-ramp placed $d = 17.8\delta$ upstream, from Giepman *et al* [19].

to compare the uncontrolled interaction with the micro-ramp controlled interaction. Since separated regions could not be accurately determined by them; a less sensitive criterion of flow reversal was considered by them. Therefore, separation probability P_{sep} is defined as the probability that a certain point in the measurement region shows reversed flow [19]. In the uncontrolled interaction, some regions close to the wall exhibit flow reversal 75% of the time and by using a micro-ramp this is reduced to 41% as seen in figure (2.15).

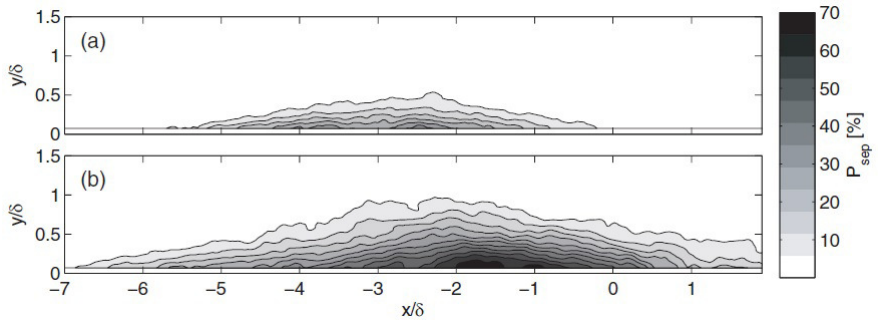

Figure 2.15: Separation probability (a) P_{sep} with a $h = 4$mm micro-ramp (b) P_{sep} for the uncontrolled interaction.

Since, the effect of a micro-ramp does not extend beyond its span, for practical applications micro-ramp arrays would be necessary. To this end, Blinde *et al* [8] investigated micro-ramp arrays in two configurations; single-row array and double-row staggered array. In contrast to the mean flow results of Giepman *et al* [19], Blinde *et al* [8] found that the effect of the micro-ramps is least downstream of their apices or centrelines, and increases while moving away from their centreline (in the figure micro-ramp locations are indicated by black triangles). From

their results, it appears that the micro-ramps increased the extent of low velocity regions along their centrelines as shown in figure (2.16).

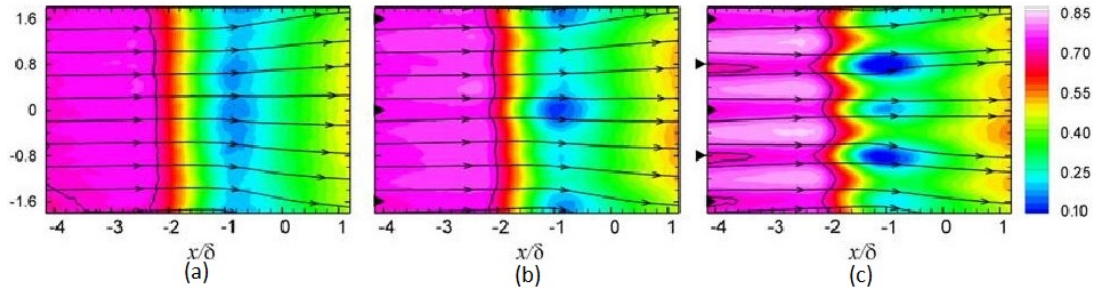

Figure 2.16: Mean velocity fields U/U_∞ at y/δ = 0.1 from Blinde *et al* [8]. (a) Uncontrolled interaction (b) Single-row array control (b) Double-row staggered array control. (Black triangles indicate locations of micro-ramps)

From the results of Blinde *et al* [8] at y/δ = 0.6, it appears that downstream of the micro-ramps' apices, the amount of low momentum fluid has increased compared to the uncontrolled interaction in both array configurations. This can be seen in figure (2.17) where U$\approx$ 0.5U$_\infty$ fluid is found in both the array configurations and is completely absent in the uncontrolled interaction. This indicates that in the controlled interaction, the separated flow regions might have a greater wall normal extent compared to the uncontrolled interaction. Therefore, it is of prime importance to investigate whether application of micro-ramps actually reduces the total amount of separated flow.

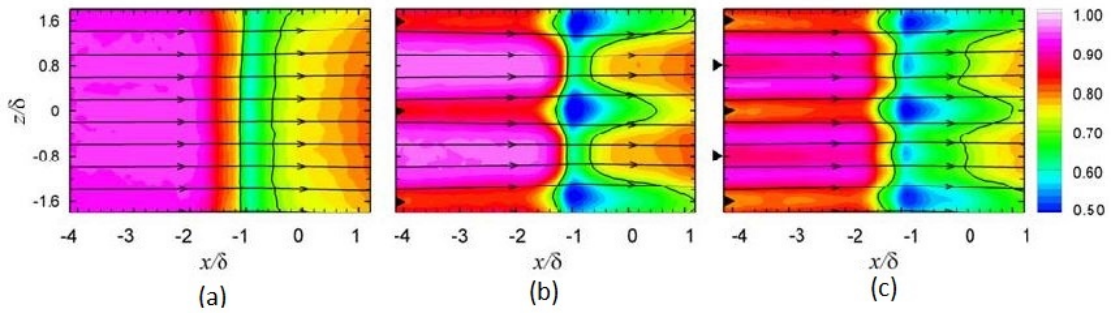

Figure 2.17: Mean velocity fields U/U_∞ at y/δ = 0.6 from Blinde *et al* [8]. (a) Uncontrolled interaction (b) Single-row array control (b) Double-row staggered array control

As discussed in the previous section, the size of the separation bubble is correlated to the locations of the reflected shock wave [13]. Hence micro-ramps also reduce the unsteadiness of the reflected shock wave [8] by reducing the size of the separation bubble. Giepman *et al* [19] used the maximum of dV/dx as a shock detection criterion and determined that with the micro-ramp, the reflected shock unsteadiness is approximately halved for a h = 4 mm micro-ramp placed 17.3δ upstream of the interaction. Interestingly, the micro-ramp reduces the reflected shock unsteadiness at 50

In case of micro-ramp arrays, Blinde *et al* [8] found that the largest reductions in the unsteady motion of the reflected shock wave occurred downstream of the apices of the micro-ramp. This can be seen in figure (2.18), where downstream of the micro-ramp apices, the size of the intermittent region is smaller. However, with micro-ramp control the extent of the motion has increased in both the array configurations when compared to the uncontrolled interaction.

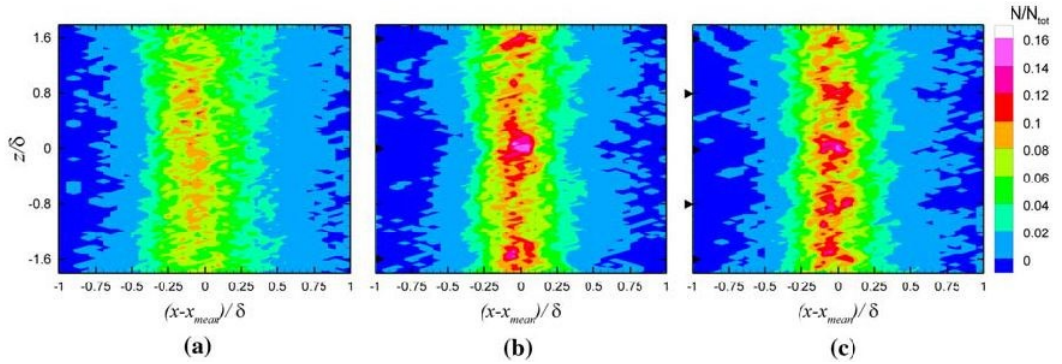

Figure 2.18: Discrete PDFs of reflected shock wave position at $y/\delta = 0.1$ [8] (a) Uncontrolled interaction (b) Single-row array control (b) Double-row staggered array control

2.6 Summary

The flow organization downstream of a micro-ramp proposed by Babinsky et al. [6] recognized a counter rotating vortex pair as the primary flow feature in the micro-ramp wake. This was confirmed by the tomographic-PIV experiments of Sun et al. [42]. From the studies of Hirt and Anderson [21], Babinsky et al. [6] and Giepman et al. [19] it is noted that larger micro-ramp produces larger and stronger vortices, due to which larger micro-ramps are more effective compared to smaller micro-ramps. The surface oil flow measurements by Ford and Ford and Babinsky [16] and planar PIV studies by Giepman et al. [19] both confirm that the micro-ramp breaks the separation bubble into smaller cells and that the effect of the micro-ramps does not extend far beyond their span. Spanwise modulation of separation bubble size was noted by Giepman et al. [19], but due to the three dimensionality of the bubble its exact effect on the unsteadiness needs to be investigated.

The planar PIV investigation by Giepman *et al* [19] found that the separation probability decreases downstream along the micro-ramp centre line and increases while moving away from the centre line. The stereoscopic PIV results of Blinde et al. [8] also reported that the separation probability was reduced by using a single row of micro-ramps as well as a double row staggered micro ramp array. At a wall normal location of y/δ=0.6 studied by Blinde et al. [8], it is found that the regions where separated flow exists in the controlled interaction case, these separated regions show a greater wall normal extent compared to the uncontrolled interaction [8]. Therefore, it still remains unclear whether the volume of separation has been reduced by employing micro-ramps [43].

Chapter 3

Experimental Techniques and Arrangement

Firstly, this chapter provides the description of the wind tunnel and the micro-ramp geometry used for the experiments, in section (3.1) and section (3.2) respectively.

Further, the working principles of the experimental techniques: Schlieren visualization, surface oil flow visualization and Tomographic-PIV used in this thesis are discussed in section (**??**). This section also includes the experimental set up and the test matrices for these experimental techniques.

3.1 Flow Facility

All the experiments were performed in the supersonic wind tunnel ST-15 at the High Speed Laboratory of the faculty of Aerospace Engineering at TU Delft. The Mach number was $M_\infty = 2$ with a total pressure of 3.2×10^5 N/m^2 and a total temperature of 278 K. The unit Reynold's number was 43.5×10^6 m^{-1}. A schematic representation of the ST-15 is shown in figure (3.1).

The wind tunnel is comprised of four parts, namely; the settling chamber, the nozzle, the test section and the diffuser. The air that is used to drive the tunnel is dried and stored in a $300m^3$ reservoir at 40 bars. The settling chamber is connected to the reservoir and it consists of meshes or screens to reduce the turbulence level in the flow. The settling chamber provides access ports to introduce PIV seeding particles into the flow. The test section measures 150×150 mm^2 and has glass windows to allow optical access for Schlieren and PIV measurements. For SWBLI experiments, an incident shock wave of shock angle $\beta = 42°$ is created by a nearly full span (120 mm) 12° shock generator. The inviscid shock impingement location is taken as the origin of the co-ordinate system, with x measured in the downstream direction from this origin, y normal to the wall and z in the spanwise direction.

The shock generator and the micro-ramps, along with a representation of the incident and reflected shock waves for the inviscid case are shown in figure (3.2).

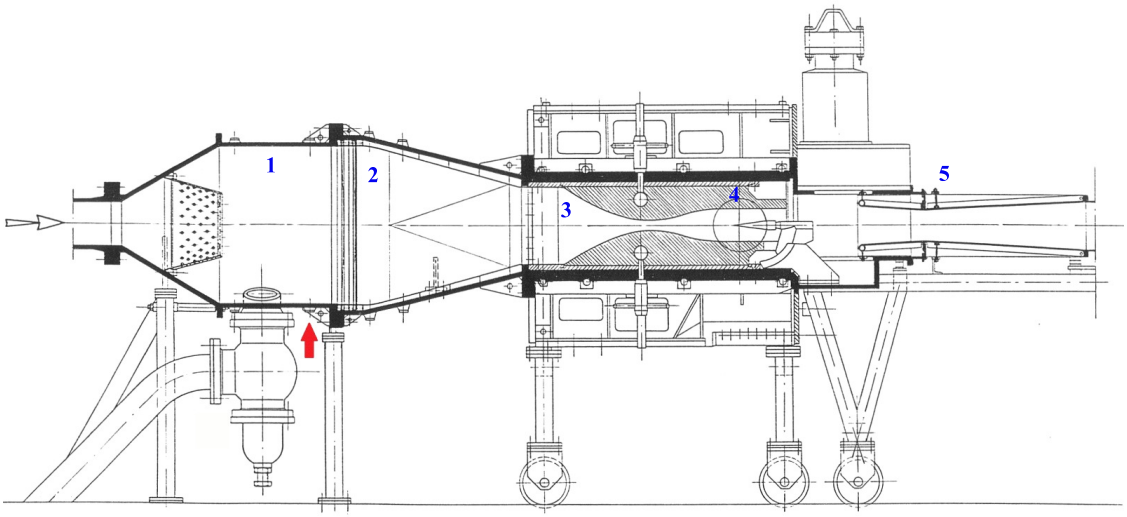

Figure 3.1: Cross section of the ST-15 wind tunnel. (1) Settling chamber (2) Screens (3) Nozzle (4) Test section (5) Diffuser. The red arrow indicates the location of the access port through which seeding is introduced into the wind tunnel for the tomo-PIV experiments.

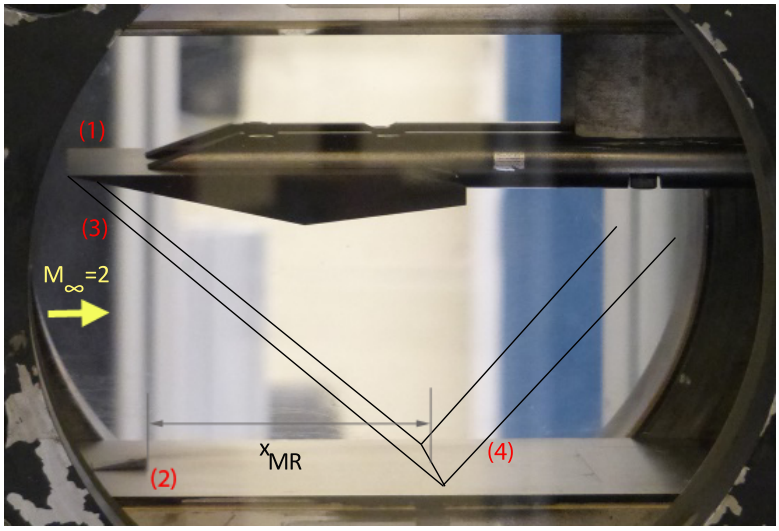

Figure 3.2: Test section of ST-15 with a representation of the oblique shock reflection for the inviscid case. (1) Shock generator (2) micro-ramp (3) incident shock wave (4) reflected shock wave. Flow direction is from left to right. x_{MR} is the distance between the micro-ramp trailing edge and inviscid shock impingement location.

3.2 Micro-ramp geometry

Micro-ramps of height h= 3 mm and geometry prescribed by Anderson et al. [4] ; with a micro-ramp half angle $A_p = 24°$, ramp angle $\theta = 8.6°$, a chord length c= 7.5h (4.32δ) and length L= 6.6h (3.8δ) were used for all experiments on SWBLI control by micro-ramps. A schematic representation of the micro-ramp geometry used for the SWBLI study is shown in figure (3.3).

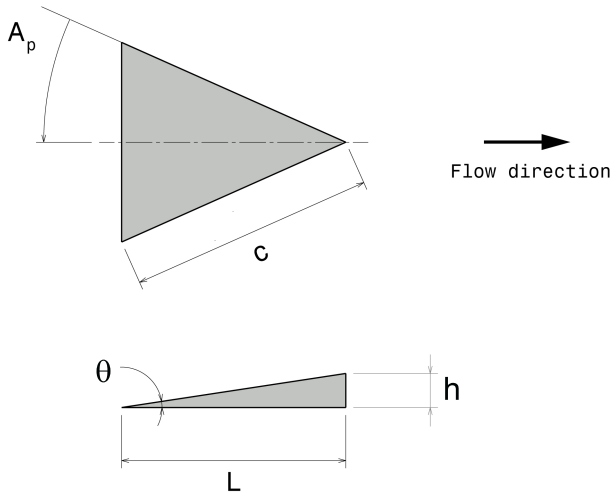

Figure 3.3: Micro-ramp geometry parameters.

Micro-ramps were placed $x_{MR} = 17.3\delta$ upstream of the incident shock wave according to the recommendations of Giepman et al. [19]. For the case of the single micro-ramp, the micro-ramp symmetry axis was aligned with the centreline of the wind tunnel. For the case of micro-ramp arrays, the distance between each micro-ramp $s = 1.6$ h (1.6δ) was chosen as per the recommendations of Anderson et al. [4]. A schematic of the single-row and double-row staggered array of micro-ramp arrays used in this study are shown in figure (3.4a-b).

For the surface oil flow experiments to investigate the horseshoe vortices generated by a micro-ramp, Anderson type of micro-ramps ($A_p = 24°$) with ramp angle $\theta = 4.3°, 13°, 17.3°, 21.6°$ were used in addition to the 8.6° micro-ramp. The dimensions of all the micro-ramps used in the oil flow study pertaining to horseshoe vortices are listed in table (3.1).

Ramp angle θ	Length L	Chord c
4.3°	13.2h (7.6δ)	14.5h (8.4δ)
8.6°	6.6h (3.8δ)	7.2h (4.1δ)
13°	4.3h (2.5δ)	4.8h (2.8δ)
17.3°	3.2h (1.85δ)	3.5h (2δ)
21.6°	2.5h (1.6δ)	2.8h (1.6δ)

Table 3.1: Geometry parameters of micro-ramps used for the oil flow study of horseshoe vortices

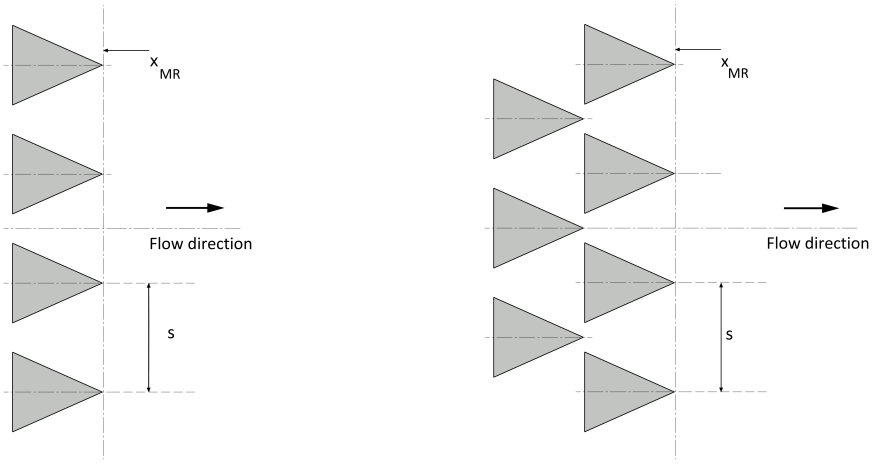

(a) Single-row micro-ramp array. (b) Double-row staggered micro-ramp array.

Figure 3.4: Micro-ramp array geometrical parameters.

3.3 Experimental set-up and test matrices

The working principles, experimental set ups for Schlieren, Surface oil flow visualization and Tomographic-PIV are discussed in this section. The test cases investigated using each technique are presented in the form of test matrices.

3.3.1 Schlieren Visualization

Schlieren visualization is an optical, non-intrusive flow visualization technique. It is based on refraction of light due to changes in the refractive index caused by density gradients in the flow. The deflected rays are obstructed by a knife-edge with acts as a cut-off filter before the light rays reach the camera.

The refractive index of a medium is related to its density through the following relation:

$$n = \frac{c_0}{c} = 1 + K\rho \tag{3.1}$$

where n is the refractive index (n = 1.0003 in air), ρ is the density of the medium, c_0 is the speed of light in vacuum(3×10^8m/s), c is the local light speed and K is the Gladstone Dale constant in that medium ($2 \times 10^{-4} m^3$/kg for air).

The luminance level in a Schlieren image responds to the first spatial derivative of refractive index (∇n) and therefore the corresponding flow quantity measured is the gradient of density ($\nabla \rho$). When light waves pass through regions of varying densities, they are deflected through different angles due to which their positions in the image plane are shifted. Upward deflected rays brighten a point and downward deflected rays darken a point since they are cut off by the knife-edge. The component of density gradient visualized depends on the orientation of the knife edge.The density gradient in the direction normal to the knife edge is visualized.

The experimental set up is shown in figure (3.5). It consists of an incoherent light source, a condenser lens C, a pin hole P, a small concave mirror S, two large parabolic mirrors P1 and P2 on either sides of the test section, a knife edge K and a camera for imaging. The light

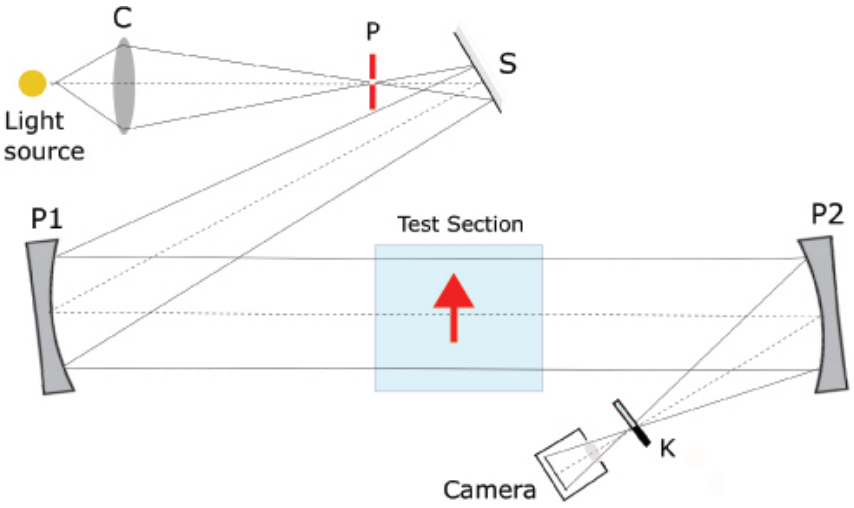

Figure 3.5: Schematic of the experimental set up used for Schlieren visualization, based on Settles [39]. Red arrow indicates the flow direction

from the light source is focussed on to the pin hole P by the condenser lens C. By using a clear Scotch tape on the pin hole, diffused light was obtained. The sensitivity of the Schlieren system to density changes depends on the diameter of the pinhole. By reducing the size of the pinhole, smaller density changes can be recorded. The light from the pin hole is then reflected by a small concave mirror S onto the large parabolic mirror P1.

The diameter of the light beam entering the test section or measurement region was approximately the same size as that of the test section windows. This was set by changing the location of the small mirror S. While moving through the test section, the light is deflected due to density changes across the incident and reflected shock waves.This deflected light beam

is reflected by the large parabolic mirror P2 after which it is intercepted by the knife edge K. For this study, the knife edge was positioned horizontally and the lower half of the light was blocked. The test matrix for the schlieren visualization experiments is shown in figure (3.2).

Expt No	Test cases	Micro-ramp height h in mm	Micro-ramp location
1	SWBLI	-	-
2	SWBLI controlled by single micro-ramp	3	17.3δ

Table 3.2: Test Matrix for Schlieren visualization, $M_\infty = 2$.

3.3.2 Surface oil flow visualization

Surface oil flow visualization serves to determine the direction of the velocity in close proximity of a model surface. Additionally, it can be used to identify low shear and high shear regions in the surface flow, transition location, separation and re-attachment.

A thin layer of highly viscous fluid like oil moves due to the action of friction exerted by air flowing over it. At the oil-air interface, the no-slip condition imposes that the air velocity equals the oil velocity. Further at the oil-air interface, the viscous stresses in the oil and the air are equal. At the wall, the oil is stationary due to the no-slip condition. Due to the large value of dynamic viscosity of oil, the gradient of velocity in the thin oil layer is smaller than that in air. The momentum equation reduces to a balance between the viscous forces and the pressure gradient. When the pressure gradient is small compared to the wall shear stress, the oil moves due to the viscous forces. However, in cases where there is boundary layer separation the wall shear stress becomes zero locally and the oil motion is influenced by the pressure gradient.

Therefore, separation lines are usually visualized as bright regions of oil accumulating from opposite directions. Reattachment lines appear as dark regions since oil is swept away from these regions due to high surface shear stress. Though the oil flow pattern provides a good representation of the flow topology close to the wall and quantitative information such as the location of separation and reattachment lines can be obtained, the flow organization away from the wall cannot be visualized.

In the present study, a mixture of bright TiO_2 particles and Shell Tellus type-22 oil was used for visualization. The bottom wall of the test section was covered by a thin black foil, and the micro-ramps were painted black to obtain a sufficient image contrast. It is important to ensure that the oil has suitable viscosity so that it does not flow too easily, or it is not too viscous that it does not follow the flow. Therefore, a few drops of oleic acid were added to obtain an oil film layer of suitable viscosity.

	Expt No	Test Cases	Location of micro-ramp(s) x_{MR}	Micro-ramp height h in mm
Set1	1	Uncontrolled SWBLI	-	-
	2	SWBLI controlled by single micro-ramp	17.3δ	3
	3	SWBLI controlled by single-row array of micro-ramps	17.3δ	3
	4	SWBLI controlled by double-row array of micro-ramps	17.3δ	3

Table 3.3: Oil flow Test Matrix for Experiment Set-1: Uncontrolled and controlled SWBLI, $M_\infty = 2$

Surface oil flow visualization experiments were performed for the cases of the uncontrolled SWBLI and the micro-ramp controlled SWBLIs, and they are grouped under Experiment Set-1. Micro-ramp controlled visualizations include single micro-ramp, single-row micro-ramp array and double-row staggered micro-ramp array configurations.

For the horseshoe vortex study, oil flow experiments were conducted for micro-ramps of different ramp angles. For these micro-ramps, the micro-ramp semi angle and height were constant at $A_p = 24°$ and h= 3 mm respectively. These experiments are grouped under Experiment Set-2. For the same horseshoe vortex study, surface oil flow visualizations were performed using micro-ramps of different heights h= 3 mm and 6 mm ($\theta = 8.6°$) and they are grouped under Experiment Set-3. The test matrices for Experiment Set-1, 2 and 3 are shown in table (3.3), table (3.4) and table (3.5) respectively.

	Expt No	Ramp angle of micro-ramp θ	Oil application
Set 2	1	4.3°	Everywhere(upstream and downstream of the micro-ramp)
	2	8.6°	
	3	13°	
	4	17.3°	
	5	21.6°	
	6	4.3°	Downstream of the micro-ramp's leading edge
	7	8.6°	
	8	13°	
	9	17.3°	
	10	21.6°	

Table 3.4: Oil flow Test Matrix for Experiment Set-3: Micro-ramps of different ramp angles in a Turbulent Boundary layer of $M_\infty = 2$

	Expt No	Micro-ramp height h in mm	Oil application
Set 3	1	3	Everywhere (upstream and downstream of the micro-ramp)
	2	6	
	3	3	Downstream of micro-ramp's leading edge
	4	6	

Table 3.5: Oil flow Test matrix for Experiments Set-2: Micro-ramps of different heights in a Turbulent Boundary layer of $M_\infty = 2$

3.3.3 Tomographic-PIV

Tomographic-PIV is a three-dimensional flow investigation technique which combines the principles of PIV and optical tomography, and was introduced by Elsinga et al. [14]. It is the extension of planar-PIV to three dimensions.

Seeding particles or tracer particles which follow the flow are first introduced into the region of interest. These particles are illuminated by laser light source and the scattered light pattern is recorded by a camera at two instants of time. Using the distance moved by the particles in the time interval between the two recordings, and the time interval, the velocity of the seeding particles be determined. From such measurements, 2D velocity organization in the region of interest can be determined. This forms the principle of planar-particle image velocimetry.

This method can be extended to 3D by imaging the region of interest from different unique directions or angles. These images are then reconstructed using the methods from optical tomography to obtain a three-dimensional image of the region of interest. The velocity can be calculated by applying the principle of PIV to two such reconstructed volumes and 3D flow fields can be obtained. Figure (3.6) pictorially represents the working principle of tomographic-PIV and the exact working principle is detailed below.

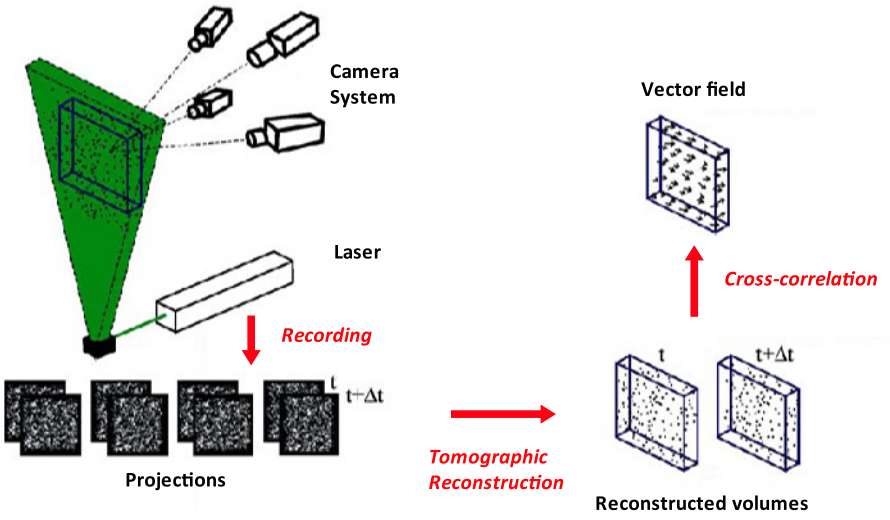

Figure 3.6: Principle of Tomographic-PIV, based on Elsinga et al. [14]

Volume Illumination

Seeding particles are introduced into the flow and are illuminated by a pulsed light source such as a laser. By using an arrangement of cylindrical and spherical lenses, the light sheet from the laser is expanded to provide volume illumination. However, the laser light intensity is inversely proportional to the thickness of the laser light sheet [35]. The reduction in energy density after distributing the laser light in the measurement volume becomes a limiting factor for the measurement volume sizes in tomographic-PIV [35].

Volume Imaging

The seeding particles scatter the laser light and the scattered light is recorded simultaneously from different viewing angles by CCD cameras. All the particles in the volume must be in imaged in focus to obtain high quality reconstructions of the volume. For this, the object plane or the camera focal plane is set to the centre of the measurement volume which forms an image on the image plane of the camera lens. In tomographic PIV the cameras are set at different angles due to which the camera focal plane does not align with the centre plane of the measurement volume. To eliminate this issue, the lens is rotated about its optical axis so that the focal plane coincides with the centre plane of the measurement volume and this is known as the Scheimpflug condition. The rotation of the lens is achieved by using lens-tilt

adapters or Scheimpflug adapters. By carefully setting the f-stop (f#), the depth-of-field is changed which ensures that all the particles are imaged in focus.

Calibration

The calibration procedure consists of a first physical calibration, followed by volume self-calibration.

(a) Physical Calibration: The volume reconstruction using the projections from different cameras Is based on the triangulation relation between the image co-ordinates and the physical world co-ordinates and this established by a physical calibration procedure. This procedure utilizes a calibration target which is a two level plate of known distance between the levels. A two level calibration target is shown in figure (3.7). Each level consists of dotted markers of known positions. Using a third order polynomial fit, a mapping function from the image co-ordinate system to the physical world co-ordinate system is obtained.

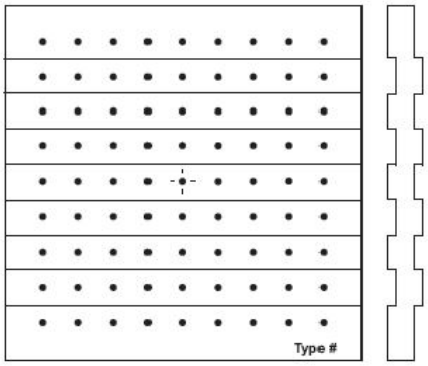

Figure 3.7: A dual plane calibration target [1]

(b) Volume Self-Calibration: Vibration of equipments, loose camera mounts can cause significant deviations from the established mapping function [47]. Aero-optical aberrations due to density gradients in the vicinity of shocks can also cause significant errors. Therefore, a particle image based volume-self calibration technique proposed by Wieneke [47] is used to mitigate such errors. By the process of volume self-calibration the disparity vector between the projected particle position (x',y') and the imaged particle position (x,y) is minimized. The disparity is represented in a disparity map at different depths for each camera. The mapping function for every camera is then corrected by using the disparity vector field.

Tomographic-Reconstruction

The 3D particle distribution in the measurement volume is reconstructed as a 3D light intensity distribution from the projections from the different cameras. This volume reconstruction is achieved by algebraic techniques such as ART (Algebraic reconstruction technique), MART (Multiplicative algebraic reconstruction technique) [14]. The particle displacement and hence the velocity is then calculated by 3D cross-correlation of two different reconstructed volumes.

Experimental set-up

The schematic of the experimental set up consisting of the cameras and the measurement volume is shown in figure (3.8). The different components of the tomographic-PIV experimental set-up are discussed in detail below.

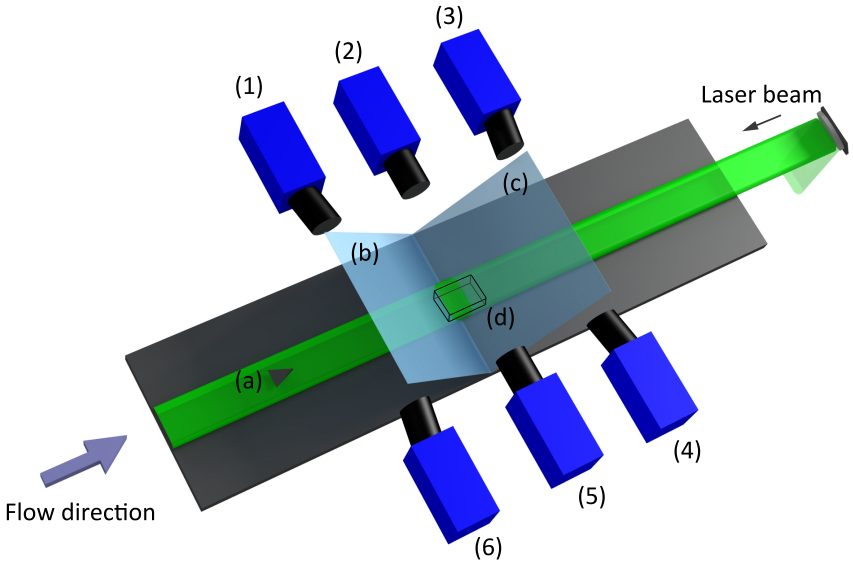

Figure 3.8: Schematic of the tomo-PIV set up. The cameras used for the experiments are labelled from (1) to (6). The micro-ramp is labelled (a), the incident shock wave (b), reflected shock wave (c). (d) indicates the position of the measurement volume.

- Cameras

  The Tomo-PIV set up consists of six 2 Megapixel LaVision Imager intense CCD cameras, and three cameras each were placed on either side of the test section as shown in figure (3.8). Cameras 1 and 6 were in back scatter mode while cameras 3 and 4 were in forward scatter mode. The cameras were equipped with objective lens of focal length 75 mm. The objectives were equipped with Scheimpflug adapters to place the focal plane in the mid-section of the measurement volume and to maintain the entire measurement volume in focus. The cameras had a sensor of size of 1624×1236 pixels with a pixel size of 4.4μ m.

- Illumination

  For illumination of the seeding particles, a Spectral Physics Quanta-Ray double pulsed Nd:YAG laser, shown in figure (3.9) was used. The wavelength of the laser beam is $\lambda = 532$ nm with an energy of 400 mJ per pulse and pulse duration of 6 ns.

  A set up consisting of a combination of cylindrical and spherical lenses was used to form a laser volume of finite thickness. To reduce the light reflections due to the test section windows, the laser beam was introduced into the test section from the back of the tunnel. This was achieved by using a combination of mirrors, to direct the laser beam to the flange at the bottom wall of the diffuser. A laser probe shown in figure (3.10) was attached to the

bottom wall of the diffuser and was used to introduce the laser beam into the test section. To achieve a light beam with sharp edges, a knife-edge filter was used at the flange.

Figure 3.9: Spectral Physics Quanta-Ray, Nd: YAG laser used for the tomographic-PIV experiments.

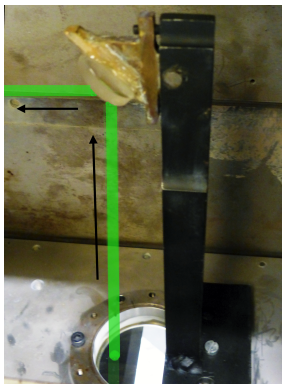

Figure 3.10: Laser probe (a) Flange at the bottom of the diffuser (b) Mirror

- Seeding

  The seeding for the tomo-PIV experiments was generated using the PIVTEC Aerosol generator PivPart45, which shown in figure (3.11). The seeding considerations for tomographic-

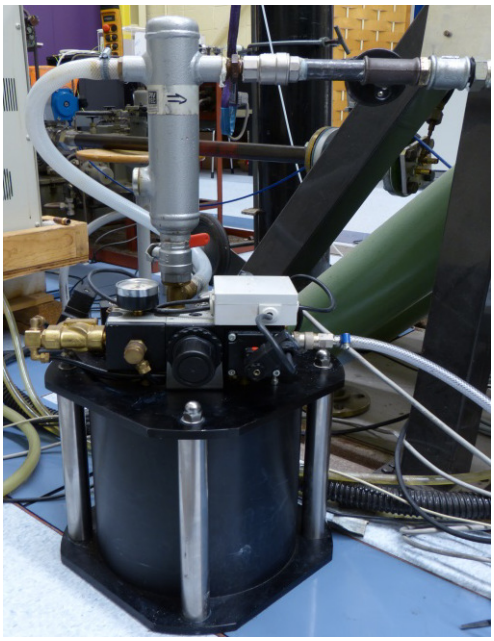

Figure 3.11: PIVTEC Aerosol generator used to produce the DEHS tracer particles.

Figure 3.12: Seeding rake

PIV experiments have been discussed in detail in appendix (A). Based on these considerations, Di-Ethyl-Hexyl-Sebacat (DEHS) particles were selected to be suitable tracers and were distributed into the settling chamber using a seeding distribution rake. The seeding

rake was designed by the author and was manufactured in the High speed laboratory and is shown in figure (3.12).

- Programmable Timing unit (PTU)

  The synchronization of camera trigger signals and laser, and image acquisition were achieved by a LaVision programmable timing unit (PTU) and the DaVis 8.2 software package. The tomo-PIV experiments were conducted in a double-pulse, double-frame mode. The laser pulse separation time was determined to be 0.8μs.

- Measurement volume/ Field of view (FOV)

  The measurement volume is located so as to image the separation bubble in the interaction region. The centre of the measurement volume was located $17.8\delta = 90$mm downstream of the trailing edge of the micro-ramp. The flow was imaged in the streamwise, spanwise and wall normal planes over a volume of 60 $\times$40 $\times$ 14.5 mm^3.

- Magnification factor (M)

  The magnification factor is defined as the ratio of image distance d_i to object distance d_o. It is a scaling factor and can be written as equation (3.2).

$$M = \frac{d_i}{d_o} = \frac{\text{pixel size} \times \text{no of pixels}_{streamwise}}{\text{FOV}_{streamwise}} \tag{3.2}$$

  With a pixel size $= 4.4 \times 10^{-6} m$ and 1624 pixels in streamwise x-direction, $M = 0.119$ is obtained. The resolution of the experiment can be obtained as equation (3.3).

$$Resolution = \frac{\text{no of pixels}_{streamwise}}{\text{FOV}_{streamwise}} \tag{3.3}$$

  For the experiments in the current study, the resolution was 36.1pixels/mm.

- f-stop ($f_\#$)

  $f_\#$ is defined as the ratio of the objective's focal length to the diameter of the lens aperture. According to Scarano [35], it is important that the particles are imaged in focus and that the focal depth δ_z is larger than or equal to the depth of the illuminated volume [35]. This requirement can be written as equation (3.4):

$$\delta_z \geq 4.88 \cdot \lambda \cdot f_\#^2 \Big(1 + \frac{1}{M^2}\Big) \tag{3.4}$$

  where λ is the wavelength of the laser beam and M is the magnification factor. With the focal depth equal to the depth of the illuminated volume $\delta_z = 14.5$mm, $f_\# = 8.08$ is obtained.

  According to Scarano Scarano [35], the particles outside the focal depth are imaged on a larger area called the blur circle. It is assumed that the out of focus effects will be negligible when the blur circle area d_b is limited to within 2pixels. Taking this requirement along with equation (3.4) above, Scarano [35] has suggested equation (3.5) as a rule to obtain the optimal f-stop.

$$f_\# \geq min\Big\{ \frac{M}{M+1} \sqrt{\frac{\triangle Z}{4.88\lambda}}, \frac{\triangle Z \cdot M^2}{4\, d_b} \Big\} \tag{3.5}$$

where $\triangle Z$ is the depth of the volume and d_b is the diameter of the blur circle. Since $f_{\#} = 8$ resulted in a large number of out of focus particles, $f_{\#} = 11$ was set on all the six cameras.

- Image Pre-processing

  Image pre-processing forms an important and necessary step in tomo-PIV due to the sensitivity of the reconstruction to the background light intensity [14]. Image pre-processing was performed using the filters available in the DaVis 8.1.6 software.

  The image pre-processing steps carried out to eliminate the background noise from the acquired images and to improve the particles images are detailed in Appendix B.

  All the tomographic-PIV recording parameters are summarized in table (3.6). The test matrix for tomographic-PIV is shown in table (3.7). Though experiments were performed with micro-ramp array configurations (Expt 4 and Expt 5), data from only Expt 1 - Expt 3 are analysed in this thesis due to time considerations.

Sl no	Parameter	Value
1	Measurement Volume	$60 \times 40 \times 14.5$ mm^3
2	Digital Image Resolution	36.1pixels/mm
3	Objective Focal Length	75mm
4	f-stop (f#)	11 for all cameras
5	Laser pulse separation time (dt)	$0.8\,\mu$s
6	Final Interrogation volume	$48 \times 48 \times 48$ voxels^3
7	Ensemble size	200

Table 3.6: Tomographic-PIV recording parameters

Expt No	Test Case	Mach Number M_∞	Unit Reynolds number	Micro-ramp configuration	Micro-ramp height h in mm	Location of micro-ramp(s) x_{MR}
1	Undisturbed Boundary Layer	2	43.5×10^6	-	-	-
2	Uncontrolled SWBLI	2	43.5×10^6	-	-	-
3	Controlled SWBLI	2	43.5×10^6	Single	3	17.3δ
4	Controlled SWBLI	2	43.5×10^6	Single-row array	3	17.3δ
5	Controlled SWBLI	2	43.5×10^6	Double-row staggered array	3	17.3δ

Table 3.7: Test matrix for Tomographic-PIV. Both laser pulses were set to 100%

Chapter 4

Boundary Layer study

Before the investigation of the effect of micro-ramps on the separation behaviour of SWBLI, first the undisturbed boundary layer or the boundary layer which enters the interaction is characterized. The boundary layer velocity profile and the boundary layer conditions are discussed in section (4.1). In section (4.2), the velocity fluctuations in the boundary layer are discussed.

4.1 Boundary layer Velocity Profile

The boundary layer developed to a thickness of 5.2 mm in the test section and the boundary layer velocity profile is shown in figure (4.1). The boundary layer thickness is in agreement with the boundary layer thickness (5.2mm) obtained by Giepman *et al* [19] for the same freestream Mach number in the same flow facility through planar-PIV.

In the present study, the first data point is 0.3δ from the wall location, which would lead to a wrong estimate of the boundary layer properties. Hence the near wall velocities are obtained by an approximation of the form :

$$u_{\text{near wall}}(\text{y}) = \text{a}\text{y}^{b}.$$

This power-law approximation comes from the log-law and the first four measurement points were considered to determine the values of a and b. For this study, b = 0.13 which is in agreement with Schlichting *et al* [37] according to whom b $\approx 1/7$ (or0.14).

The incompressible displacement thickness and momentum thickness thus calculated are $\delta_i^* =$ 0.67 mm and $\theta_i = 0.51$ mm. This results in a shape factor $H_i = 1.3$ which is typical for turbulent boundary layers [46].

The mean boundary layer velocity profile is transformed into an effective velocity u_{eq} using the van Driest compressibility transformation for an adiabatic flow as discussed earlier in Chapter (2) section (2.2). The van Driest compressibility transformation was used in combination with the Crocco-Busemann relation with a recovery factor r = 0.89 which is typical for turbulent flows according to [46]. The corresponding law of the wall fit for the present experimental data is shown in figure (4.2).

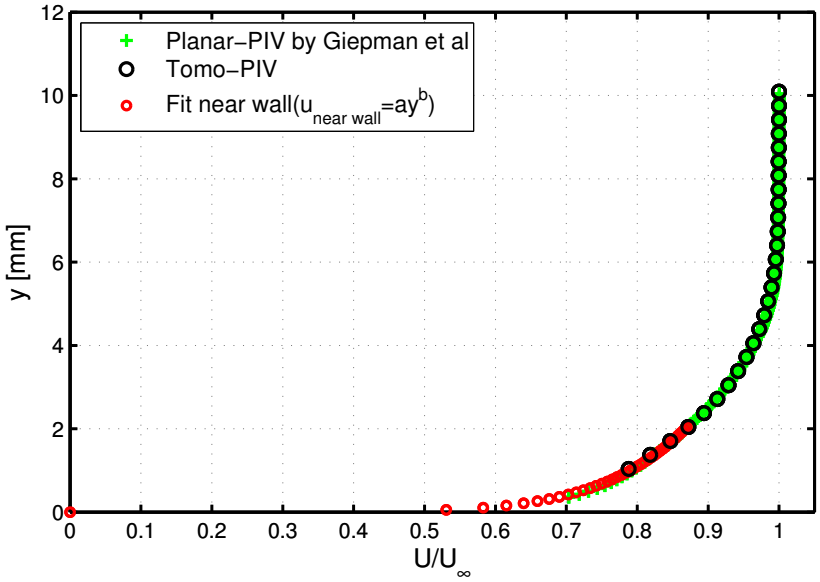

Figure 4.1: Boundary layer velocity profile, profile from Giepman*et al* [19] is included for comparison.

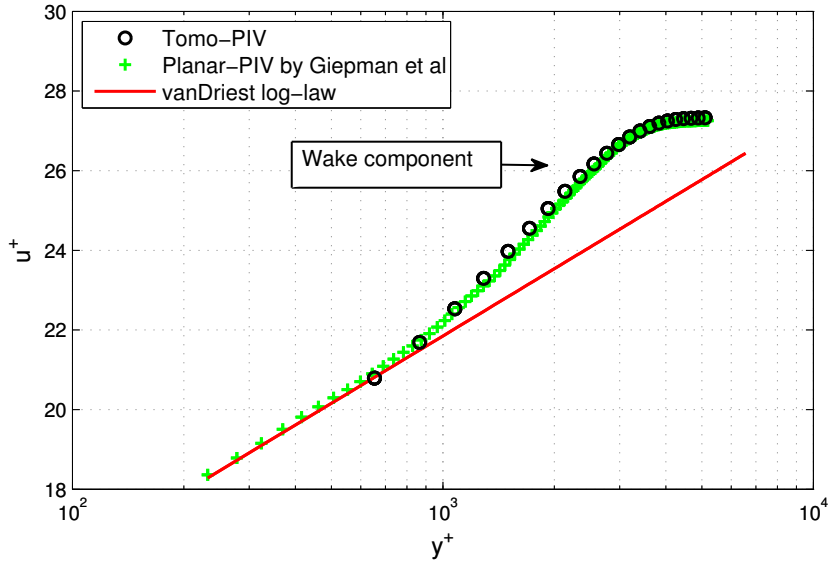

Figure 4.2: Comparison with van Driest log-law and Giepman *et al* [19]

The experimental effective velocity profile coincides with the theoretical velocity profile when a wall friction velocity $u_\tau = 19.6$ m/s is used. The corresponding skin friction co-efficient C_f was determined to be 1.9×10^{-3}. From $y^+ = 650 \sim 900$, the velocity profile is in close agreement with the log-law fit and for $y^+ > 900$ a wake component can be distinguished. When compared to the results of Giepman *et al* [19], it can be observed that the log-law region from $y^+ > 300$ to $y^+ < 650$ is not resolved in the present results. This is due to the limited resolution of the experiment. The log-law profile is in agreement with the results of Giepman *et al* [19] in the entire region recorded.

All the undisturbed boundary layer conditions are tabulated in table (4.1). The undisturbed boundary layer properties from the planar-PIV investigation of Giepman *et al* [19] are also included for comparison.

Sl no	Parameter	Tomo-PIV	Planar-PIV Giepman *et al*[19]
1	M_∞	2	2
2	U_∞ (m/s)	492	524
3	p_0 (N/m^2)	3.2×10^5	3.2×10^5
4	T_0(K)	278	290
5	δ_{99} (mm)	5.2	5.2
6	δ_i^* (mm)	0.67	0.63
7	θ_i (mm)	0.51	0.52
8	H_i	1.3	1.2
9	u_τ (m/s)	19.6	20.8
10	τ_w (N/m^2)	21.1	23.7
11	C_f	1.9×10^{-3}	1.9×10^{-3}
12	Re_∞ (1/m)	43.5×10^6	42.2×10^6
13	Re_θ	22×10^3	21.8×10^3

Table 4.1: Undisturbed Boundary Layer conditions, the planar-PIV results from Giepman *et al*[19] are shown for comparison.

4.2 Velocity Fluctuations in the boundary layer

The turbulent properties are important to characterize the boundary layer and are essential to substantiate the validity of the PIV measurements. The fluctuations in the undisturbed

boundary layer were normalized by the wall friction velocity u_τ. To take into account the variation of density in the boundary layer and to compare the results with the incompressible data of Klebanoff [24], the normalized fluctuations were multiplied by $\sqrt{(\frac{\rho}{\rho_w})}$ according to the Morkovin's hypothesis [29]. The local mean density was calculated from the local mean velocity using the adiabatic Crocco-Busemann relationship with a recover factor r = 0.89. The fluctuations are shown in figure (4.3) and were calculated as:

$$\text{Streamwise: } \sqrt{\frac{\rho}{\rho_w}}\frac{\sqrt{\overline{u'^2}}}{u_\tau} \quad \text{Spanwise: } \sqrt{\frac{\rho}{\rho_w}}\frac{\sqrt{\overline{v'^2}}}{u_\tau} \quad \text{Wall normal: } \sqrt{\frac{\rho}{\rho_w}}\frac{\sqrt{\overline{w'^2}}}{u_\tau} \tag{4.1}$$

In figure (4.3), the streamwise fluctuations (u′) are higher than the wall normal (v′) and

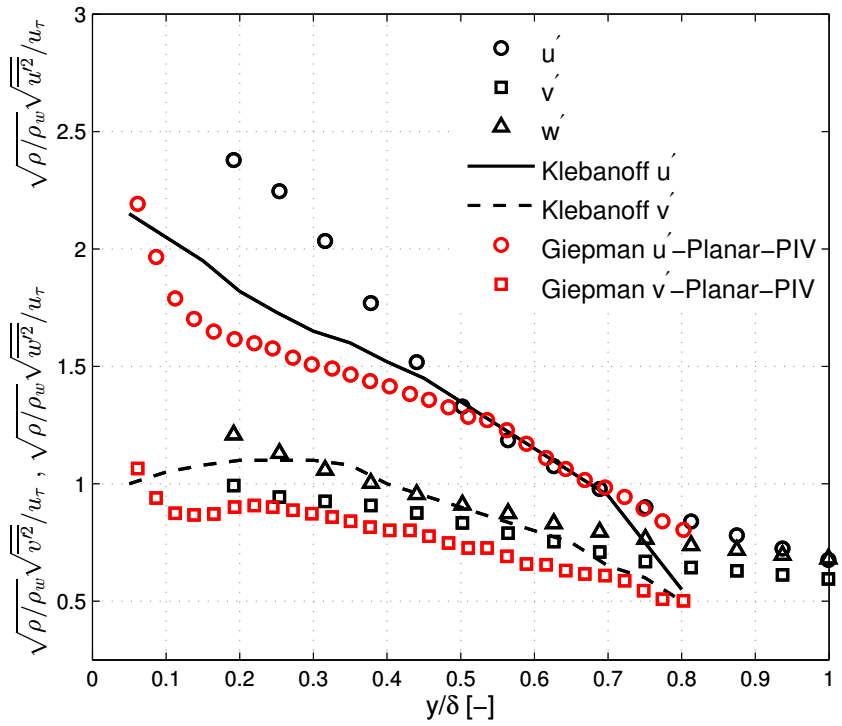

Figure 4.3: Velocity fluctuations in the boundary layer, profiles from Klebanoff [24] and Giepman *et al*[19] are included for comparison.

spanwise (w′) fluctuations in the entire boundary layer. Further, the wall normal fluctuations are lower than the spanwise fluctuations. At the wall, due to the no-slip condition, all the fluctuations reduce to zero. Due to the limited resolution of the experiment, this has not been recorded. At the edge of the boundary layer ($y/\delta \approx 1$), all the fluctuations reduce to the freestream turbulence intensity level.

When compared to the results of Klebanoff [24], it is seen that the streamwise fluctuations are larger in the region $y/\delta < 0.5$. This can be attributed to the wall effects of PIV. However, in the region $y/\delta > 0.5$, the streamwise fluctuations are in close agreement with Klebanoff [24] and Giepman *et al* [19]. In contrast, the wall normal fluctuations are slightly lower than

Klebanoff [24] in the region $y/\delta < 0.5$ and form a closer match with Giepman *et al* [19]. This can be due to the limited applicability of the Morkovin's hypothesis for the wall normal fluctuations [40].

In conclusion, the log-law profile and the velocity fluctuations in the the undisturbed boundary layer are in agreement with the results of Klebanoff [24] and Giepman et al. [19]. Therefore the boundary layer can be termed as a standard turbulent boundary layer.

Chapter 5

Micro-ramp flow features

In this chapter, first a brief discussion of the flow features generated by a micro-ramp are discussed in section (5.1). This is followed by the surface oil flow visualizations performed for the horseshoe vortex study in section (5.2).

5.1 Flow topology

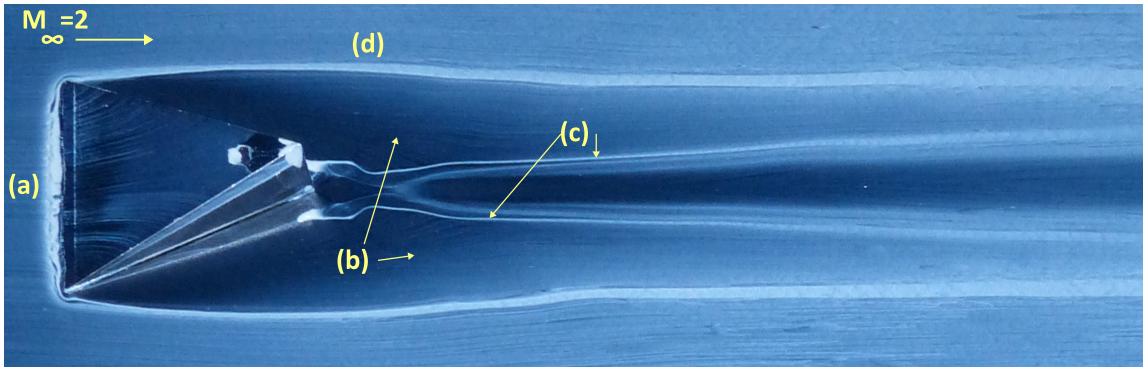

Figure 5.1: Surface oil flow pattern for a micro-ramp of h= 6mm and $\alpha = 8.6°$. Flow direction is from left to right. (a) Leading edge oil accumulation (b) Primary vortex pair (c) Secondary vortex pair (d) Bright streaks (thought to be) due to horseshoe vortex

Figure (5.1) shows the surface oil flow pattern for a h= 6mm micro-ramp with a ramp angle of $\theta = 8.6°$ mounted in a $M_\infty = 2$ flow. At the leading edge of the micro-ramp a shock wave is formed due to the ramp angle of the micro-ramp. The incoming boundary layer experiences the adverse pressure gradient due to the shock wave and a region of oil accumulation can be seen just upstream of the micro-ramp's leading edge labelled as 'a' in the figure.

For similar oil applications, surface oil flow visualizations of Babinsky et al. [6], Saad et al.

[34] and Herges et al. [20] show the accumulation of oil upstream of the micro-ramp leading edge. According to Babinsky et al. [6], the flow close to the leading edge of the micro-ramp is separated. The separated flow seen as an oil accumulation at the leading edge, forms a horseshoe vortex, wraps around the leading edge and trails downstream. This can be seen as bright oil streaks on either sides of the micro-ramp wake labelled 'd' in figure (5.1).

The flow moving down the edges of the micro-ramp forms large vortices, one on either side of the micro-ramp symmetry plane, and together they are referred to as the primary counter-rotating vortices.

The primary counter-rotating vortices which form the principal flow features are visualized as dark regions that begin from the sides of the micro-ramp, indicated by 'b' in figure (5.1). In this region, due to the high shear of the counter-rotating vortices the oil is swept away. Due to the upwash induced by the two counter-rotating vortices on each other, they are lifted away from the wall as they move downstream. The secondary vortex pair formed between the micro-ramp side wall and the test section floor junction can also be observed in the oil flow pattern indicated by (c).

It is important to note that, in the experiments of Babinsky *et al* [6] and Herges *et al* [20] oil was applied both upstream and downstream of the micro-ramp (as in the oil pattern in figure(5.1)). In the following section,oil flow patterns in the absence of oil upstream of the micro-ramp leading edge are discussed.

5.2 Horseshoe vortex study

To study the separation behaviour of the flow at the micro-ramp leading edge, surface oil flow visualizations were performed for micro-ramps of increasing ramp angles. A stronger leading edge shock wave would be formed for higher ramp angles. This leads to a larger upstream influence and an increase in the streamwise extent of the interaction. In figures (5.2a-b), figures (5.3a-b), figures (5.4a-b), figures (5.5a-b) and figures (5.6a-b), the surface oil flow pattern for micro-ramps of ramp angle $\theta = 4.3°, 8.6°, 13°, 17.3°$ and $21.6°$ are presented. The labels 'a, b' correspond to experiments with oil applied everywhere and oil applied only downstream of the leading edge, respectively.

According to Kuehn's [25] threshold for incipient separation, separated flow regions are formed if $\theta_{inc} > 15°$ for the given experimental conditions. According to this criterion, separated flow regions (and hence horseshoe vortex) are formed only for micro-ramps of ramp angles $17.3°$ and $21.6°$. Hence with oil applied only downstream of the micro-ramp, bright streaks indicative of the horseshoe vortex must be present for $17.3°$ and $21.6°$ micro-ramps.

In figures (5.2a) - (5.6a) i.e oil applied everywhere, it can be seen that the streamwise extent of the interaction region ahead of the micro-ramp leading edge increases with increasing ramp angles as expected. In figures (5.2a) - (5.6a), the bright oil streaks indicating a horseshoe type structure are clearly visible on either sides of the micro-ramp. This is true even for

micro-ramps with $\theta < 15°$. However, these bright streaks disappear from the oil flow patterns in the absence of the oil upstream shown in figures (5.2b) - (5.6b).

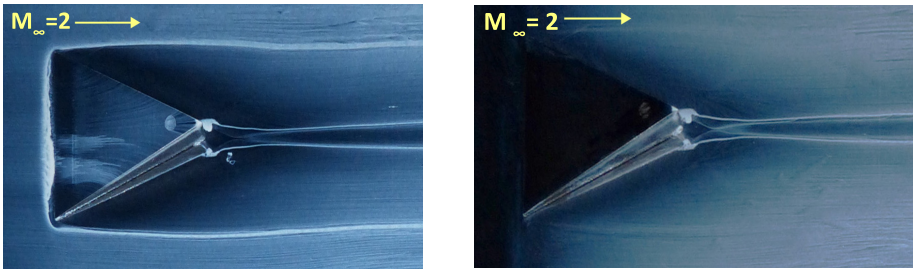

(a) (b)

Figure 5.2: Micro-ramp with ramp angle $\theta = 4.3°$, (a) oil applied everywhere (b) oil applied only downstream.

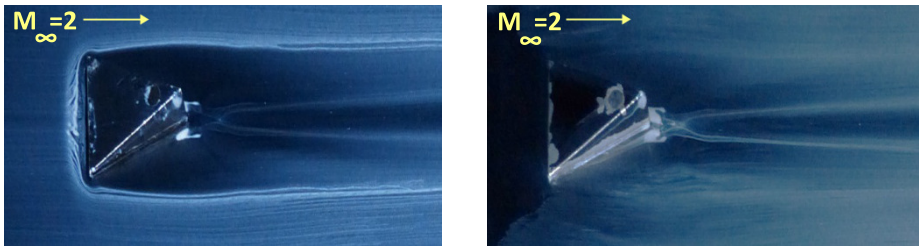

(a) (b)

Figure 5.3: Micro-ramp with ramp angle $\theta = 8.6°$ (Standard micro-ramp with h= 3mm),(a) oil applied everywhere (b) oil applied only downstream.

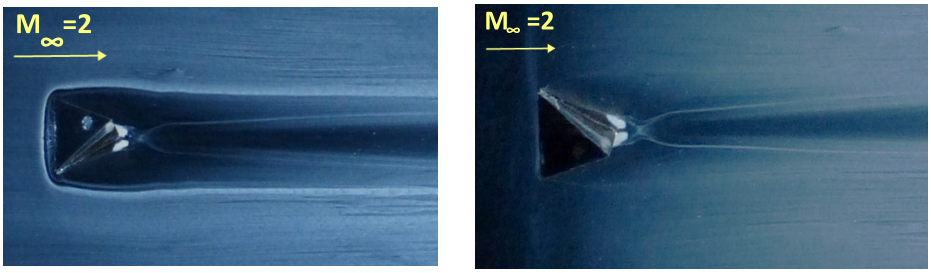

(a) (b)

Figure 5.4: Micro-ramp with ramp angle $\theta = 13°$, (a) oil applied everywhere (b) oil applied only downstream.

It is important to note that, Kuehn's [25] incipient separation threshold is applicable for a 2D object which extends outside the boundary layer and not for a 3D object like the micro-ramp which is embedded inside the boundary layer. Hence, for the micro-ramps with $\theta < 15°$ (figures (5.2a) - (5.4a)), it is not very clear whether the flow upstream has separated. Since

the micro-ramp is inside the boundary layer and the effective Mach number is lower than M_∞, there may be separated flow regions forming a horseshoe vortex [28].

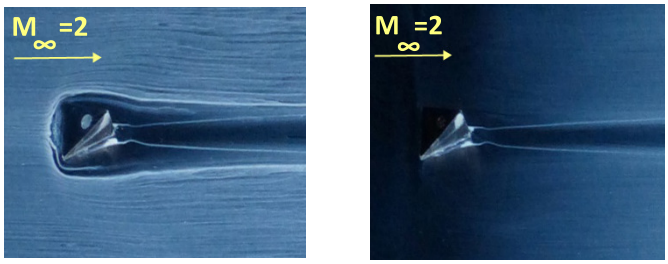

(a) (b)

Figure 5.5: Micro-ramp with ramp angle $\theta = 17.3°$, (a) oil applied everywhere (b) oil applied only downstream.

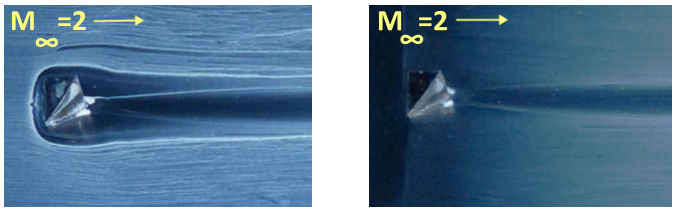

(a) (b)

Figure 5.6: Micro-ramp with ramp angle $\theta = 21.6°$, (a) oil applied everywhere (b) oil applied only downstream.

Importantly, for micro-ramps with ramp angles greater than the incipient separation threshold $\theta > 15°$ in figures (5.5b) and (5.6b), where it is certain that separated flow region exists upstream of the leading edge, no bright streaks are visible with oil applied only downstream of the micro-ramp. Therefore, the horseshoe vortex may be a very weak flow feature.

Additionally, the bright oil streaks in the oil flow pattern with oil applied everywhere (figures (5.2a) - (5.6a)) may be due to converging skin friction lines and not due to a horseshoe vortex. Due to the adverse pressure of the leading edge shock, some of the incoming flow moves towards the edges of the micro-ramp. Because of this, the skin friction lines converge close to the micro-ramp corners. Since the oil flowing between two skin friction lines has to be conserved, the height of the oil lines increases. Such converging lines lead to an accumulation of oil which trails downstream and forms oil streaks on either sides of the micro-ramp wake. These streaks closely resemble the oil flow pattern which would form in the presence of a horseshoe vortex, leading to a misinterpretation of the surface oil flow pattern.

For further investigation, surface oil flow visualization was performed for a standard micro-ramp, with height h= 6mm in $M_\infty = 2$ boundary layer for both the oil applications. With the increase in the height of the micro-ramp, the flow features also increase in size. Therefore, the horseshoe vortex if present, must be more clear in this oil flow pattern. From figure (5.7b), it can be seen that when oil is applied only downstream of the micro-ramp, the bright streaks

of oil in figure (5.7a) representing a horseshoe vortex type structure, disappear from the oil flow pattern as in the previous cases.

Therefore, the horseshoe vortex may not be a physical flow feature (or maybe a very weak flow feature even for large ramp angles) but only an artefact of the visualization technique leading to a misinterpretation of the flow features.

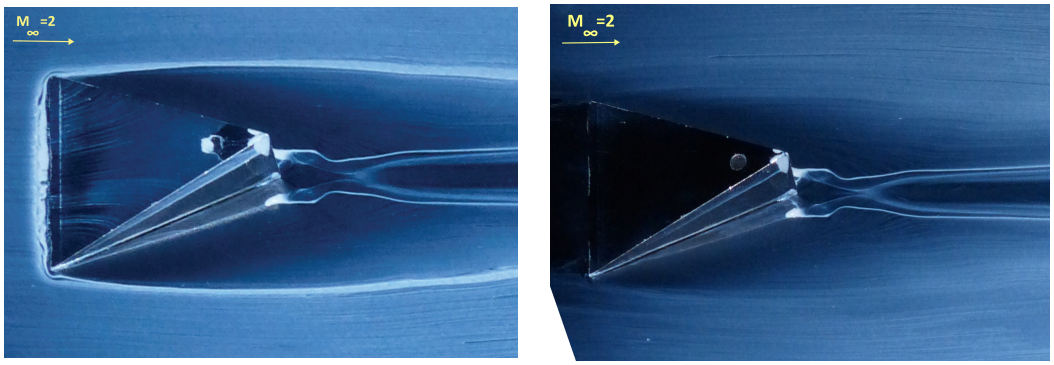

(a) (b)

Figure 5.7: Micro-ramp of height $\theta = 8.6°$ and h = 6mm (a) oil applied everywhere (b) oil applied only downstream.

Chapter 6

Global Flow features of the interaction

6.1 Introduction

In the previous chapter, surface oil flow patterns of micro-ramp flow were discussed. This chapter presents the preliminary results of micro-ramp controlled interaction. The uncontrolled interaction results are also presented and form a reference to understand micro-ramp effects.

Section (6.2) presents the results from Schlieren visualization for both the uncontrolled and single micro-ramp controlled interaction. The surface oil flow patterns for uncontrolled and single micro-ramp controlled interactions are presented in section (6.3). Further, flow features generated by micro-ramp arrays: single-row array and double-row staggered arrays are also presented in section (6.3).

6.2 Schlieren visualization

Figure (6.1) presents the Schlieren image for the uncontrolled interaction. In figure (6.1), the incident shock wave can be seen distinctly as a sharp dark line indicated by (1). The incoming boundary layer is labeled as (2) and the interaction region is indicated by (3) in the figure. Due to this density gradient in the boundary layer, the boundary layer is brighter than the freestream. It can be seen from figure (6.1) that the boundary layer becomes thicker after the interaction.

The reflected shock wave (4) can be seen as a dark band. At the intersection of the incident shock wave and the reflected shock wave, a slip line emanates. The magnitude of velocity on either side of the slip line is different. Because of this velocity gradient,the slip line can be observed as a bright line indicated by (5) in the figure. Close to the reflected shock wave, a

bright region can be observed. This indicates an expansion fan which is formed due to the reflection of the incident shock wave at the M = 1 isoline. Due to this expansion fan, the detached shear layer is turned towards the wall. The shear layer experiences deceleration while passing through the compression waves. The compression waves coalesce together to form a reattachment shock. The reattachment shock is visualized as a dark region after the expansion fan in figure (6.1).

The flow that has gone through the shock system and the expansion fan undergoes recovery process further downstream. However, it does not recover to the initial conditions within the measurement region. It is seen that the boundary layer at the end of the measurement region is thicker compared to the boundary layer entering the interaction region.

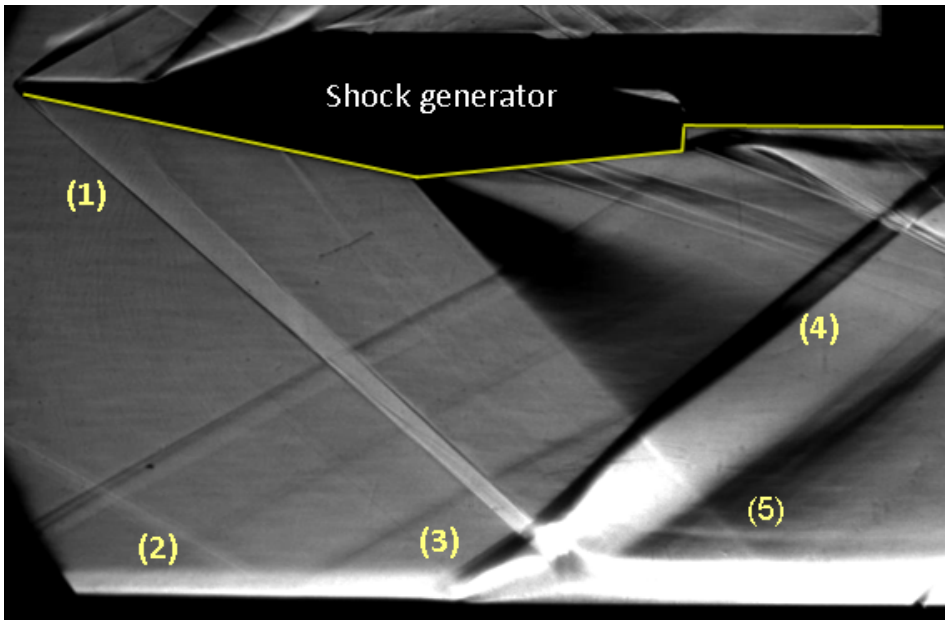

Figure 6.1: Schlieren image of uncontrolled interaction. Flow direction is from left to right (1) Incident shock wave (2) Boundary layer (3) Interaction region (4) Reflected shock wave (the bottom edge of the shock generator is marked by a yellow line for clarity)

Figure (6.2) shows the schlieren image for a single micro-ramp controlled interaction, with the micro-ramp placed 17.3δ upstream of the inviscid shock impingement location. When compared to the uncontrolled schlieren image, two additional shock waves that are generated by the micro-ramp itself are clearly visible. These are the micro-ramp leading edge shock and the trailing edge lip shock, and can be observed as dark lines indicated by (1) and (2). Additionally, the wake from the micro-ramp can also be observed as a faint bright line in the image indicated by (5).

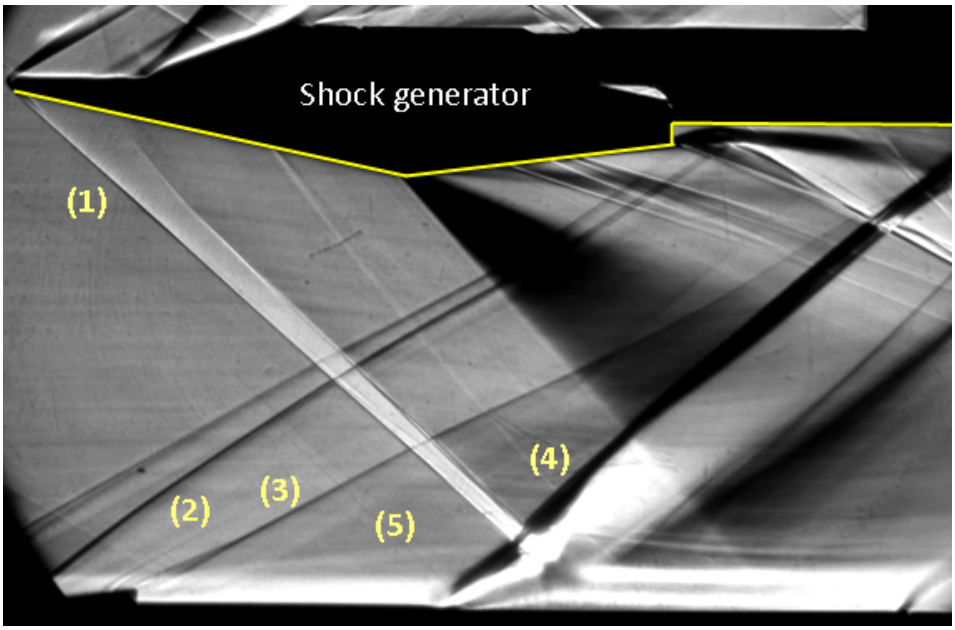

Figure 6.2: Schlieren image of single micro-ramp controlled interaction, micro-ramp placed at $x_{MR} = 17.3\delta$. Flow direction is from left to right (1) Incident shock (2) Micro-ramp leading edge shock (3) Micro-ramp trailing edge shock (4) Reflected shock wave (5) Micro-ramp wake.

6.3 Surface Oil flow visualization

The surface oil flow patterns for the uncontrolled interaction and single micro-ramp controlled interaction are shown in figure (6.3a-b), respectively. Due to the 3D effects caused by the tunnel side walls and the limited span of the shock generator (120 mm, 23δ), oil flow pattern only from z = -9.6δ to z = 9.6δ is considered. The measurement region considered is marked by a yellow rectangle in the following surface oil flow patterns. The surface oil flow pattern is smeared due to the shock at the end of the tunnel run. However, by comparing the final surface oil flow pattern with the video taken during the tunnel run, it is seen that the smearing does not alter the flow features significantly.

In figure (6.3a), (1) indicates the separation line which is visualized as a thick bright line. Due to converging skin-friction lines, oil accumulates from opposite directions at the separation line. (2) indicates the re-attachment line. The skin friction pattern close to the re-attachment line is very similar to the pattern at the separation line. However, on either side of the re-attachment line the skin friction lines diverge which causes a relatively faint appearance of the re-attachment line. The region between the separation and the reattachment lines indicates the separation bubble consisting of recirculating fluid.

The streamwise extent of the separation bubble is recorded manually by measuring the distance between the separation and re-attachment lines. These values are plotted in figure (6.4). At the tunnel centreline, the separation bubble is approximately $\approx 7\delta$) long. The

streamwise extent of the separation bubble increases while moving away from the centreline. The maximum length of the separation bubble was recorded to be $\approx 9\delta$ at $z/\delta \approx -5$. This is followed by a decrease in the streamwise extent of the separation bubble. Further, it is seen that the interaction remains largely symmetrical about the centreline of the tunnel.

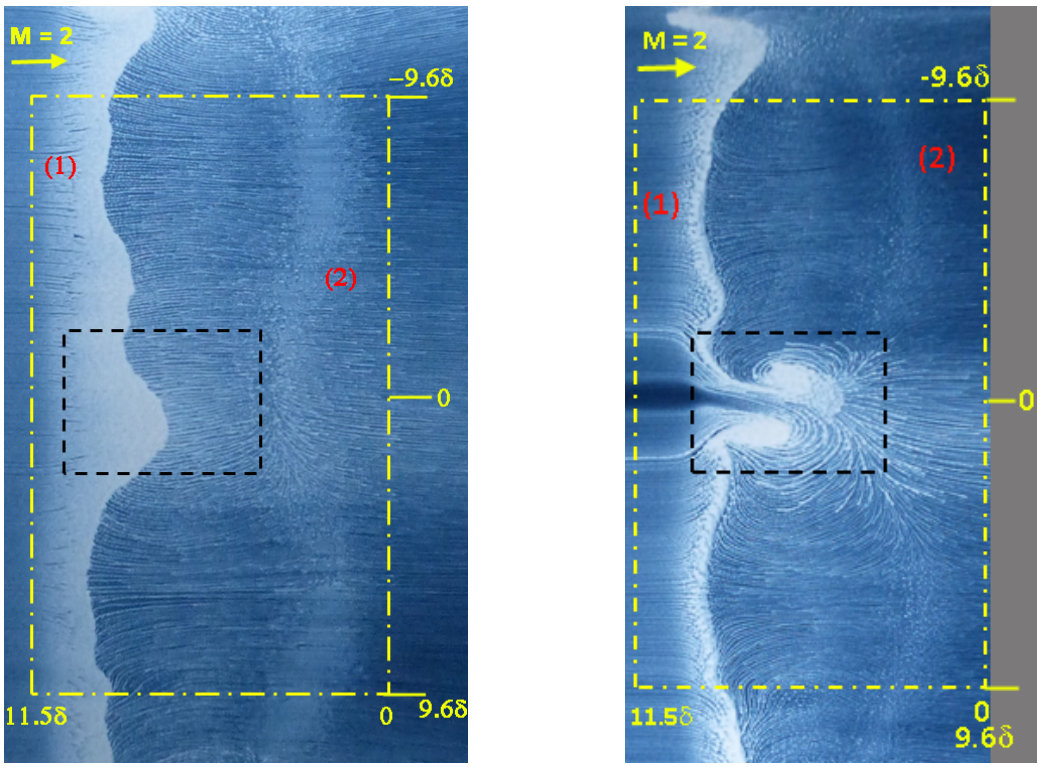

(a) Uncontrolled interaction

(b) Interaction controlled by a single micro-ramp placed at $x_{MR} = -17.3\delta$

Figure 6.3: Surface oil flow patterns. Flow is from left to right. Black dashed line represents the tomographic-PIV measurement region

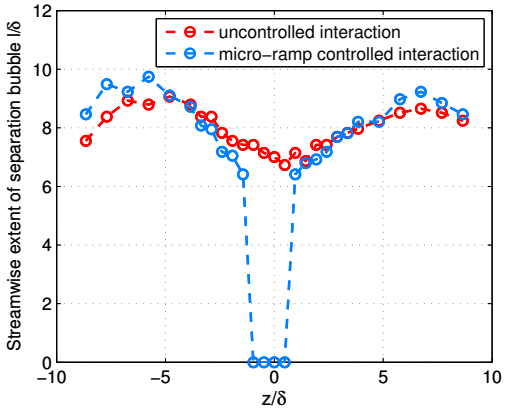

Figure 6.4: Streamwise extent of the separation bubble l/δ

From figure (6.3b), it is seen that the micro-ramp substantially alters the separation bubble.

Along the centreline of the micro-ramp, a thin channel of attached flow is seen and separation is seen away from the micro-ramp centreline. Thus the micro-ramp creates a spanwise modulation of the flow. The attached flow region spans from $z/\delta \approx -1$ to $z/\delta \approx 0.5$ and not directly downstream of the micro-ramp centreline. Hence, it appears that the flow topology generated by the micro-ramp is not precisely symmetrical as also observed by Babinsky et al. [6] in their oil flow patterns.

At outboard locations $z/\delta = -6$ and $z/\delta = 6$, the streamwise extent of the separation bubble increases when compared to the uncontrolled interaction. This can be observed in figure (6.4) at $z/\delta = -6$ and $z/\delta = 6$ where the streamwise extent of the separation bubble is approximately 9.7δ and 9.2δ respectively.

Additionally, two bright three dimensional structures are formed on either side of the centreline in the interaction region. The effectiveness of the micro-ramp at outboard locations is reduced. Hence, compared to the centreline boundary layer, the boundary layer at outboard locations are less full. Therefore, in the interaction region, the separated flow at outboard locations forms these structures. In the oil flow videos the oil is seen to be rotating in opposite directions in this particular region.

Further, Babinsky et al. [6] have noted an 'owl-face separation' [31] in the interaction region on either sides of the micro-ramp-centreline. However, the present single micro-ramp controlled oil flow patterns do not show such structures. In conclusion, it appears that substantial

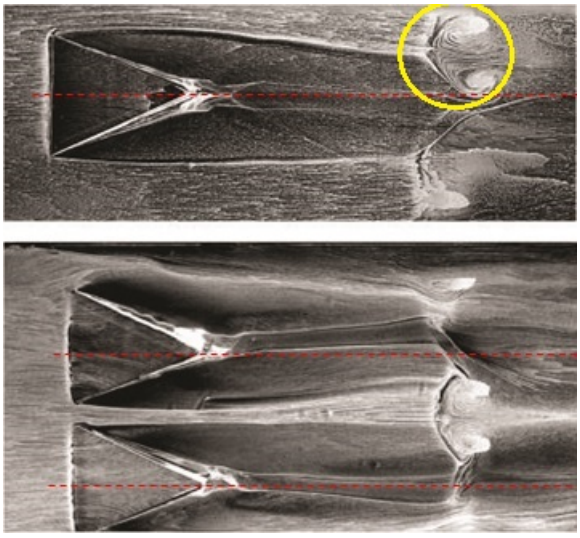

Figure 6.5: Surface oil-flow pattern for h = 6 mm micro-ramp from Babinsky et al. [6]. Owl-face marked by yellow cirle.

benefit is achieved in reduction of the streamwise extent of the separated flow by employing micro-ramp control.

6.4 Micro-ramp arrays

For boundary layer control in practical situations, arrays of micro-ramps will be required since the effectiveness of micro-ramps reduces away from their centrelines. The qualitative flow features of the interaction controlled using micro-ramp arrays forms the topic of this section. Figures (6.6a-b) show the surface oil flow pattern for a single-row micro-ramp array and a double-row staggered micro-ramp array respectively. Grey triangles are indicative of the spanwise location of micro-ramps and are not exact to scale. For the exact geometry of the arrays, the reader can refer to chapter (3), section (3.2).

Both the micro-ramp arrays create a complex flow pattern in the interaction region by partitioning the separation bubble into a three dimensional cellular structure. This partitioning is due to thin channels of attached flow that are found at locations corresponding to the micro-ramp centrelines.

In case of the double-row configuration, it is important to note that attached flow channels are found only at centrelines of the second row of the array. At centrelines of the first row of the array, bright three dimensional structures of oil accumulation are seen. When an instantaneous snapshot of the oil flow pattern is taken from the oil flow video, it is observed that the structures downstream of the first row centrelines, correspond to the owl-face structures. This can be seen in figure (6.7).

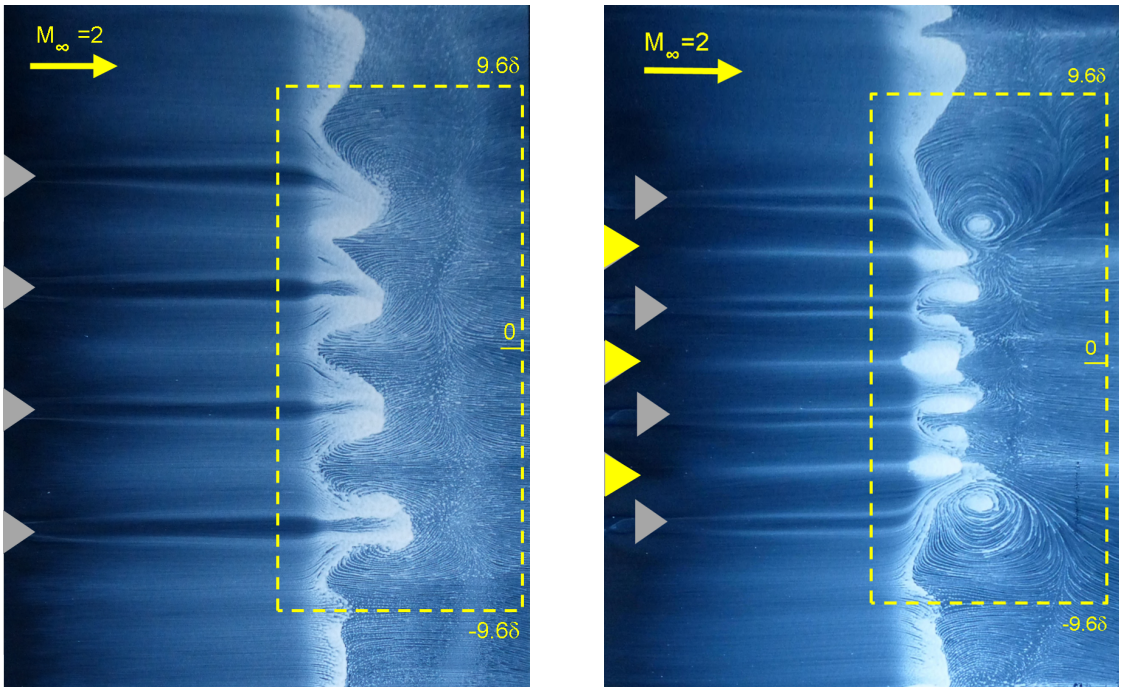

(a) single-row array placed at $x_{MR} = -17.3\delta$

(b) double-row staggered array placed at $x_{MR} = -17.3\delta$

Figure 6.6:
Surface oil flow patterns of SWBLI controlled by micro-ramp arrays. Grey triangles are indicative of micro-ramp spanwise positions and their size is not shown to scale. Yellow triangles represent the first row of the double-row array.

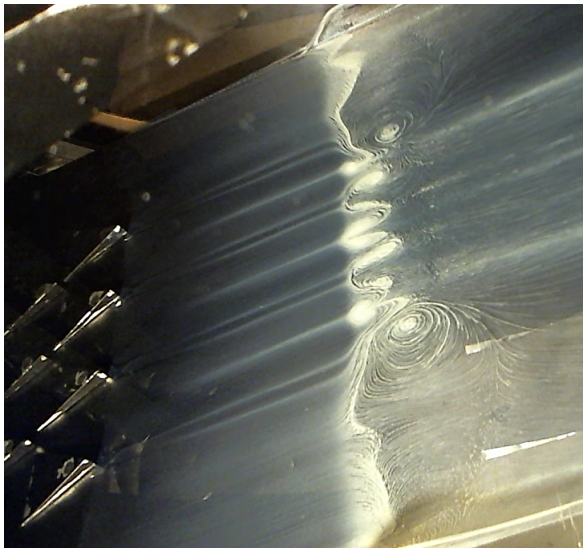

Figure 6.7: Instantaneous surface oil flow snapshot of double-row micro-ramp array

Chapter 7

Mean flow organization

7.1 Introduction

In the preceding chapter, the qualitative flow features in an uncontrolled interaction and single micro-ramp controlled interaction were discussed primarily. In the present chapter, the three-dimensional velocity fields obtained from the tomographic-PIV experiments are presented for both the uncontrolled interaction and a single micro-ramp controlled interaction.

Firstly, the mean flow organization of the uncontrolled interaction is discussed in section (7.2). This is followed by the mean flow organization of a single micro-ramp controlled interaction in section (7.3). The effect of the micro-ramp vortex generator on the interaction is understood using the spanwise, wall-parallel and crossflow planes in sections (7.4), (7.5) and (7.6) respectively. The main observations are noted in section (7.7) and the volumetric representation of the interaction is provided.

7.2 Uncontrolled interaction

Figure (7.1) describes the mean velocity pattern of the interaction using ensemble averaged streamwise (U/U_∞) and wall normal velocity components (V/U_∞) at $z/\delta = 0$. For clarity, only 1 in 4 mean velocity vectors are shown in the streamwise direction. In figure (7.1a), the mean velocity vectors in the incoming boundary layer are parallel to the wall. About 5δ upstream of the origin, the mean velocity vectors begin to deflect upwards due to the upstream influence of the incident shock wave. After this, the flow moves away from the wall, reaching a maximum wall normal velocity of $\approx 0.2U_\infty$ which can be seen in figure (7.1b).

The black solid line represents the $M = 1$ iso-line or the sonic line. The $M = 1$ iso-line envelopes the subsonic fluid. The incident shock wave is reflected as an expansion fan at the sonic line.

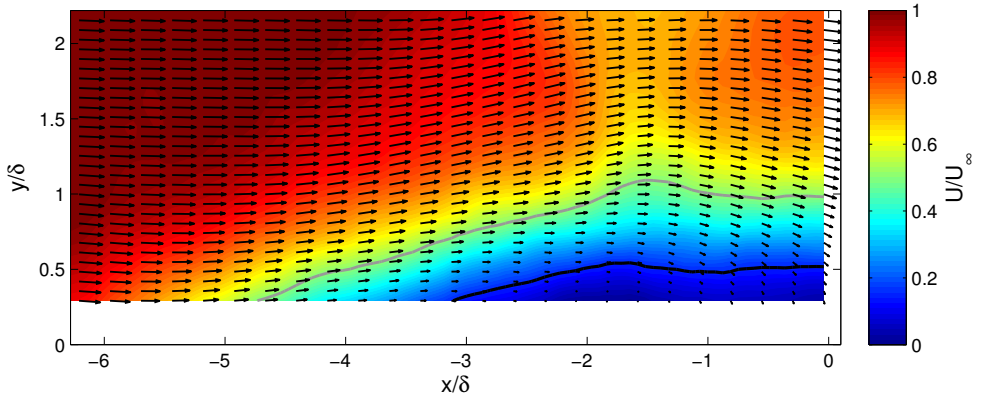

(a) Mean streamwise velocity component U/U_∞.

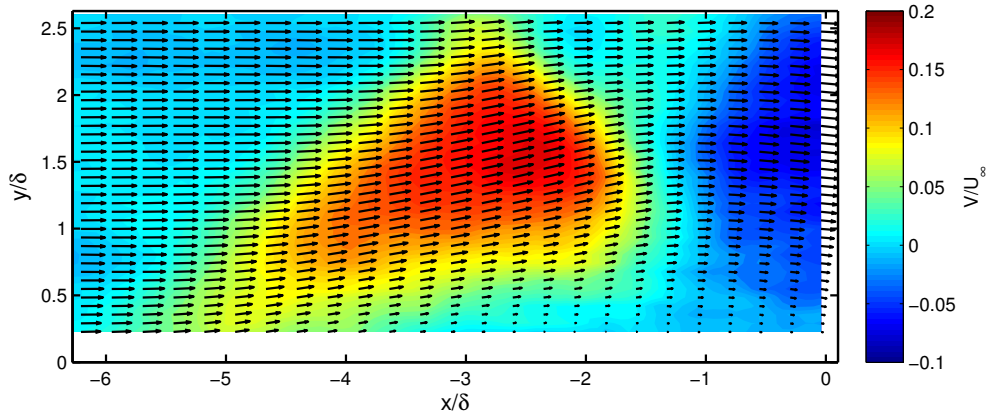

(b) Mean wall normal velocity component V/U_∞.

Figure 7.1: Mean velocity distribution at $z/\delta = 0$. Black line envelopes $U = 0.1U_\infty$ fluid and grey line represents the $M = 1$ sonic line. 1 in 4 mean velocity vectors shown in streamwise direction.

About 0.75δ upstream of the origin, the velocity vectors are deflected towards the wall. This is indicative of fluid returning towards the wall due to the expansion fan. The interaction length which is defined as the distance between the extrapolated intersection points of the incident and reflected shocks with the wall is about $L \approx 5.5\delta \approx 32$mm. Importantly, no reversed flow is observed at $y/\delta = 0.29$ in the mean velocity fields shown in figure (7.1a). However, higher resolution results from Giepman et al. [19] for the same experimental conditions show the presence of reverse flow in the interaction region at the same wall normal position. The reversed flow regions are not recorded in the tomographic-PIV mean flow results due to the limited resolution of PIV near the wall. While averaging over a PIV interrogation window small regions of reversed flow are masked as also found by Humble et al. [22]. Furthermore, since the reversed flow regions have not been recorded, a representative low velocity of $U_{0.1} = 0.1U_\infty$ is considered as a surrogate for separated flow in this thesis.

However, substantial reversed flow regions as large as $\approx 2\delta$ are found in instantaneous snapshots. Such an instantaneous tomo-PIV snapshot is shown in figure (7.2). Considered together

with the surface oil flow pattern (in figure (6.3)) which clearly shows separated flow, a small region of separated flow is known to be present in the interaction region though it is not recorded in the tomographic-PIV mean flow results.

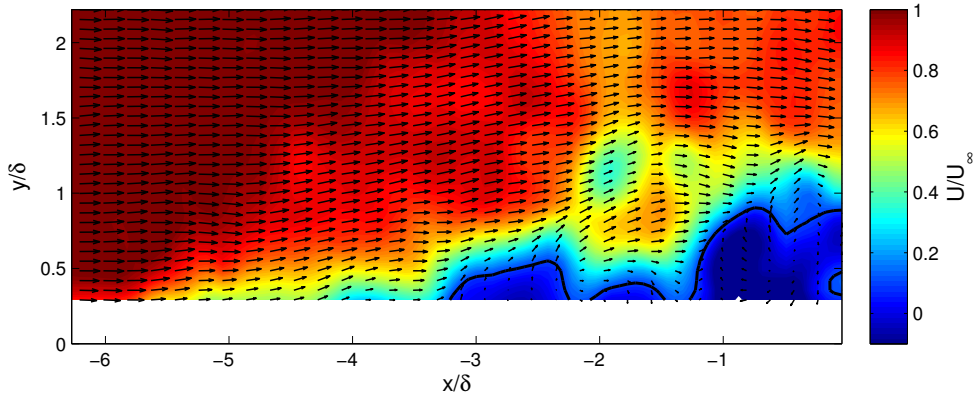

Figure 7.2: Instantaneous PIV snapshot at $z/\delta = 0$. The black solid line represents the zero-velocity iso-line.

7.3 Single micro-ramp controlled interaction

Figure (7.3) presents the ensemble averaged streamwise velocity component (U/U_∞) in a micro-ramp controlled interaction. The flow organization is shown at the micro-ramp centre-line or symmetry plane ($z/\delta = 0$). For clarity, only 1 in 4 mean velocity vectors are shown in the streamwise direction. The grey line indicates the M= 1 iso-line which envelopes the subsonic fluid. Due to the action of the counter-rotating vortices, the boundary layer entering the interaction zone is fuller. This can be seen in figure (7.4a). Close to the wall, the boundary layer with micro-ramp control is fuller than the boundary layer with no control. A velocity deficit region is also observed which is representative of the micro-ramp wake. Due to a fuller boundary layer velocity profile, the subsonic part of the boundary layer is thinner which leads to lesser upstream influence from the incident shock wave. The velocity vectors are deflected away from the wall at $x/\delta \approx 5$.

Further, due to the upwash induced by the counter-rotating vortices on each other, the vortices move away from the wall as they move downstream [6]. This can be seen in figure (7.4b) which shows the velocity profiles at different streamwise locations. While moving downstream, it is clear that the velocity deficit region or the micro-ramp wake moves away from the wall. This micro-ramp wake interacts with the incident shock wave between $x/\delta \approx -3$ and -2, and forms a low velocity pocket between $y/\delta = 1.5$ and 2.3.

From the previous paragraphs it is understood that, on average micro-ramp eliminates the separation bubble at the centreline. However, instantaneously separated flow regions as large as $\approx 3.5\delta$ are observed at the symmetry plane, as shown in figure (7.5). This is because

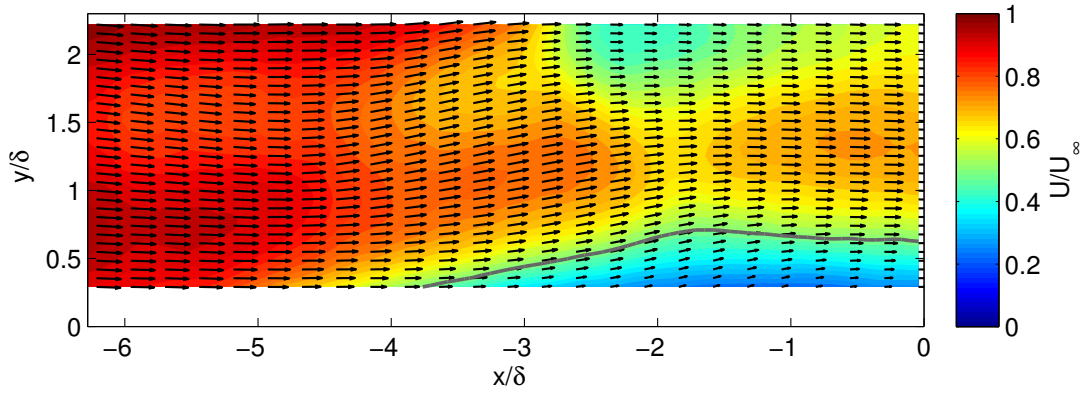

Figure 7.3: Mean streamwise velocity component distribution U/U_∞ at $z/\delta = 0$ for h = 3 mm micro-ramp placed at $x_{MR} = -17.3\delta$. Grey line indicates the M = 1 iso-line.

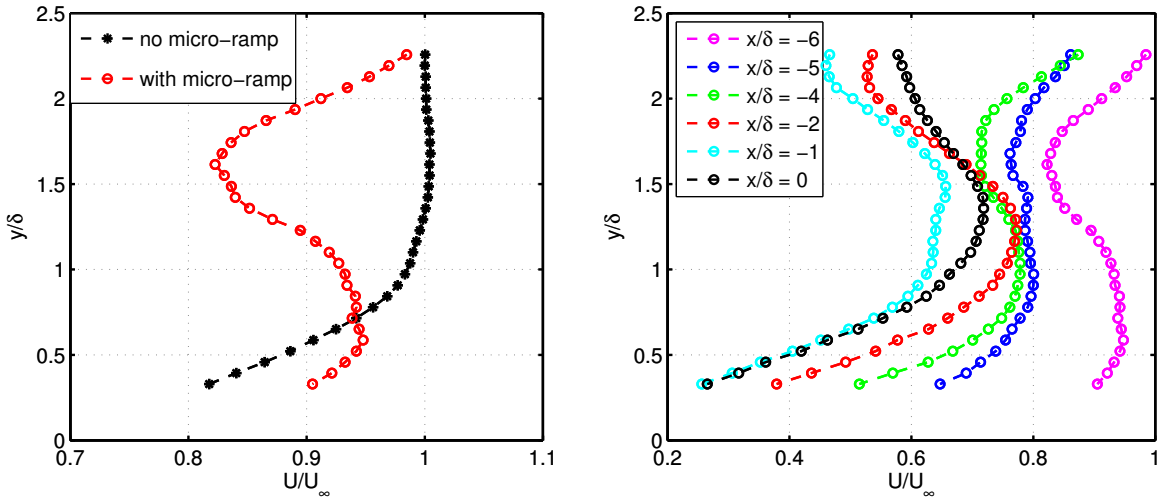

(a) Boundary layer profiles at $x/\delta = -6.2$ for uncontrolled and micro-ramp controlled interaction

(b) Velocity profiles for micro-ramp controlled interaction at $z/\delta = 0$

Figure 7.4: Boundary layer velocity profiles at micro-ramp centreline $z/\delta = 0$, h = 3 mm micro-ramp placed at $x_{MR} = -17.3\delta$

the counter-rotating vortices show significant variations in their spanwise location in the instantaneous flow as noted by Sun et al. [42]. Therefore, due to the meandering effect of the counter-rotating vortices, instantaneously separated flow is found even along the micro-ramp centreline.

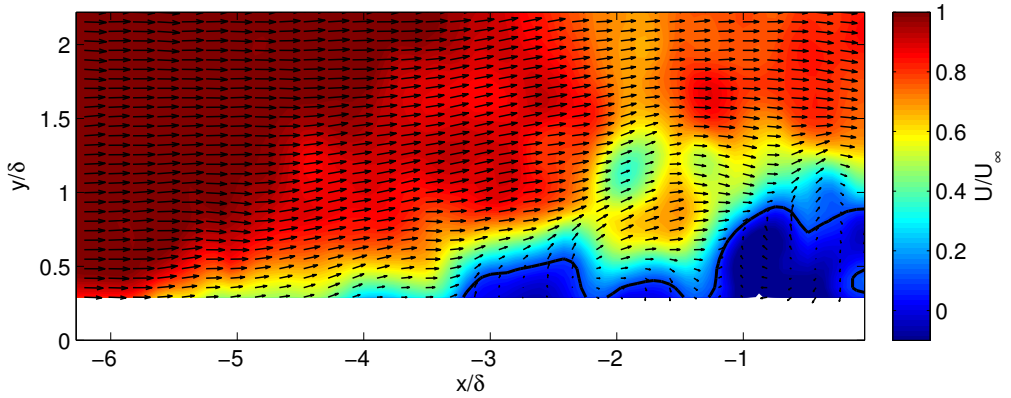

Figure 7.5: Instantaneous streamwise velocity contours at micro-ramp symmetry plane $z/\delta = 0$ showing a large separation bubble

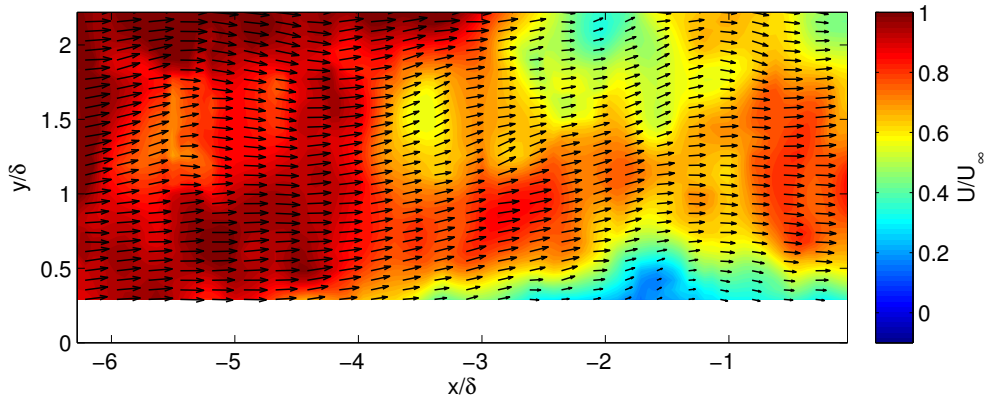

Figure 7.6: Instantaneous streamwise velocity contours at micro-ramp symmetry plane $z/\delta = 0$ showing attached flow

7.4 Micro-ramp effects: Spanwise planes

Though the micro-ramp completely eliminates the separation bubble at the symmetry plane, its effectiveness reduces while moving outboard [6]. Figure (7.7) illustrates the streamwise velocity contours at outboard locations corresponding to 25% ($z/\delta = \pm 0.96$) micro-ramp span.

From figure (7.7) it appears that the micro-ramp flow is not symmetric about the micro-ramp centre plane. At $z/\delta = -0.96$ (top figure) the micro-ramp wake is faintly visible. Additionally, the low velocity pocket formed due to the interaction of the micro-ramp wake and the incident shock wave is also seen. Though no $U_{0.1}$ regions are found at $z/\delta = -0.96$, a distinct $U_{0.1}$ bubble of the size $\approx \delta$ is seen at $z/\delta = 0.96$ (bottom figure).

This can be further illustrated by plotting the velocity profiles at two different streamwise stations in the low velocity region. Figure (7.8a-b) show the velocity contours at x/ = −3

and −1 respectively. The velocity profiles at a given streamwise location are not identical at ±25% span and show significant differences between each other. However, this behaviour of the micro-ramp flow is not expected due to the geometrical symmetry of the micro-ramp. Further the flow symmetry has been validated by Sun [41].

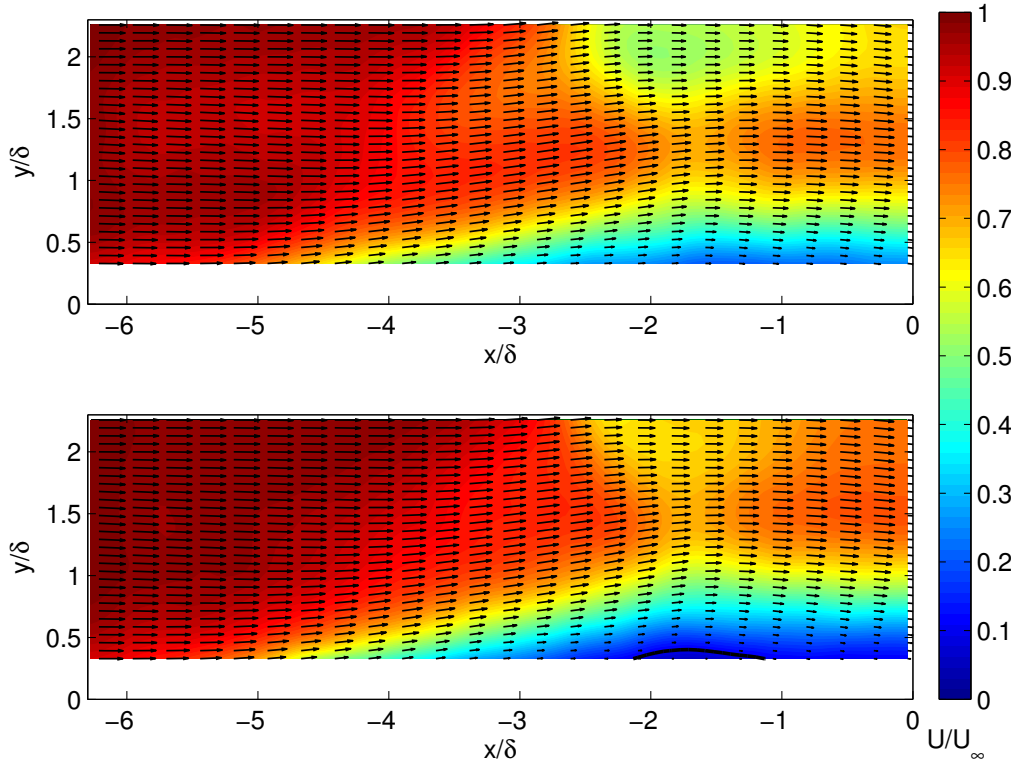

Figure 7.7: Streamwise velocity component at 25% micro-ramp span, Top: $z/\delta = -0.96$, Bottom: $z/\delta = 0.96$

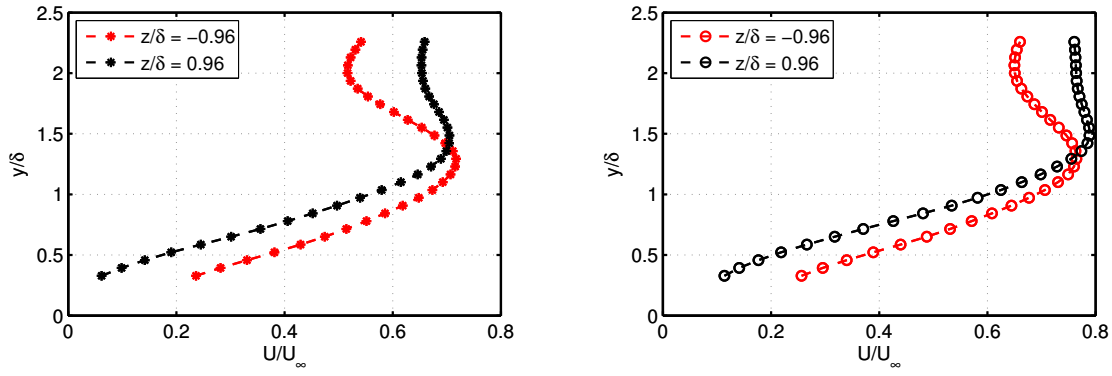

(a) $x/\delta = -3$ (b) $x/\delta = -1$

Figure 7.8: Velocity profiles for (a) $x/\delta = -3$ measured at 25% span (b) $x/\delta = -1$ measured at 50% span.

Further, according to the observations of Babinsky et al. [6] and Giepman et al. [19], the velocity contours at the edges of the micro-ramp are expected to be close to the uncontrolled interaction. Figure (7.9) illustrates the streamwise velocity contours at 50% micro-ramp span ($z/\delta = \pm 1.92$). The velocity contours at 50% micro-ramp span on either side of the centreline are almost identical except for a larger $U_{0.1}$ bubble at $z/\delta = 1.92$. From figures (7.7), (7.8)

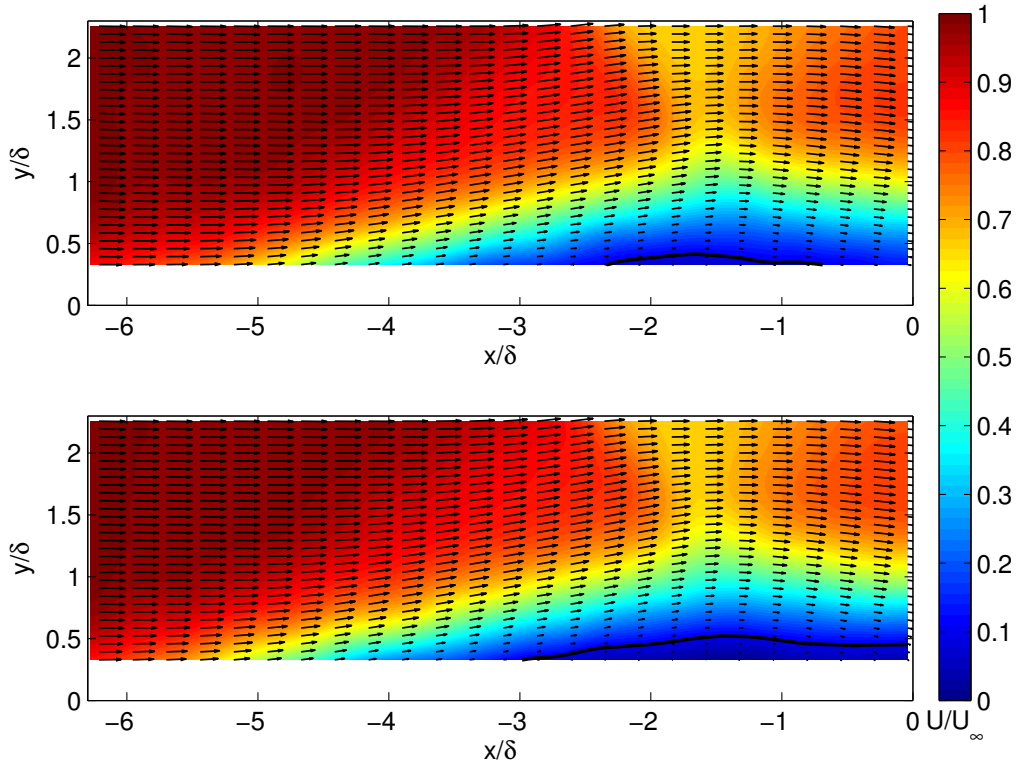

Figure 7.9: Streamwise velocity component at 50% micro-ramp span, Top: $z/\delta = -1.92$, Bottom: $z/\delta = 1.92$. Micro-ramp of h = 3 mm placed at $x_{MR} = -17.3\delta$.Black line indicates the $U_{0.1}$ bubble

and (7.9), it is seen that the present tomo-PIV measurements do not record a symmetric behaviour of the micro-ramp flow about its centreline. This discrepancy between the present experiments and the literature [41], maybe due to one of the following reasons:

- Misalignment between the micro-ramp centreline and the tunnel centreline, due to which the micro-ramp might have been at a small angle with respect to the tunnel centreline.
- Another cause of this inconsistency maybe that the volume self-calibration procedure requires further improvement.

Figure (7.10) illustrates the streamwise velocity contours at the ends of the measurement volume $z/\delta = \pm 2.3$. The velocity contours show large low velocity bubble as in the uncontrolled interaction. From this it is clear that the effect of the micro-ramp does not extend beyond its span.

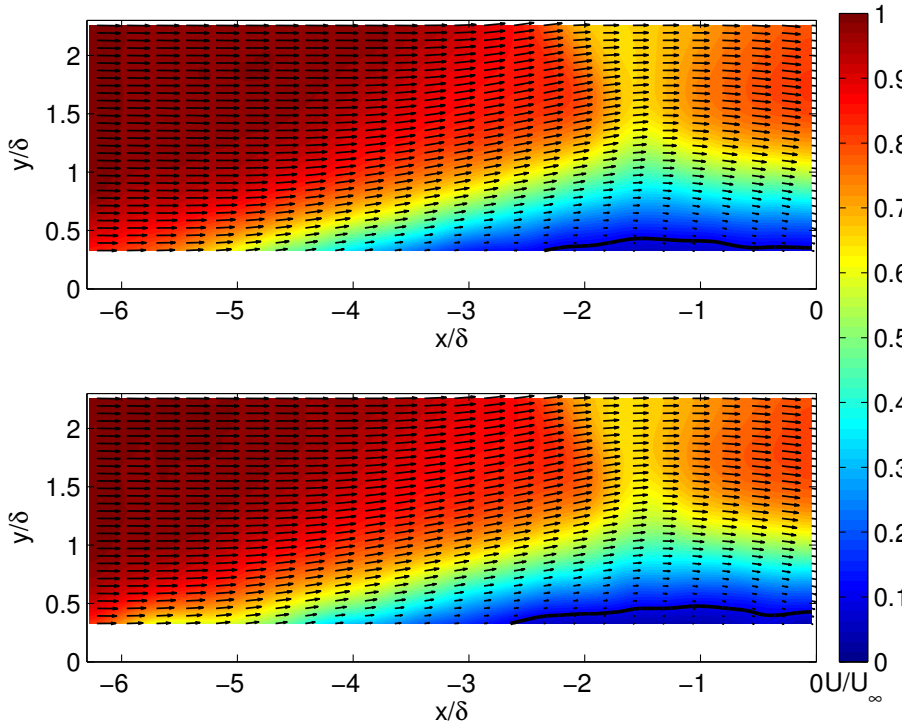

Figure 7.10: Streamwise velocity contours at ends of measurement volume $z/\delta = \pm 2.3$, micro-ramp of h = 3 mm placed at $x_{MR} = -17.3\delta$. Black line indicates the $U_{0.1}$ bubble

7.5 Micro-ramp effects: Wall parallel planes

Figure (7.11a-b) show the streamwise velocity contours of the uncontrolled and single micro-ramp controlled interactions at a wall normal location of $y/\delta = 0.3$ respectively. In both the figures, the grey line indicates the M = 1 iso-line and encloses the subsonic fluid. The $U_{0.1}$ velocity fluid is enclosed within the black line.

In the uncontrolled interaction, high velocity fluid of $U \approx 0.8U_\infty$ enters the measurement volume at $x/\delta = -6.2$. Due to the upstream influence of the incident shock wave, the boundary layer entering the measurement volume experiences deceleration. The start of this deceleration is seen at approximately $x/\delta = -6$. After this, the fluid is decelerated to subsonic velocities from $x/\delta \approx -4.75$. At the end of the measurement volume, the fluid is decelerated to $U=0.1U_\infty$. The streamwise extent of $U_{0.1}$ is found to vary from $\approx 3\delta$ to $\approx 2\delta$.

In micro-ramp controlled interaction, due to the action of the counter-rotating vortices, the boundary layer entering the interaction is fuller. Therefore, in the immediate vicinity of the micro-ramp's centreline ($z/\delta = 0.5$ to -0.5), the re-energized boundary layer undergoes deceleration further downstream (at $x/\delta \approx -5$) compared to the uncontrolled interaction. This boundary layer deceleration is postponed further downstream, even at outboard locations (such as $x/\delta = 1.5$ and -1.5), when compared to the uncontrolled interaction. Due to limited effectiveness of the micro-ramp at outboard locations, the boundary layer at the outboard

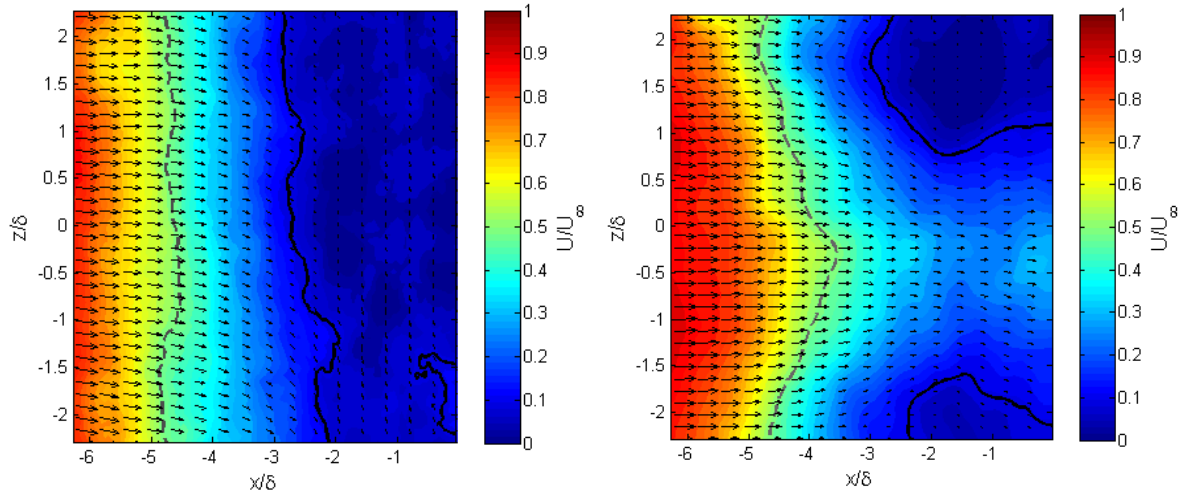

(a) Uncontrolled interaction (b) Micro-ramp controlled interaction

Figure 7.11: Streamwise velocity contours at $y/\delta = 0.3$. Black solid line encloses the $U_{0.1}$ fluid. Grey line indicates the M = 1 isoline.

locations undergoes the deceleration earlier when compared to the micro-ramp centreline. Importantly, the $U_{0.1}$ bubble is completely eliminated along the micro-ramp centreline. However, at micro-ramp outboard locations the $U_{0.1}$ bubble with a streamwise extent comparable to the uncontrolled interaction is still present.

Figures (7.12), (7.13) and (7.14) present the streamwise velocity contours at wall normal locations of $y/\delta = 0.5$, $y/\delta = 0.75$ and $y/\delta = 1$, for both the uncontrolled and single micro-ramp controlled interactions. Due to the inclination of the shock wave, the M=1 iso-line moves downstream, and the amount of sub-sonic fluid decreases with increasing distance from the wall. Importantly, at $y/\delta = 0.5$, a small $U_{0.1}$ bubble is observed in the micro-ramp controlled interaction. However, this bubble is not found in the uncontrolled interaction. From this it appears that the micro-ramp redistributes the $U_{0.1}$ fluid in the wall normal direction.

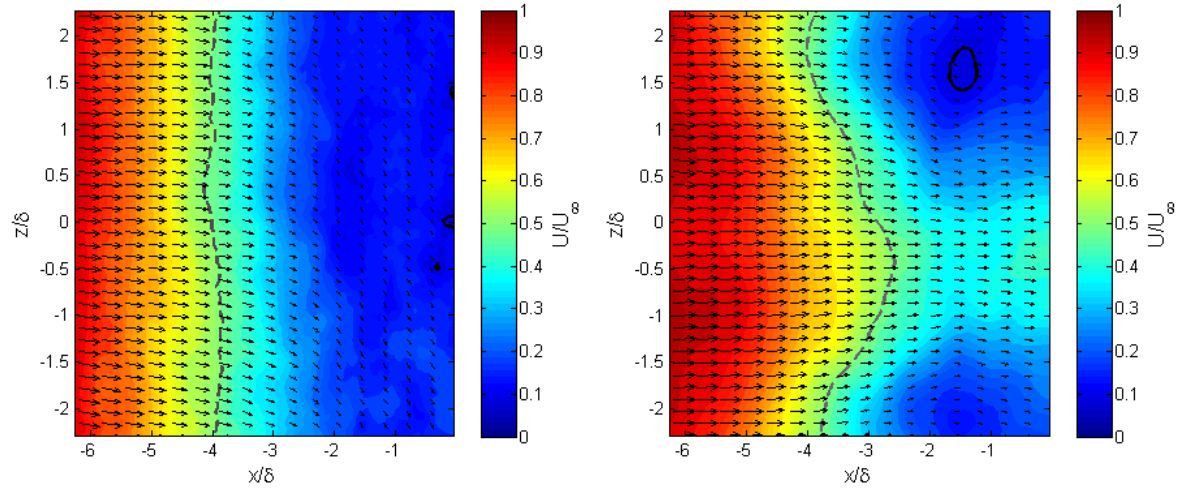

(a)Uncontrolled interaction (b) Micro-ramp controlled interaction

Figure 7.12: Streamwise velocity contours at $y/\delta = 0.5$. Black solid line encloses the $U_{0.1}$ fluid. Grey line indicates the M = 1 isoline.

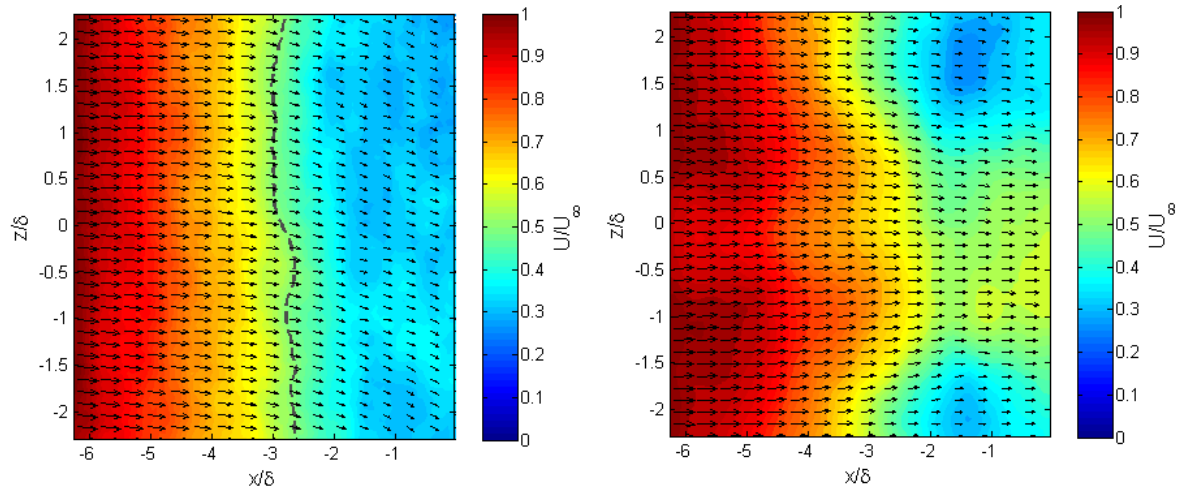

(a)Uncontrolled interaction (b) Micro-ramp controlled interaction

Figure 7.13: Streamwise velocity contours at $y/\delta = 0.75$. Grey line indicates the M = 1 isoline.

Figures (7.15) and (7.16) illustrate the streamwise velocity contours at wall normal locations outside the boundary layer: $y/\delta = 1.5$ and $y/\delta = 2.2$, for the uncontrolled and single micro-ramp controlled interactions respectively. At these wall normal locations it is seen that, the flow decelerated by the shock wave accelerates rapidly. An important feature in the micro-ramp controlled interaction is the micro-ramp wake which is seen as a relatively low velocity region between $z/\delta \approx -0.75$ and $z/\delta \approx 0.5$. At $z/\delta = 2.2$, a low velocity pocket is formed due to the interaction of the wake and shock system and can be seen around $x/\delta = -4$.

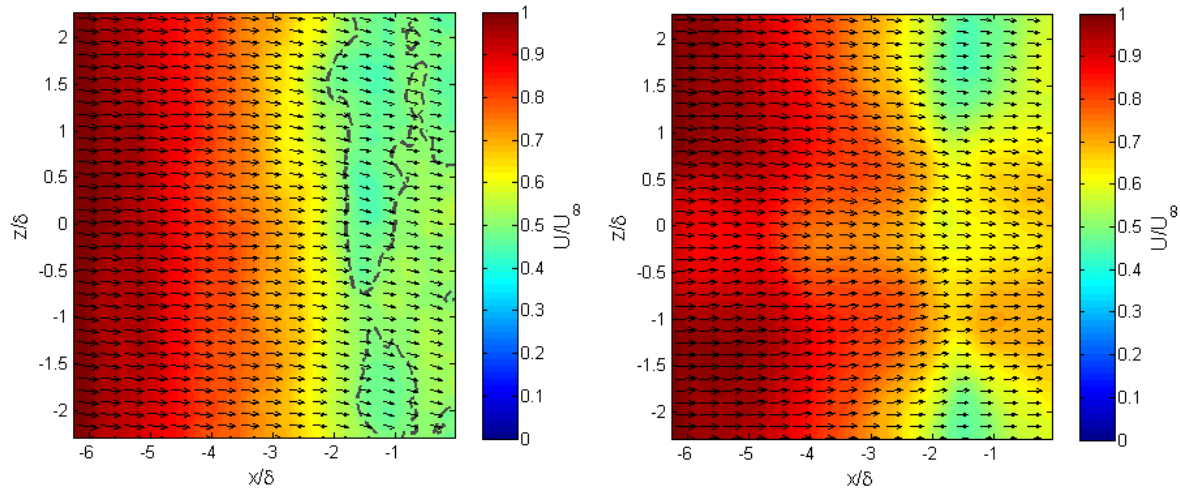

(a)Uncontrolled interaction (b) Micro-ramp controlled interaction

Figure 7.14: Streamwise velocity contours at $y/\delta = 1$. Grey line indicates the M = 1 isoline.

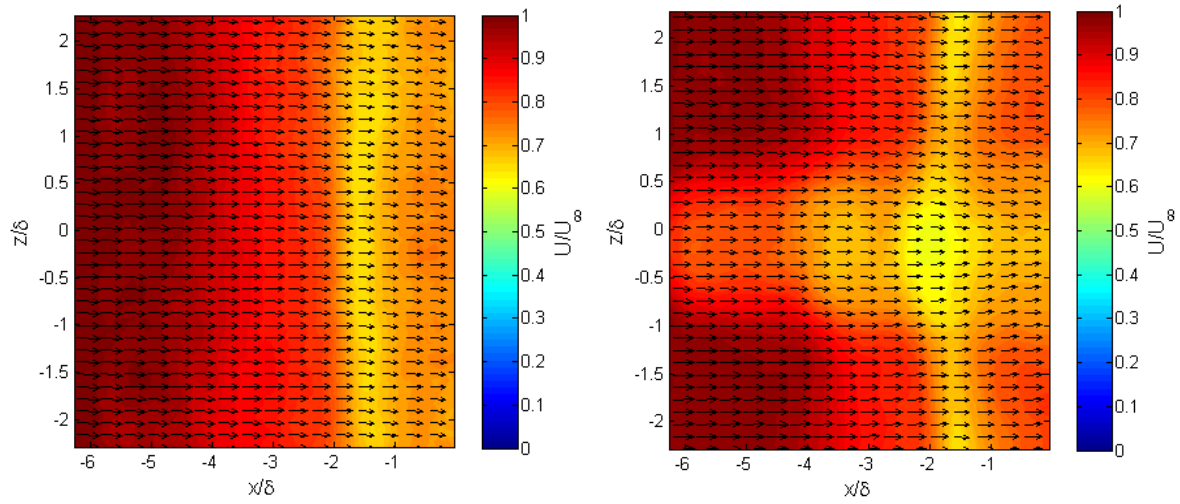

(a)Uncontrolled interaction (b) Micro-ramp controlled interaction

Figure 7.15: Streamwise velocity contours at $y/\delta = 1.5$. Grey line indicates the M = 1 isoline.

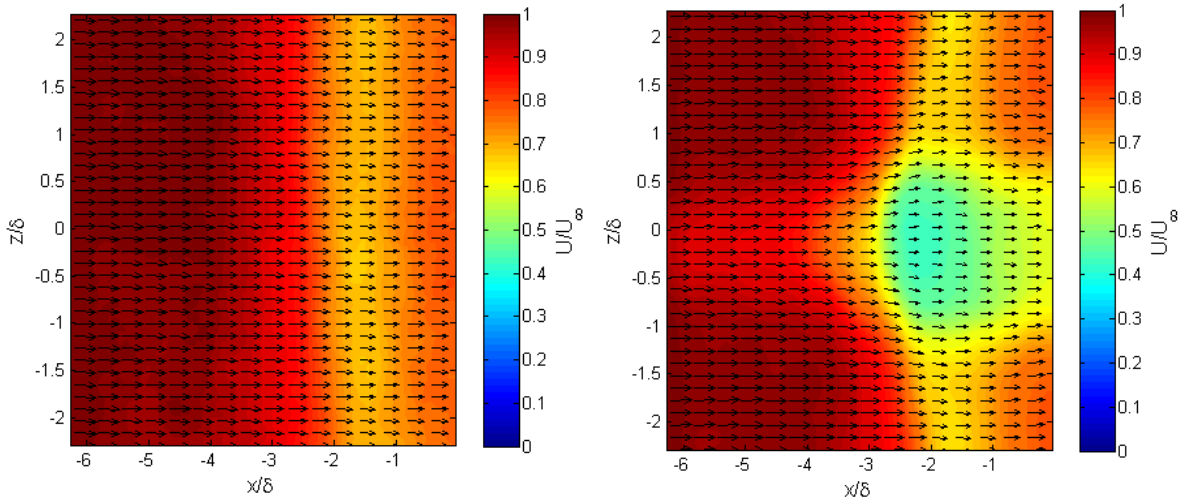

(a)Uncontrolled interaction (b) Micro-ramp controlled interaction

Figure 7.16: Streamwise velocity contours at y/δ = 2.2. Grey line indicates the M = 1 isoline.

7.6 Micro-ramp effects: Crossflow planes

Figures (7.17)- (7.20), present the streamwise and spanwise velocity contours at different streamwise stations in the measurement volume: $x/\delta = -6.2, -3.5, 2.5 and - 0.5$. Note that the limits of the colour bars in these figures are not constant.

In figure (7.17a), the micro-ramp wake is seen as a circular structure which contains the counter-rotating vortices. The wake is bound by a shear layer at its outer edge. The vortex cores are located at wall normal positions $y/\delta = 1.3$, $y/\delta = 1.7$ and separated by a spanwise distance of 0.75δ. Importantly, it is seen that the circular wake containing the counter-rotating vortex pair is not aligned with the $z/\delta = 0$ centreline. This was also indicated earlier in section (**??**) where micro-ramp flow was not found to be symmetric about the centrelines.

In figure (7.17b), a region of strong upwash (indicated by red contour) attaining velocities of $0.08U_\infty$ is seen at $z/\delta = 0.1$. Further, it is seen that the downwash regions on either side of the centreline extend over a larger area and attain approximately half the intensity of the upwash: $-0.04U_\infty$.

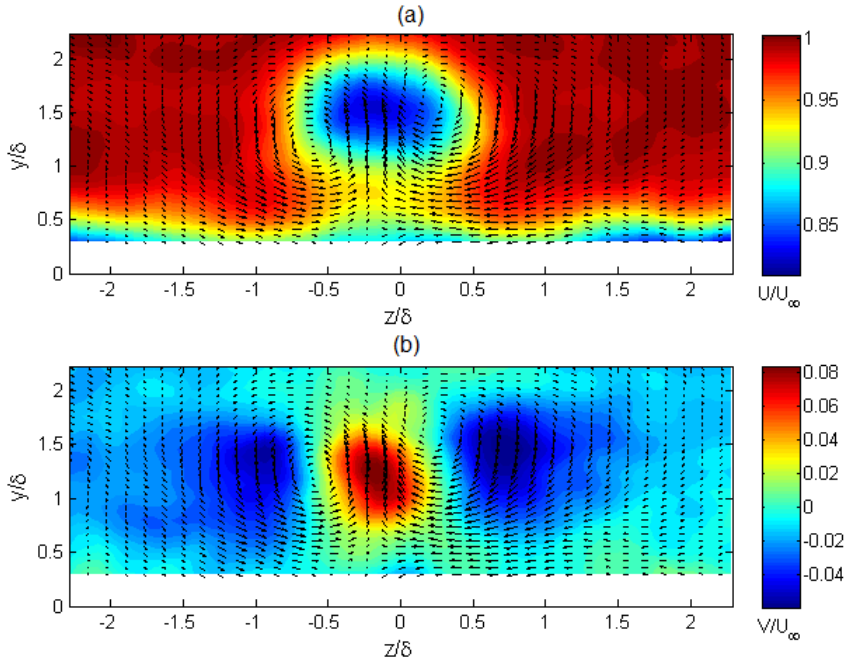

Figure 7.17: (a) Streamwise and (b) Wall-normal velocity contours at $x/\delta = -6.2$

Due to the mutual upwash of the counter-rotating vortices, they experience a net positive lift force. Therefore the vortices move away from the wall as they move downstream. This can be observed as an upward shift of the micro-ramp wake in the streamwise velocity contours of figures (7.18) and figure (7.19).

Close to the end of the volume, $x/\delta = -0.5$ it is seen that the velocity vectors are directed

towards the wall indicating a downwash. The flow at $x/\delta = 0$ has passed through the expansion fan that is caused by the reflection of the incident shock wave at the M=1 iso-line. Through the expansion fan the fluid is turned towards the wall. Hence this figure shows the fluid that is returning towards the wall.

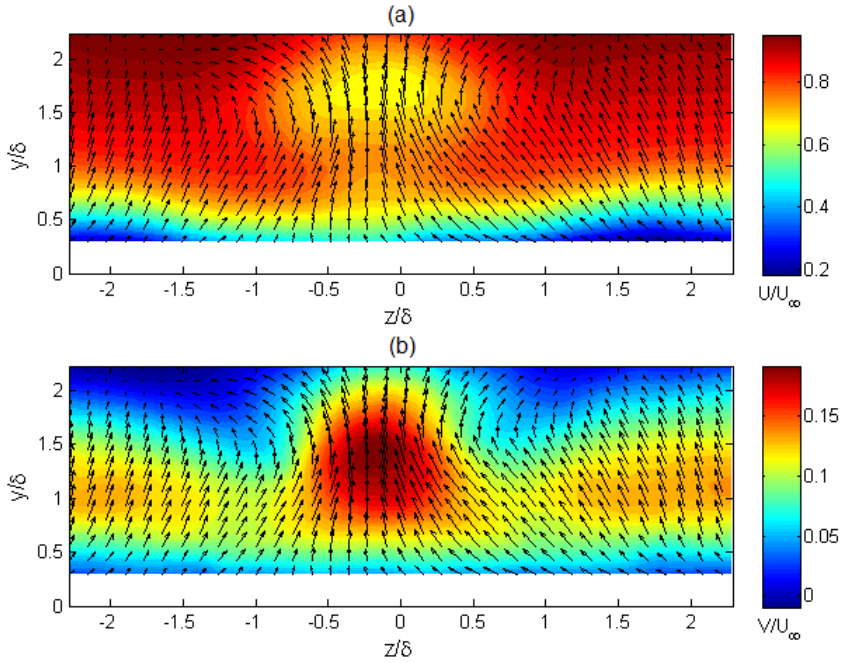

Figure 7.18: Streamwise and Wall-normal velocity contours at $x/\delta = -3.5$

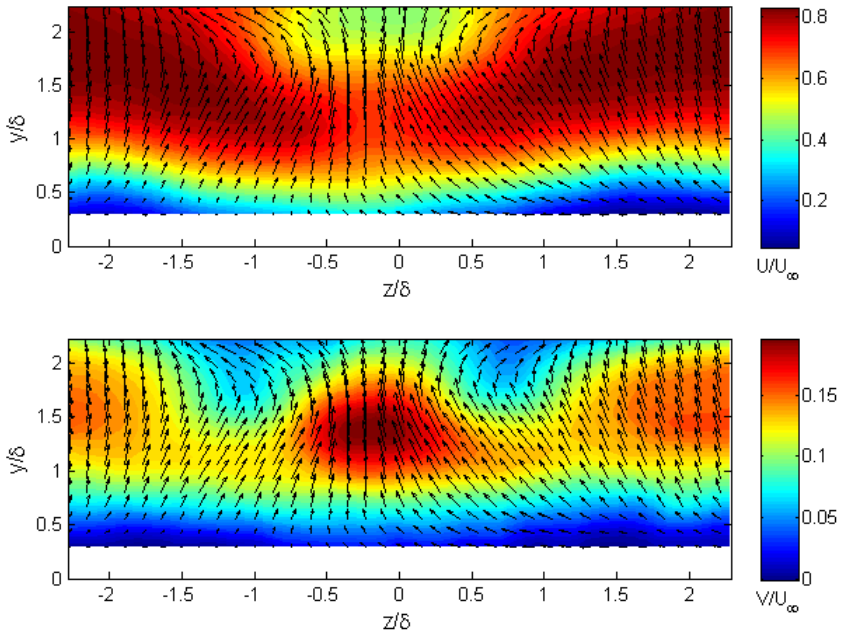

Figure 7.19: Streamwise and Wall-normal velocity contours at $x/\delta = -2.5$

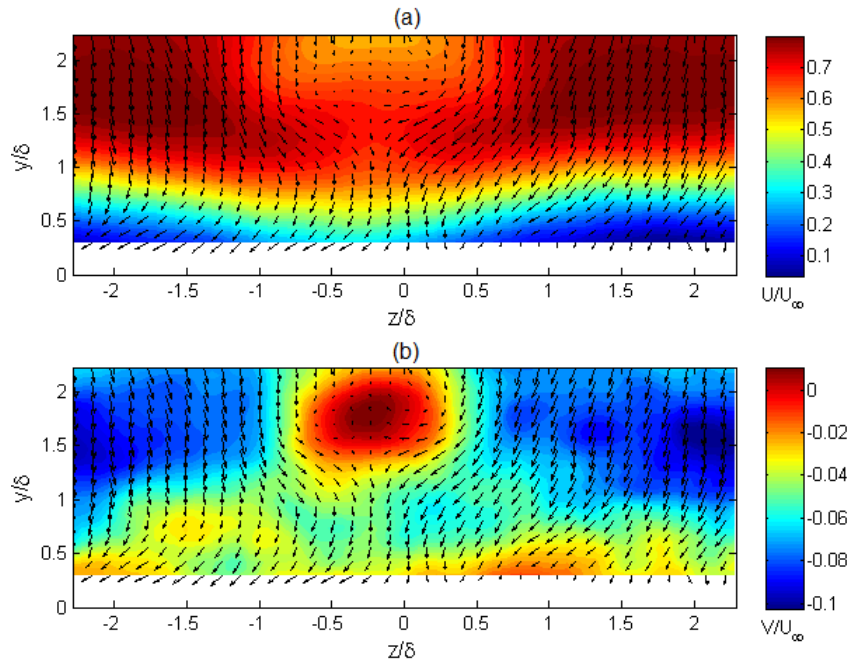

Figure 7.20: Streamwise and Wall-normal velocity contours at $x/\delta = 0$

7.7 Volumetric Flow representation

The volumetric representations of uncontrolled and micro-ramp controlled interactions are presented in figures (7.21) and (7.22) respectively. In both the figures, the green contour represents a high velocity iso-surface ($U = 0.75U_\infty$) and the pink contour presents the $U_{0.1}$ iso-surface.

In the uncontrolled interaction, the high velocity iso-surface shows a high degree of spanwise homogeneity. However, with micro-ramp control, the counter-rotating vortices greatly alter the high velocity iso-surface. In the micro-ramp controlled interaction, the primary counter rotating vortices are visualized by plotting the streamwise vorticity. The vortex pair has the same magnitude but opposite directions of rotation and hence represented by red and blue contours.

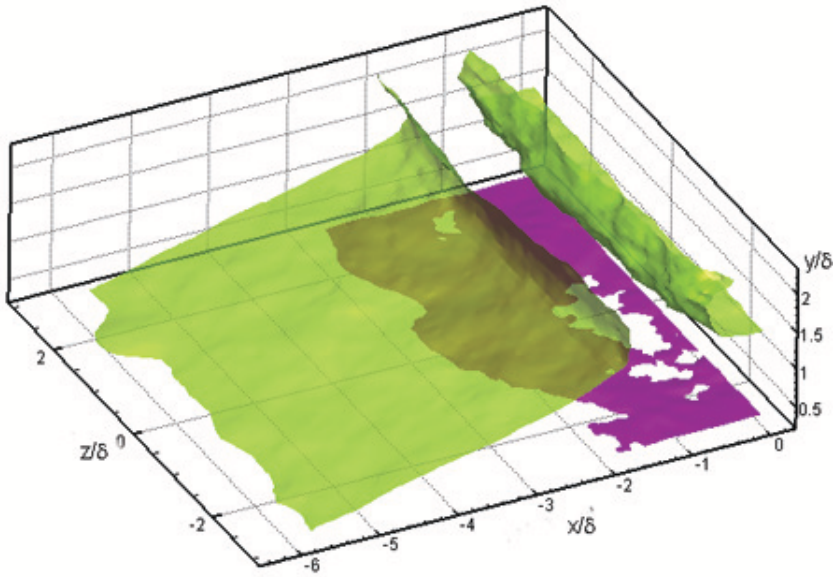

Figure 7.21: Uncontrolled interaction, Green iso-surface: $0.75U_\infty$, Purple iso-surface: $0.1U_\infty$

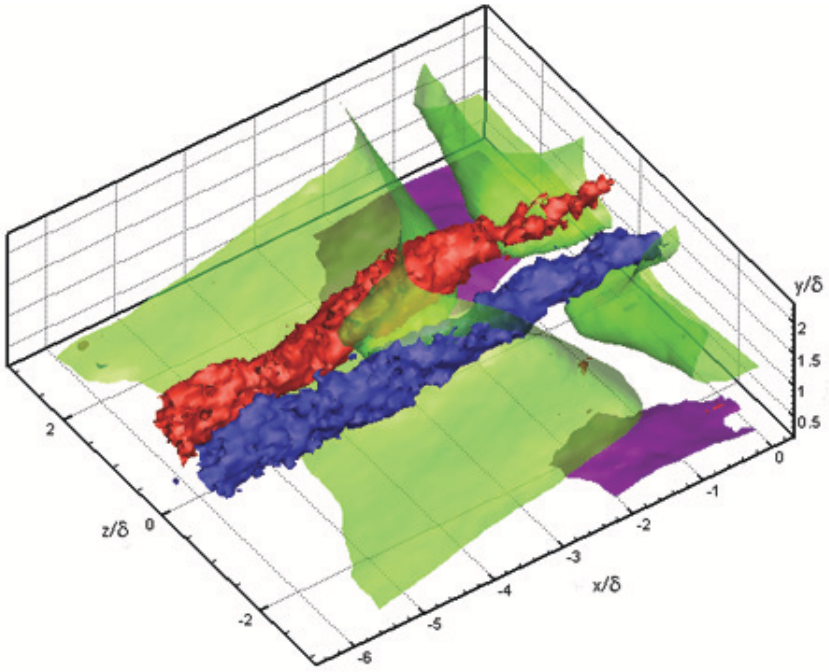

Figure 7.22: Micro-ramp controlled interaction, Green iso-surface: $0.75U_\infty$, Purple iso-surface: $0.1U_\infty$, Red and blue contours: counter-rotating vortices

Chapter 8

Statistical Analysis

8.1 Introduction

In Chapter (6) and section (6.3) it was noted from the surface oil flow patterns, that the streamwise extent of the separation bubble increases at outboard locations by using micro-ramps. Further, in Chapter (7) in section (7.5) it was noted that the micro-ramp appears to redistribute the flow in the wall normal direction . In particular it was found that low velocity regions of $U_{0.1}$ have a greater wall normal height of in micro-ramp controlled interaction. Therefore it is important to determine whether a micro-ramp reduces the total amount of the separated flow or redistributes the separated fluid.

To this end, first the local probability of separation P_{sep} as defined by Giepman et al. [19] is determined from the instantaneous snapshots. The separation probability is then integrated in the domain to obtain the area of separation A_{sep} (at different spanwise and wall-parallel planes) and the total volume of separation V_{sep}. The effect of the micro-ramp on the separation probability in the interaction region is discussed in section (8.2). This is followed by a discussion on the area of separation and the total volume of separation in section 8.3. Further, section (8.4) explores whether a correlation exists between the size of the separation bubble in the spanwise direction.

8.2 Probability of separation

Probability of separation P_{sep} is defined as the probability that a certain point (x,y,z) in the measurement volume shows flow reversal i.e $U < 0$. [19]. At the micro-ramp symmetry plane Giepman et al. [19] found that P_{sep} in the interaction region reduces by application of micro-ramp control.

8.2.1 Spanwise planes

Figure (8.1a) and figure (8.1b) illustrate the local separation probability at $z/\delta = 0$ for the uncontrolled and micro-ramp controlled interactions respectively. It is noted that the entire separation bubble is not captured in the measurement volume. It can be seen that the streamwise extent of the separation bubble captured is $\approx 5\delta$ for the uncontrolled interaction. With a h = 3 mm micro-ramp placed 17.3δ upstream of the interaction, this has been reduced to $\approx 4\delta$.

In the uncontrolled interaction, the highest separation probability of about 45% is observed at (x,y)= $(-1.7\delta, 0.3\delta)$. With micro-ramp control, this peak value is reduced to about 11% at the same streamwise location. Similar reductions in P_{sep} have been recorded by Giepman et al. [19]. With h = 4 mm micro-ramp, Giepman et al. [19] noted that the separation probability close to the wall ($y/\delta \approx 0.1$) is reduced from 75% in the uncontrolled interaction to 41%.

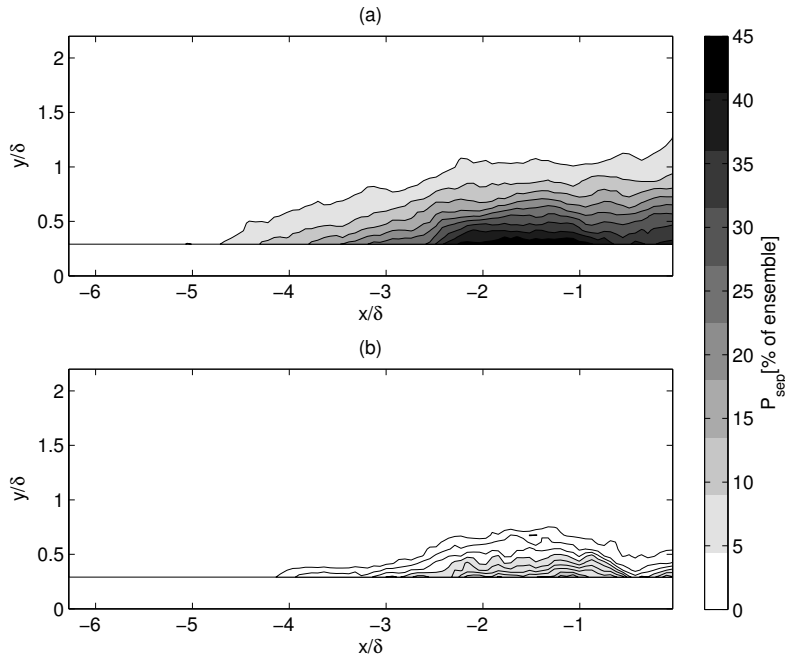

Figure 8.1: Separation Probability P_{sep} at $z/\delta = 0$ (a) uncontrolled interaction (b) Interaction controlled by a micro-ramp h = 3 mm placed at $x_{MR} = -17.3\delta$

The reduction in the separation probability is also observed at outboard locations. Figure (8.2) shows the P_{sep} for the uncontrolled interaction and controlled interaction at 25% of micro-ramp span or $z/\delta = 0.96$. By using micro-ramp control, the maximum separation probability has reduced from 47% to 35%. Compared to the symmetry plane of the micro-ramp $z/\delta = 0$, the reduction in P_{sep} caused by the micro-ramp at $z/\delta = 0.96$ is lesser. This behaviour is expected since it is known from the average velocity fields that the effectiveness of the micro-ramp in elimination of separation reduces while moving outboard.

Further, the local separation probability P_{sep} for $z/\delta = -0.96$ is shown in figure (8.3). Micro-ramp reduces the maximum separation probability from 45% to 10%. From figures () and (), it is observed that with micro-ramp control, the reduction in separation probability at $z/\delta = 0.96$ and $z/\delta = -0.96$ is not identical. This maybe due to a misalignment between the tunnel and the micro-ramp centrelines, or due to the volume-self calibration procedure as discussed in Chapter (7) and section (7.4). While moving further outboard, at 50% micro-

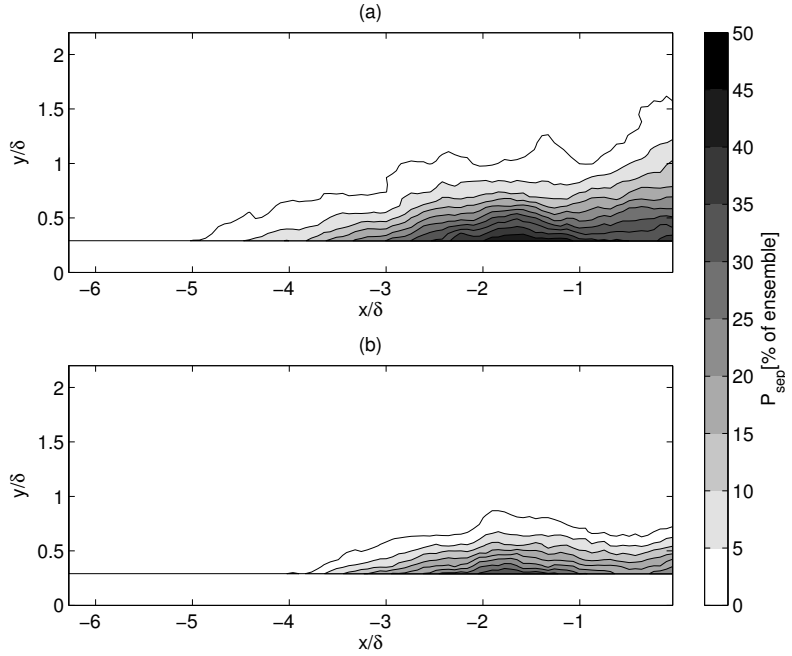

Figure 8.2: Separation probability P_{sep} at $z/\delta = 0.96$ (25% span) (a) uncontrolled interaction (b) Interaction controlled by a micro-ramp h = 3 mm placed at $x_{MR} = -17.3\delta$

ramp span $z/\delta = \pm 1.92$, the effectiveness of micro-ramp in separation reduction further decreases. At $z/\delta = \pm 1.92$ the maximum separation probability reduces from 41% to 36%. This can be observed in figures (8.4) and (8.5).

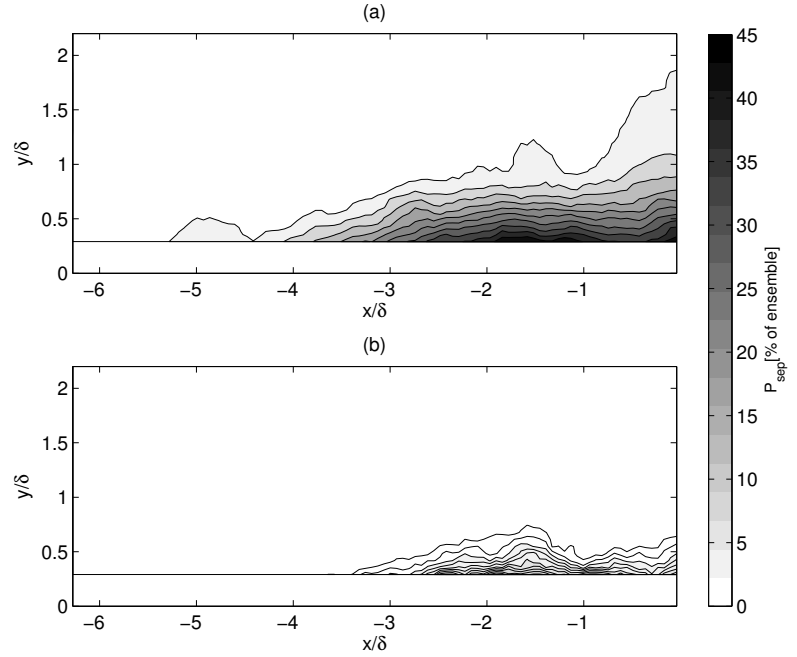

Figure 8.3: Separation probability P_{sep} $z/\delta = -0.96$ (25% span) (a) uncontrolled interaction (b) Interaction controlled by a micro-ramp h = 3 mm placed at $x_{MR} = -17.3\delta$

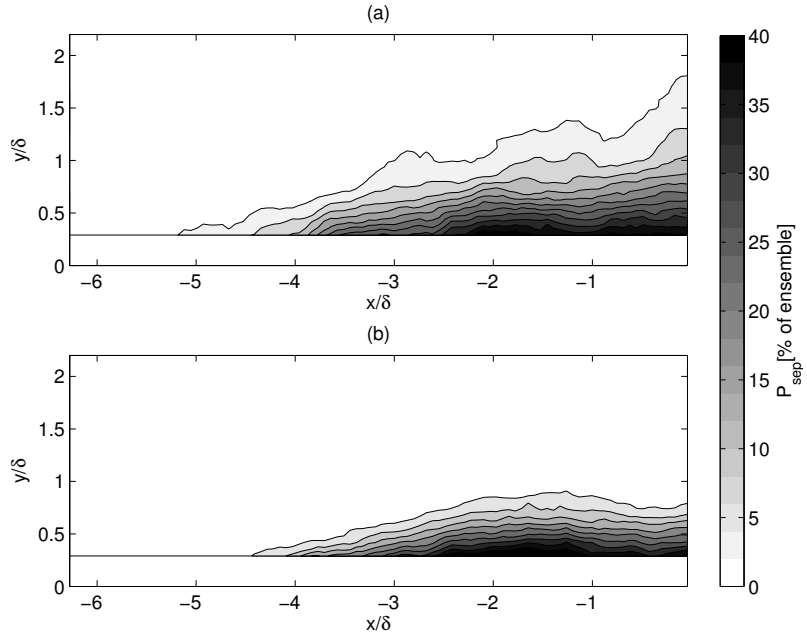

Figure 8.4: Separation probability P_{sep} $z/\delta = 1.91$ (50% span) (a)uncontrolled interaction (b) Interaction controlled by a micro-ramp h = 3 mm placed at $x_{MR} = -17.3\delta$

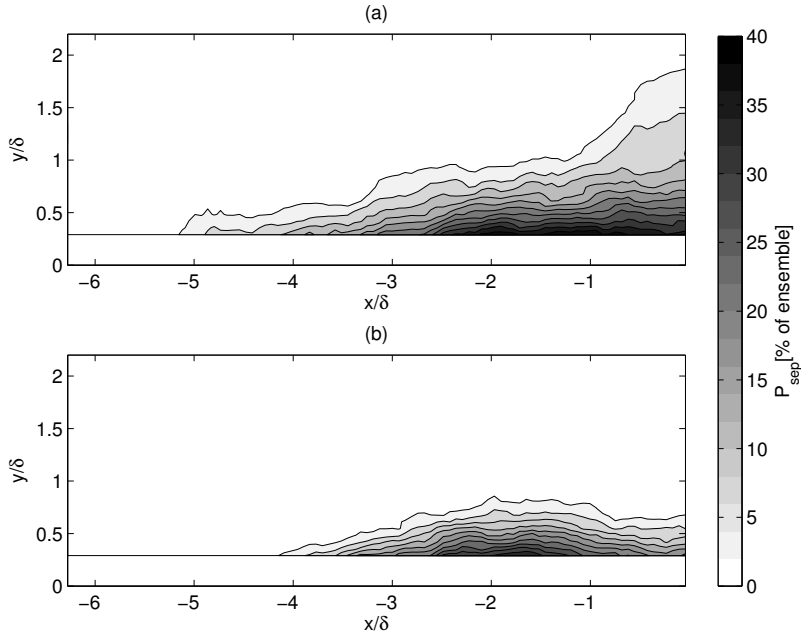

Figure 8.5: Separation probability P_{sep} $z/\delta = -1.91$ (50% span) (a) uncontrolled interaction (b) Interaction controlled by a micro-ramp h = 3 mm placed at $x_{MR} = -17.3\delta$

8.2.2 Wall-parallel planes

The separation behaviour of the interaction is further investigated by determining the separation probability at different wall parallel planes within the boundary layer. Figure (8.6) - (8.8) show P_{sep} for the uncontrolled interaction and single micro-ramp controlled interaction at wall parallel planes: $y/\delta = 0.3, 0.5$ and 0.75. Note varying colourbar limits in these figures.

At $y/\delta = 0.3$ the micro-ramp controlled interaction exhibits a significant reduction in P_{sep}. From $x/\delta = -5.5$ to $x/\delta \approx -4$ the separation probability is reduced to zero when micro-ramp control is used. Importantly, the largest reductions in the separation probability are observed close to the micro-ramp centreline. The separation probability is reduced from $\approx 45\%$ to $\approx 4\%$. This means that these locations show flow reversal only in 4% of the ensemble.

At outboard locations the effectiveness of the micro-ramp reduce, hence the reduction in P_{sep} is less when compared to the centreline. However, when compared to the uncontrolled interaction, micro-ramp application still proves to be advantageous in the reduction of P_{sep}. The largest separation probability of $P_{sep} \approx 55\%$ at (x,y) = $(-1.52\delta, 1.6\delta)$ is reduced to $\approx 44\%$ with micro-ramp control.

With increasing distance from the wall, the maximum P_{sep} decreases. At $y/\delta = 0.5$, the uncontrolled interaction shows a maximum $P_{sep} = 35\%$. However, with micro-ramp control, this maximum value is decreased to $\approx 31\%$ at outboard locations. At wall normal locations of $y/\delta = 0.75$ similar decrease in separation probability is recorded. It is seen that the micro-ramp decreases the maximum separation probability from 21% to 14%.

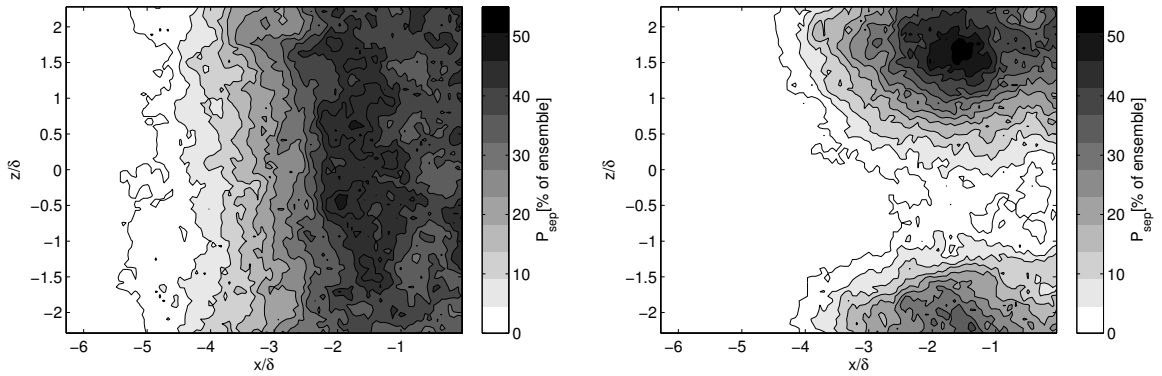

(a) Uncontrolled interaction (b) Micro-ramp controlled interaction

Figure 8.6: Separation Probability P_{sep} at $y/\delta = 0.3$

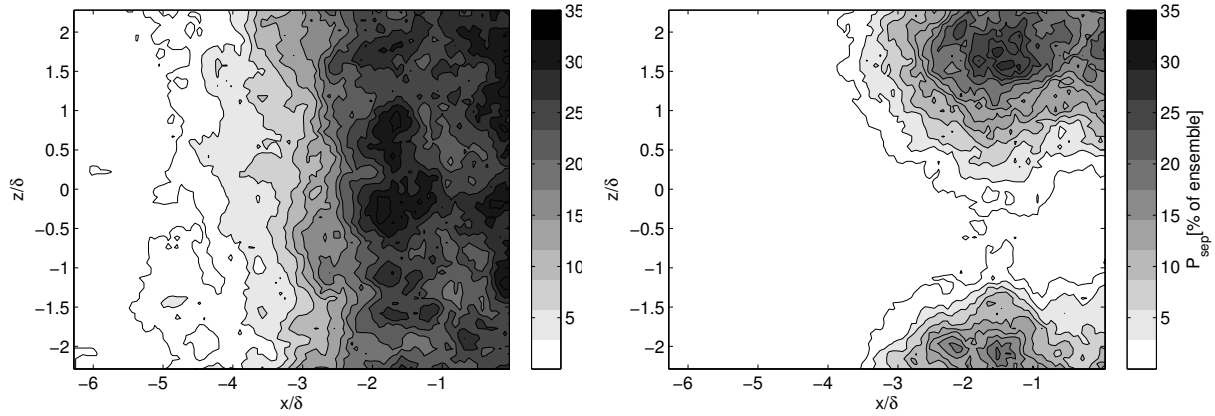

(a) Uncontrolled interaction (b) Micro-ramp controlled interaction

Figure 8.7: Separation Probability P_{sep} at $y/\delta = 0.5$

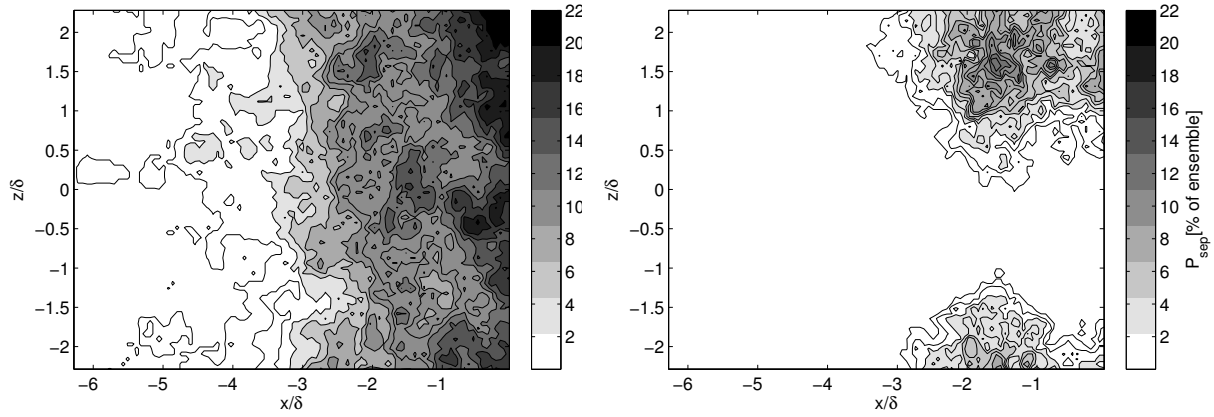

(a) Uncontrolled interaction (b) Micro-ramp controlled interaction

Figure 8.8: Separation Probability P_{sep} at $y/\delta = 0.75$

8.3 Total volume of separated flow

As discussed in the beginning of this chapter, the probability of separation P_{sep} can be integrated in the domain to obtain the average area of separation A_{sep} and volume of separated fluid V_{sep} in the interaction. The average separated area A_{sep} is defined as:

$$A_{sep} = \frac{A_{sep,controlled}}{A_{sep,uncontrolled}} \tag{8.1}$$

Hence A_{sep} is obtained after normalizing the average separated area in the controlled interaction by the average separated area in the uncontrolled interaction.

Figure (8.9) shows a plot of A_{sep} at different spanwise planes. From $z/\delta = -1$ to $z/\delta = 0$, the average separated area is ≈ 0.05 $A_{sep,\ uncontrolled}$. The largest reductions are observed at $z/\delta = -0.4$ where micro-ramp control reduces the average separated area to $0.04A_{sep,\ uncontrolled}$. At outboard locations, the effectiveness of the micro-ramps reduces. Importantly, it can be observed that the reduction in the separated area is not identical on either sides of the micro-ramp centreline.

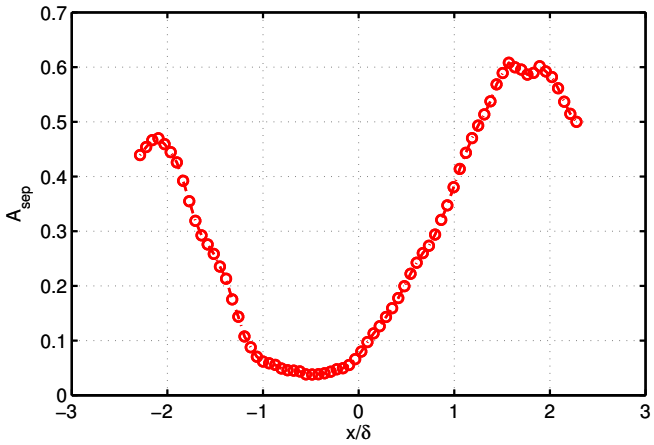

Figure 8.9: A_{sep} for different spanwise planes, for a h = 3 mm micro-ramp placed at $x_{MR} = -17.3\delta$.

While moving away from the wall, the probability of separation reduces as observed in the previous section. Hence, the area of separated flow also reduces with increase in the wall normal distance. In the uncontrolled interaction, no separated flow is found for $y/\delta > 1.13$ due to which $A_{sep} = 0$ for $y/\delta > 1.13$ in figure (8.10).

From the probability of separation in the entire measurement volume, the the total volume of separated flow V_{sep} is determined. By using micro-ramp control, the total volume of separated flow is reduced to 31% of the uncontrolled interaction for the micro-ramp of height h= 3 mm placed 17.3δ upstream of the inviscid shock impingement location. This confirms that micro-ramps have a beneficial effect in reducing the total volume of separated flow.

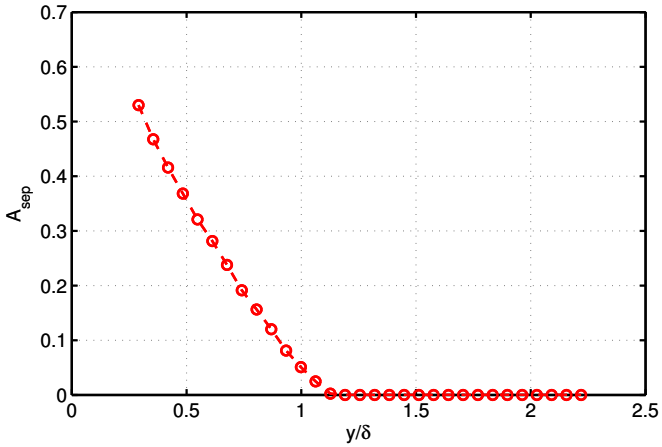

Figure 8.10: Average separated area A_{sep} for different wall-parallel planes, for a h = 3 mm micro-ramp placed at $x_{MR} = -17.3\delta$.

8.4 Spanwise correlation of separation bubble size

The separation bubble size is calculated as the streamwise extent of the region which shows flow reversal i.e $U < 0$. Figure (8.11) shows the correlation between bubble sizes at different locations along the span, i.e between $z/\delta = 1$ and -1, $z/\delta = 1.5$ and $z/\delta = -1.5$ and so on. Such locations on either side of the micro-ramp centreline will be referred to as 'spanwise location pairs' from here on. The correlation coefficients between such spanwise location pairs, at wall normal planes: $y/\delta = 0.3, 0.5, 0.75$ and 1 are presented in this figure. An additional x-axis is included at the top of the figure to show the scaling with respect to the micro-ramp height.

The correlation coefficients between the separation bubble sizes close to the micro-ramp centreline remain positive at all wall normal locations. At $z/\delta = 0$, the correlation coefficient r = 1, since it is an autocorrelation of the separation bubble size. At the ends of the measurement volume $z/\delta = \pm 2.3$, the correlation coefficient reduces to zero at all wall normal positions, except for $y/\delta = 1$ where a weak positive correlation coefficient r= 0.13 is observed.

At $y/\delta = 0.3$, the correlation coefficient r reduces to zero for the spanwise pair $z/\delta = \pm 0.5$. When further outboard stations are considered, a negative correlation is observed. The strongest negative correlation coefficient of r = -0.29 is observed at $z/\delta = \pm 1.84$. This means that, when the separation bubble size increases at $x/\delta = -1.84$, its size decreases at $x/\delta = 1.84$ and vice versa.

An example of such negative correlation between separation bubble size is shown in figure (8.12). Figure (8.12) shows an instantaneous snapshot of streamwise velocity contours at wall-normal plane $y/\delta = 0.3$. For $z/\delta < 0$, a large separation bubble can be observed. However, for $x/\delta > 0$ relatively small regions of separated flow are observed.

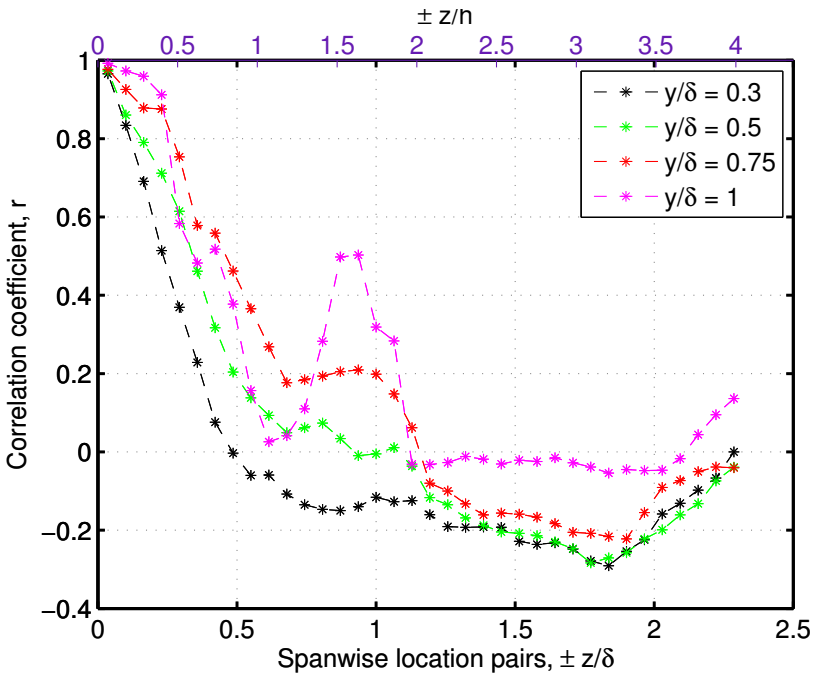

Figure 8.11: Correlation co-efficient between bubble size at different spanwise location pairs.

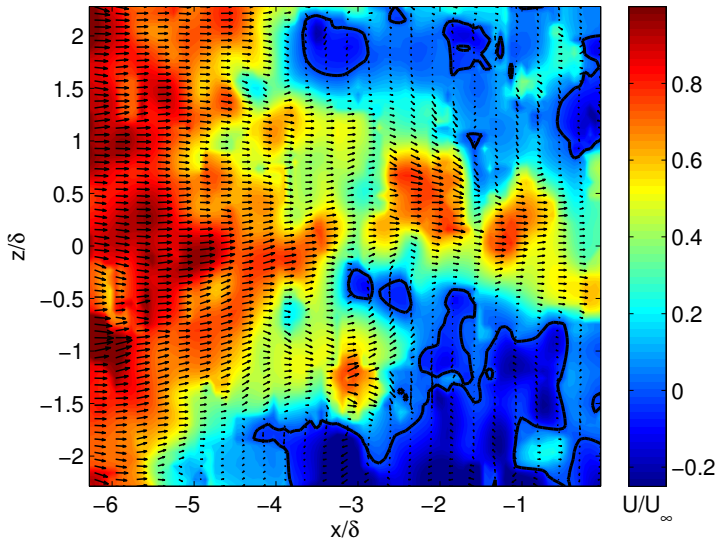

Figure 8.12: Instantaneous snapshot showing U/U_∞ contours for h = 3 mm micro-ramp at $y/\delta = 0.3$.

Further, at $y/\delta = 0.5$ and $y/\delta = 0.75$, the strongest negative correlation coefficients of r= -0.29 and r= -0.22 are recorded at $z/\delta = \pm 1.75$ and $z/\delta = \pm 1.9$. The correlation coefficient is strongest close to the wall i.e at $y/\delta = 0.3$. Further, at $y/\delta = 1$, the correlation coefficient reduces to zero at $z/\delta = 0.6$, after which a sharp increase in the correlation coefficient is observed at $z/\delta = \pm 0.9$. Following this, the correlation coefficient reduces to zero and remains

close to zero till the ends of the volume.

Further, correlation coefficients between streamwise velocity were determined for different spanwise location pairs in the entire domain. Figures (8.13a-c) show the correlation coefficient results in the entire domain for $y/\delta = 0.3$, 0.5 and 0.75 respectively. At $y/\delta = 0.3, 0.5$ a region of positive correlation coefficient is seen from $x/\delta = -6.2$ to ≈ 4. Further downstream from this region, a negative correlation coefficient is recorded everywhere in the domain. At the centreline i.e $z/\delta = 0$ the correlation coefficient is 1. With increasing wall-normal distance, the region at the start of the measurement domain showing a positive correlation coefficient reduces.

From the instantaneous snapshot of the streamwise velocity in figure (8.12), it seems that the instantaneous meandering motion of the micro-ramp wake containing the counter-rotating vortices leads to the observed negative correlation coefficient. When the micro-ramp wake moves to the right of the centreline, the separation bubble becomes larger on the left and vice versa.

However, it is important to recall that Sun et al. [42] observed that the counter-rotating vortex pair is brought closer to one another under the head of a K-H vortex as discussed earlier in chapter (2), section (2.4.2). For this kind of vortex motion, a positive correlation co-efficient would be expected. This means that, when the primary vortices come close to each other under the K-H vortex, their effect at outboard locations is lower due to which separated flow increases at outboard locations on either side the micro-ramp centreline. Similarly, when the vortices are not under the K-H vortex, they are further apart which increases their efficiency at outboard locations, and separated flow is reduced on either side of the centreline. However, the study performed by Sun et al. [42] involved only the investigation of micro-ramp flow and did not involve a shock-boundary layer interaction unlike in the present study.

Therefore, it is possible that the introduction of the shock system and the unsteadiness of the reflected shock wave changes the instantaneous movement pattern of the primary counter-rotating vortices (as described by Sun et al. [42]) and/or the K-H vortices found in the shear layer.

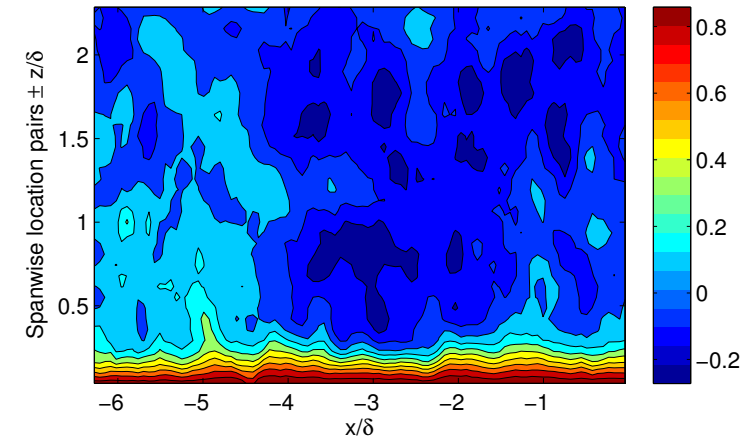

(a) $y/\delta = 0.3$

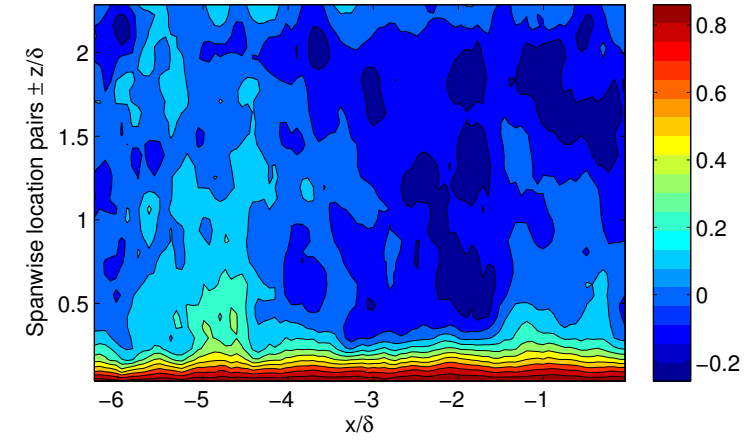

(a) $y/\delta = 0.5$

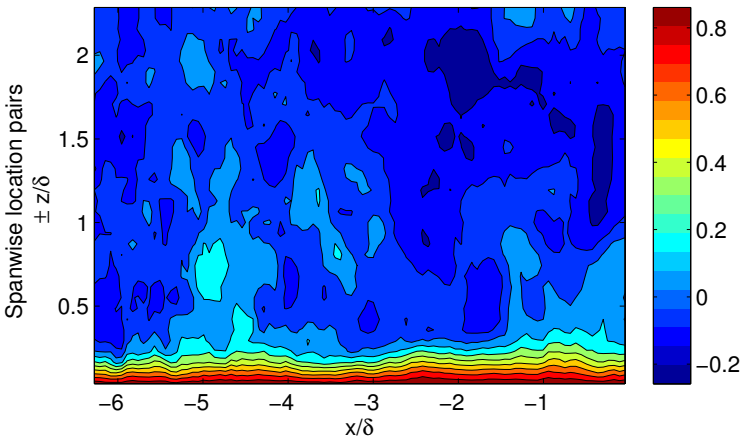

(a) $y/\delta = 0.75$

Figure 8.13: Correlation between U/U_∞ at different spanwise location pairs

Chapter 9

Conclusions and scope for future work

9.1 Introduction

This research project set out to explore the separation behaviour of a micro-amp controlled interaction by first obtaining the 3D velocity fields in the interaction. In particular, the study sought to answer the following questions about the separation behaviour of the micro-ramp controlled interaction:

- Does the total volume of separated flow decrease in a micro-ramp controlled interaction compared to the uncontrolled interaction?
- Does the separation probability decrease in micro-ramp controlled interaction compared to the uncontrolled interaction?
- Is the size of the separation bubble at one spanwise location coupled to its size at another spanwise location?

The answers to these questions and additional conclusions from the results in Chapter (5) to Chapter (8) are synthesized in section (9.2). Section (9.3) presents the additional work that could extend the knowledge of micro-ramp control of SWBLI.

9.2 Conclusions

- Chapter (5), section (5.2) showed that the horseshoe vortex emanating from the leading edge of the micro-ramp may not be a physical flow feature (or maybe a very weak structure even for large ramp angles). Such flow features which could be artefacts of the visualization technique itself, highlight the importance of proper interpretation of

surface oil flow patterns. It also shows that simple and inexpensive techniques can reveal key information about the flow features.

- The surface oil flow patterns for the uncontrolled and micro-ramp controlled interaction were discussed in Chapter (6) and section (6.3). With micro-ramp control, attached flow is observed in the interaction region along the micro-ramp centreline. Importantly, it is noted that the streamwise extent of the separation bubble increases due to micro-ramp application at outboard locations: $z/\delta > 5$ and $z/\delta < -5$. This indicates a spanwise redistribution of separated flow by the micro-ramp. However, it appears that the micro-ramp has a net positive effect on reducing flow separation.

- The spatial distribution of the mean streamwise velocity component was presented in Chapter (7). From the velocity distribution at wall-parallel planes presented in section (7.5), it is noted that the $U_{0.1}$ shows a greater wall normal extent in the micro-ramp controlled interaction when compared to the uncontrolled interaction. This indicates that the separated flow regions also extend to greater wall normal height compared to the uncontrolled interaction.

- In Chapter (8), section (8.2) it was found that the separation probability P_{sep} is reduced in the micro-ramp controlled interaction compared to the uncontrolled interaction. At the centreline, the maximum probability of separation $P_{sep} = 45\%$ in the uncontrolled interaction is reduced to 11% by employing micro-ramp control. This reduction in P_{sep} is also observed at outboard locations. However, as expected, the micro-ramp is less effective in reducing the separation at outboard locations and the largest reductions occur at the micro-ramp centreline.

- The effect of the micro-ramp on the area of separation A_{sep} was quantified in Chapter (8) and section (8.3). A_{sep} is reduced to 5% of the uncontrolled interaction along the micro-ramp symmetry plane. At outboard locations, the A_{sep} is reduced to 60% of the uncontrolled interaction. This behaviour is expected since the effectiveness of micro-ramps in reducing separation is decreased at outboard locations.

- From Chapter(8) and section (8.3), it is confirmed from the tomographic-PIV results that a micro-ramp successfully reduces the total volume of separated flow V_{sep}. For the present experimental conditions, micro-ramp height and placement of the micro-ramps, the total volume of separated flow is reduced to 30% compared to the uncontrolled interaction.

- In Chapter (8), section (8.4), a moderate negative correlation coefficient was found to exist between the separation bubble sizes for a given spanwise location pair. At $y/\delta = 0.3$, a correlation coefficient r = -0.29 is observed at $z/\delta = \pm 1.84$. This indicates that when the separation bubble becomes bigger at $z/\delta = -1.84$, it becomes smaller at $z/\delta = 1.84$ and vice versa.

9.3 Scope for future work

- During the experimental campaign of the present study, tomographic-PIV experiments were also performed for single-row and double-row micro-ramp arrays. Therefore, one immediate possible work would comprise the extension of the present study to these micro-ramp array configurations.
- In Chapter (8), section (8.4) it is observed that the separation bubble size at one spanwise location is coupled to its size at another spanwise location. Such spanwise coupling becomes important while placing micro-ramps beside one another as micro-ramp arrays.

  According to Sun [41], wakes of micro-ramps do not interact with one another till 30 micro-ramp heights downstream of the micro-ramp when placed in the single-row array configuration as shown in figure (9.1). However, in case of double-row staggered micro-ramp arrays, the micro-ramp wake interaction becomes a possibility. Due to this the spanwise coupling between the separation bubble size becomes an important factor in case of staggered arrays.

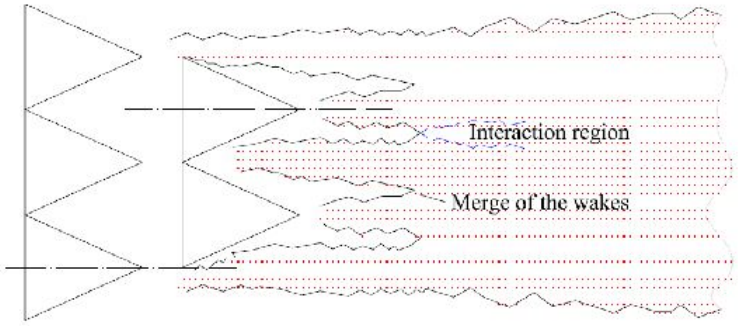

Figure 9.1: Interaction of micro-ramp wakes in a double-row staggered micro-ramp array [41]

Since micro-ramp arrays are the way forward for practical applications, further investigation regarding the implication of the spanwise coupling, on reduction of separated flow and unsteadiness of the interaction becomes an important and potential research opportunity.

Bibliography

[1] http://user.engineering.uiowa.edu/~fluids/.

[2] http://aviation.stackexchange.com/questions/13096/what-are-the-merits-of-an-inlet-cone-spike-centerbody-vs-a-2d-inlet.

[3] http://www.sr-71.org/blackbird/j-58/j58image2.jpg.

[4] B. H. Anderson, J. Tinapple, and L. Surber. Optimal control of shock wave turbulent boundary layer interactions using micro-array actuation. *AIAA Journal*, 3197, 2006.

[5] P. R. Ashill, J. L. Fulker, and K. C. Hackett. Studies of flows induced by sub boundary layer vortex generators (sbvgs). *AIAA paper*, 968:2002, 2002.

[6] H. Babinsky, Y. Li, and C. W. Pitt Ford. Microramp control of supersonic oblique shock-wave/boundary-layer interactions. *AIAA journal*, 47(3):668–675, 2009.

[7] S. J. Beresh, N. T. Clemens, and D. S. Dolling. Relationship between upstream turbulent boundary-layer velocity fluctuations and separation shock unsteadiness. *AIAA journal*, 40(12):2412–2422, 2002.

[8] P. L. Blinde, R. A. Humble, B. W. Van Oudheusden, and F. Scarano. Effects of micro-ramps on a shock wave/turbulent boundary layer interaction. *Shock Waves*, 19(6):507–520, 2009.

[9] D. R. Chapman, D. M. Kuehn, and H. K. Larson. Investigation of separated flows in supersonic and subsonic streams with emphasis on the effect of transition. 1958.

[10] J. Délery and R. Bur. The physics of shock wave/boundary layer interaction control: last lessons learned. *Office national d etudes et de recherches aerospatiales onera-publications-tp*, (181), 2000.

[11] D. S. Dolling. Fifty years of shock-wave/boundary-layer interaction research: what next? *AIAA journal*, 39(8):1517–1531, 2001.

[12] P. Dupont, S. Piponniau, A. Sidorenko, and J. F. Debiève. Investigation by particle image velocimetry measurements of oblique shock reflection with separation. *AIAA journal*, 46 (6):1365–1370, 2008.

[13] J. P. Dussauge, P. Dupont, and J. F. Debiève. Unsteadiness in shock wave boundary layer interactions with separation. *Aerospace Science and Technology*, 10(2):85–91, 2006.

[14] G. E. Elsinga, F. Scarano, B. Wieneke, and B. W. Van Oudheusden. Tomographic particle image velocimetry. *Experiments in Fluids*, 41(6):933–947, 2006.

[15] M. E. Erengil and D. S. Dolling. Physical causes of separation shock unsteadiness in shock wave/turbulent boundary layer interactions. *AIAA*, (3134), 1993.

[16] C. Ford and H. Babinsky. Micro-ramp control for oblique shock wave / boundary layer interactions. *Collection of Technical Papers - 37th AIAA Fluid Dynamics Conference*, 2:972–985, 2007.

[17] B. Ganapathisubramani, N. T. Clemens, and D. S. Dolling. Effects of upstream boundary layer on the unsteadiness of shock-induced separation. *Journal of Fluid Mechanics*, 585: 369–394, 2007.

[18] S. Ghosh, J. Choi, and J. R. Edwards. Numerical simulations of effects of micro vortex generators using immersed-boundary methods. *AIAA journal*, 48(1):92–103, 2010.

[19] R. H. M. Giepman, F. F. J. Schrijer, and B. W. Van Oudheusden. Flow control of an oblique shock wave reflection with micro-ramp vortex generators: Effects of location and size. *Physics of Fluids (1994-present)*, 26(6):066101, 2014.

[20] T. Herges, E. Kroeker, G. Elliott, and C. Dutton. Microramp flow control of normal shock/boundary-layer interactions. *AIAA journal*, 48(11):2529–2542, 2010.

[21] S. M. Hirt and B. H. Anderson. Experimental investigation of the application of microramp flow control to an oblique shock interaction. *47th AIAA Aerospace Sciences Meeting including the New Horizons Forum and Aerospace Exposition*, 2009.

[22] R. A. Humble, F. Scarano, and B. W. Van Oudheusden. Particle image velocimetry measurements of a shock wave/turbulent boundary layer interaction. *Experiments in Fluids*, 43(2-3):173–183, 2007.

[23] R. A. Humble, G. E. Elsinga, F. Scarano, and B. W. Van Oudheusden. Three-dimensional instantaneous structure of a shock wave/turbulent boundary layer interaction. *Journal of Fluid Mechanics*, 622:33–62, 2009.

[24] P. Klebanoff. *Characteristics of turbulence in a boundary layer with zero pressure gradient*. National Advisory Committee for Aeronautics, 1955.

[25] D. M. Kuehn. Experimental investigation of the pressure rise required for the incipient separation of turbulent boundary layers in two-dimensional supersonic flow. *NASA*, (19980230682), 1959.

[26] Q. Li and C. Liu. Les for supersonic ramp control flow using mvg at m= 2.5 and reθ= 1440. *AIAA paper*, 592(2010):17, 2010.

[27] H. W. Liepmann and A. Roshko. *Elements of gasdynamics*. Courier Corporation, 1957.

[28] F. Lu, A. Pierce, Y. Shin, C. Liu, and Q. Li. Experimental and numerical study of flow topology past micro vortex generators. *40th AIAA Fluid Dynamics Conference*, 2010.

[29] M. V. Morkovin. *Effects of compressibility on turbulent flows.* 1960.

[30] S. K. Norfleet. An evaluation of wall effects on stack flow velocities and related overestimation bias in epaâĂŹs stack flow reference methods. In *1998 EPRI CEM Users Group Meeting, New Orleans, Louisiana*, 1998.

[31] A. E. Perry and H. Hornung. Some aspects of three-dimensional separation. ii-vortex skeletons. *Zeitschrift fur Flugwissenschaften und Weltraumforschung*, 8:155–160, 1984.

[32] S. Pirozzoli, J. Larsson, J. W. Nichols, M. Bernardini, B. E. Morgan, and S. K. Lele. Analysis of unsteady effects in shock/boundary layer interactions. *Annu. Res. Briefs*, pages 153–164, 2010.

[33] D. M. Rao and T. T. Kariya. Boundary-layer submerged vortex generators for separation control-an exploratory study. In *AIAA*, volume 1, pages 839–846, 1988.

[34] M. R. Saad, H. Zare-Behtash, A. Che-Idris, and K. Kontis. Micro-ramps for hypersonic flow control. *Micromachines*, 3(2):364–378, 2012.

[35] F. Scarano. Tomographic piv: principles and practice. *Measurement Science and Technology*, 24(1):012001, 2013.

[36] F. Scarano and L. M. Riethmuller. Advances in iterative multigrid piv image processing. *Experiments in Fluids*, 29(1):S051–S060.

[37] H. Schlichting and K. Gersten. *Boundary-layer theory.* Springer Science & Business Media, 2003.

[38] J. Seddon and E. L. Goldsmith. *Intake aerodynamics.* 2nd ed, Blackwell Science, Boston, 1999.

[39] G. S. Settles. *Schlieren and shadowgraph techniques.* Springer, 2001.

[40] E. F. Spina, J. F. Donovan, and A. J. Smits. On the structure of high-reynolds-number supersonic turbulent boundary layers. *Journal of Fluid Mechanics*, 222:293–327, 1991.

[41] Z. Sun. *Micro Ramps in Supersonic Turbulent Boundary Layers: An experimental and numerical study.* PhD thesis, Delft University of Technology, 2014.

[42] Z. Sun, F. F. J. Schrijer, F. Scarano, and B. W. Van Oudheusden. The three-dimensional flow organization past a micro-ramp in a supersonic boundary layer. *Physics of Fluids (1994-present)*, 24(5):055105, 2012.

[43] N. Titchener and H. Babinsky. A review of the use of vortex generators for mitigating shock-induced separation. *Shock Waves*, pages 1–22, 2015. ISSN 0938-1287.

[44] O. Unalmis and D. Dolling. Decay of wall pressure field and structure of a mach 5 adiabatic turbulent boundary layer. *AIAA paper*, (94-2363), 1994.

[45] O. Unalmis and D. S. Dolling. Experimental study of causes of unsteadiness of shock-induced turbulent separation. *AIAA journal*, 36(3):371–378, 1998.

[46] F. M. White and I. Corfield. *Viscous fluid flow*, volume 3. McGraw-Hill New York, 2006.

[47] B. Wieneke. Volume self-calibration for 3d particle image velocimetry. *Experiments in fluids*, 45(4):549–556, 2008.

[48] Y. Yan and C. Liu. Further investigation on the physics of shock-wave vortex interaction in mvg controlled ramp flow. pages 2013–0401, 2013.

Appendix A

Seeding considerations for Tomographic-PIV

For successful implementation of tomographic-PIV a homogeneous seeding level is required in the test section. This appendix provides a detail of the steps carried out to obtain a uniform seeding distribution, optimal seeding concentration and illumination for the tomographic-PIV experiments.

A.1 Background

Before the commencement of this thesis project, the seeding particles were distributed from the seeding generator into the wind tunnel by a simple seeding tube of circular cross-section. This seeding tube consisted of 3 circular holes as shown in figure (A.1). From previous PIV experiments performed using this seeding tube, fluctuating seeding distribution was recorded in the test section. The test section exhibited fluctuating seeding due to the shedding of a Kármán vortex street from the seeding tube, which leads to correlational errors in PIV.

To address the issue of fluctuating seeding in the test section, before the commencement of the tomographic-PIV experiments, a new seeding rake was designed and manufactured at the High speed laboratory. The key factors based on which the seeding rake was designed are discussed in the following sections.

A.2 Seeding Distribution Rake

The basic requirement of a seeding distribution device or system in PIV is that it should provide a homogeneous seeding level in the flow. Additionally, the introduction of such a distribution device should not perturb the flow in the wind tunnel.

1. The dimensions of the new seeding rake were determined based on the seeded volume required in the test section which was $40 \times 40 \times 40\text{mm}^3$. Using the contraction ratio, the size of the seeding rake was determined to be $185 \times 185\text{mm}^2$.

2. The seeding rake consisted of 6 vertical bars with 6 orifices each. For each of the bars of the rake, an airfoil type cross section was selected. This was to ensure attached flow over the bars.

3. The size of the orifices was determined based on the condition that the total area of outflow from the orifices on the rake remains equal to the area of inflow into it. Based on this requirement, the seeding rake consists of 36 circular orifices of 1.3mm diameter each.

4. Due to density variations in the boundary layer, there is inhomogeneous seeding close to the test section wall. To improve the seeding close to the wall, the rake was mounted as close to the floor of the settling chamber as possible. The rake was mounted at the bottom of the settling chamber by using a connecting rod and is shown in figure (A.2).

Figure A.1: Seeding tube used earlier as the seeding distribution device

Figure A.2: Seeding Rake mounted inside the settling chamber of ST-15 wind tunnel.

A.3 Optimization Experiments

Preliminary experiments were conducted using the tracer particles of DEHS and TiO_2, different laser power and seeding generator power (number of nozzles used). These experiments were performed using the seeding tube and the seeding rake. For the TiO_2 experiments, a customized cyclone type seeding generator constructed at TU Delft was used. The test matrix for this optimization study is shown in table (A.1).

Expt no	Seeding					Laser Power	
	Distribution system	Access Port Location	Particles	Seeding Power	Inlet pressure in kPa	Pulse A	Pulse B
1	None: Seeding generator directly connected to access port	Settling chamber	DEHS	Full	3.2	35%	20%
2	Seeding Tube	Settling chamber	DEHS	Half	4.2		
3			DEHS	Half	3.2		
4		Upstream	DEHS	Half	3.2		
5		Upstream	DEHS	Full	3.2		
6		Downstream of the meshes	DEHS	Half	3.2	55%	-
7	Seeding Rake	Settling chamber	DEHS	Half	3.2	35%	20%
8			DEHS	Half	3.2	55%	12%
9			TiO_2	Half	5 with Bypass 4	55%	40%
10			TiO_2	Half	4	40%	40%
11			TiO_2	Half	3.2		
12			DEHS	Half	3.2	60%	48%

Table A.1: Test Matrix for seeding distribution optimization study

A.3.1 Observations from the Optimization experiments

In table (A.2) the main observations from the optimization experiments are noted down.

It is observed that with the seeding tube agglomeration or clumping of particles occurs in the test section. Physical flow features such as the vortical structures can be observed while using the seeding tube to distribute seeding particles. This can be seen in figure (A.3). With the seeding rake and DEHS as seeding, distinct particles are seen in test section. Compared to the seeding tube, more homogeneous seeding distribution is obtained by using the seeding rake as shown in figure (A.4).

Though DEHS particles are distinct, they are not very bright compared to the TiO_2 particles. However, TiO_2 particles show large amount of clumping which is undesirable. Further, TiO_2 particles necessitated cleaning of test section, optical windows of the tunnel and laser probe after every tunnel run which adds to the experimental time and complexity.

Therefore DEHS particles were chosen as suitable seeding particles and the laser was operated with 100% illumination of both pulses during the experimental campaign.

Expt No	Seeding Distribution System	Observations
1	None: Seeding generator directly connected to access port	Very poor seeding concentration
2	Seeding Tube	Poor illumination, Agglomeration or clumping of particles leading to non-uniform seeding.Flow features are clearly seen.
3		
4		
5		
6		
7	Seeding Rake	Distinct particles with no agglomeration. Poor illumination and particles are not very bright.
8		No improvement in brightness of particles with increased laser power. Hence TiO_2 used in the next experiment.
9		Too many particles with too much agglomeration.
10		Too much agglomeration of particles and hence non uniform seeding
11		
12		Distinct particles and uniform seeding. However, particles are less bright compared to TiO_2.Hence laser pulse power set to 100% with full seeder power for the experimental campaign.

Table A.2: Observations from optimization experiments

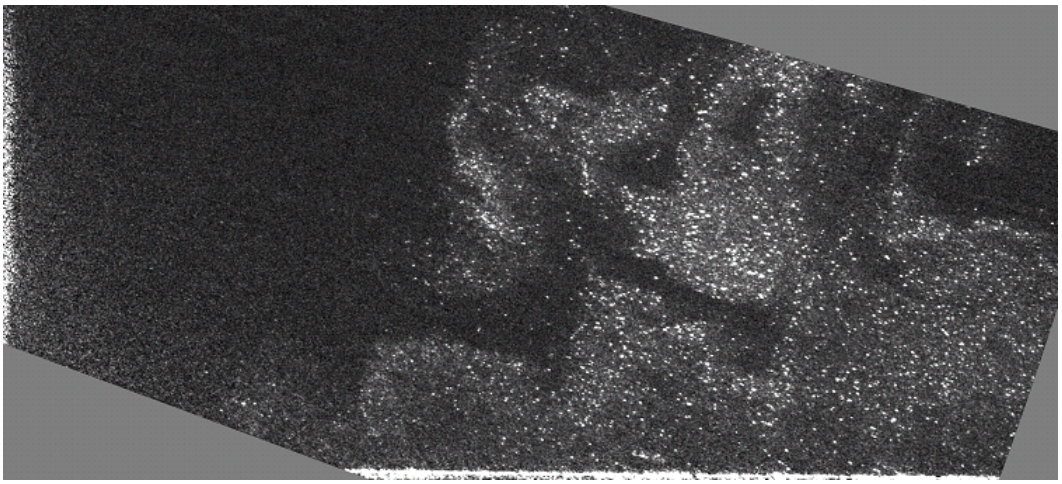

Figure A.3: Seeding distribution in the test section obtained by using the seeding tube mounted in the settling chamber, DEHS particles and both laser pulses at 100% power.

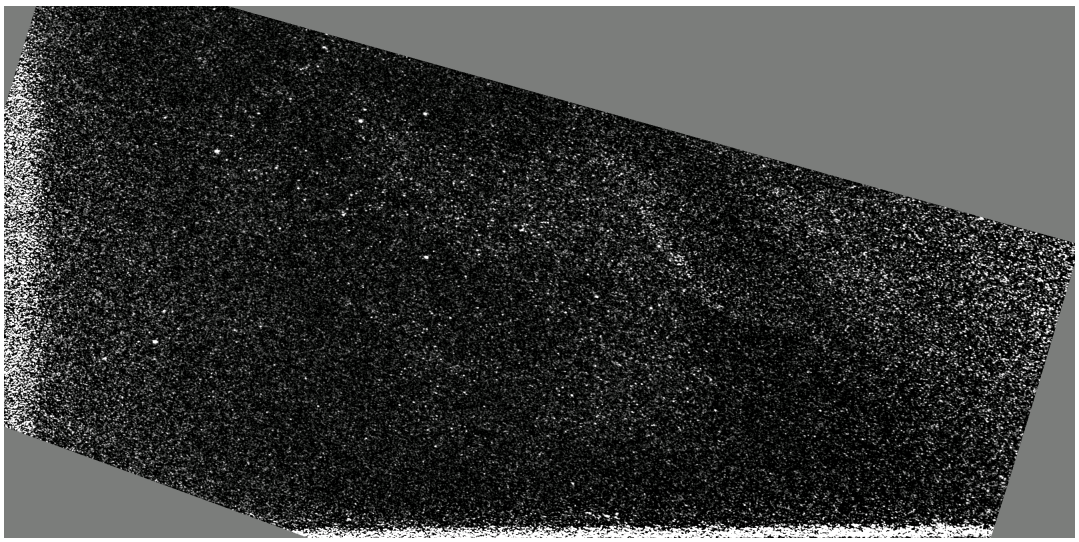

Figure A.4: Seeding distribution in the test section obtained by using the seeding rake mounted in the settling chamber, DEHS particles and both laser pulses 100% power.

Appendix B

Tomographic-PIV: Data reduction

This appendix details the steps carried out for the tomo-PIV data reduction. The data reduction procedure required several trials with different processing settings for validation with respect to the literature. The exact steps undertaken for image pre-processing, reconstruction and correlation are discussed in section (B.1), (B.2) and (B.3) respectively.

B.1 Image pre-processing

Image pre-processing forms an important and necessary step in tomo-PIV especially because of the sensitivity of the reconstruction technique to the background light intensity [14]. Image pre-processing was performed using the filters available in the DaVis 8.1.6 software.

- As a first step before volume-self calibration, the average minimum intensity was subtracted from all images to reduce the background noise.
- To further reduce the image background noise, 'subtract sliding minimum' filter was used with a small local region of 31 pixels.
- Further, it is important to have uniform particle image intensity throughout a particular image and between images from different cameras. This was achieved by normalization of the particle intensity on a larger scale using the 'normalize with local average' filter.
- Finally, a constant 40 counts was subtracted from every pixel using the 'subtract constant from each pixel' filter. This was used to obtain pixels with sufficient zero counts.

The images obtained after the above mentioned steps were used for the volume self-calibration procedure. The volume self-calibration procedure was performed to correct the calibration

mapping function for any misalignments or vibration of cameras. The self-calibration procedure was performed for a volume of smaller dimensions than the actual illuminated volume. By doing so, the bad vectors outside the actual volume are eliminated while obtaining the corrected mapping function.

After the volume self-calibration was performed, the corrected mapping function was obtained for all the cameras. The images processed as per the previous steps, were further processed for the reconstruction and correlation as following:

- A Gaussian smoothing filter with a 3×3 kernel was used to further improve the particle images.
- Finally, each pixel was multiplied with a constant factor of 10.

The typical image obtained after the above mentioned pre-processing steps is shown in figure (B.1b). The raw image with no pre-processing is also shown in figure (B.1a) for comparison. The advantage of pre-processing is seen clearly, the pre-processed image is cleaner compared to the raw image.

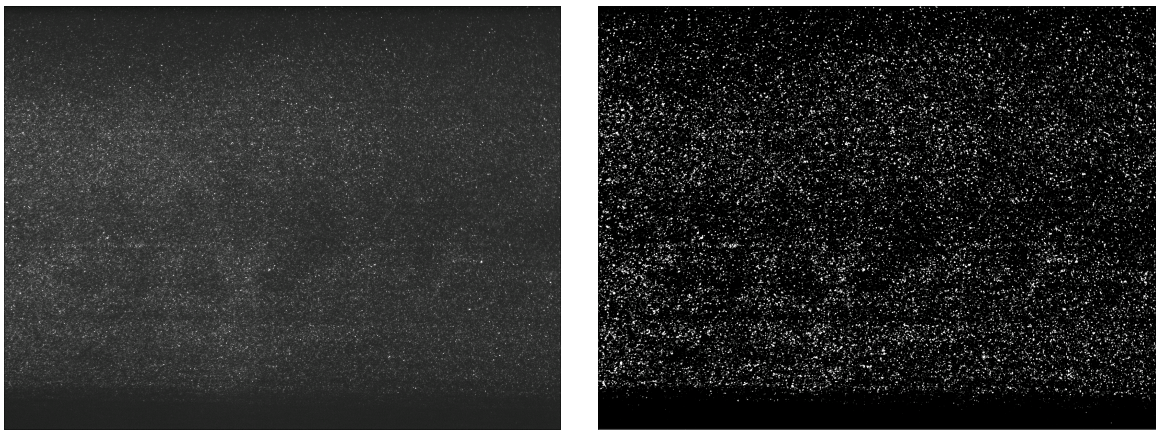

(a) PIV image before pre-processing (b) PIV image after pre-processing

Figure B.1: Effect of image pre-processing

B.2 Volume Reconstruction

For the volume reconstruction, the 'fastMART' option in DaVis 8.1.6. was used. The dimensions of the reconstructed volume are slightly larger than the dimensions used for self-calibration. This is to ensure that the entire volume has been reconstructed.

To determine the reconstruction quality, the laser sheet intensity distribution is visualized along the wall normal direction. A typical laser sheet intensity distribution obtained after

volume self-calibration, for the present study is shown in figure (B.2). The red curve is the intensity profile of the first laser pulse and the green curve is the intensity profile of the second laser pulse. In figure (B.2), the illuminated volume range is from Z = −5.5 and Z = 6. The

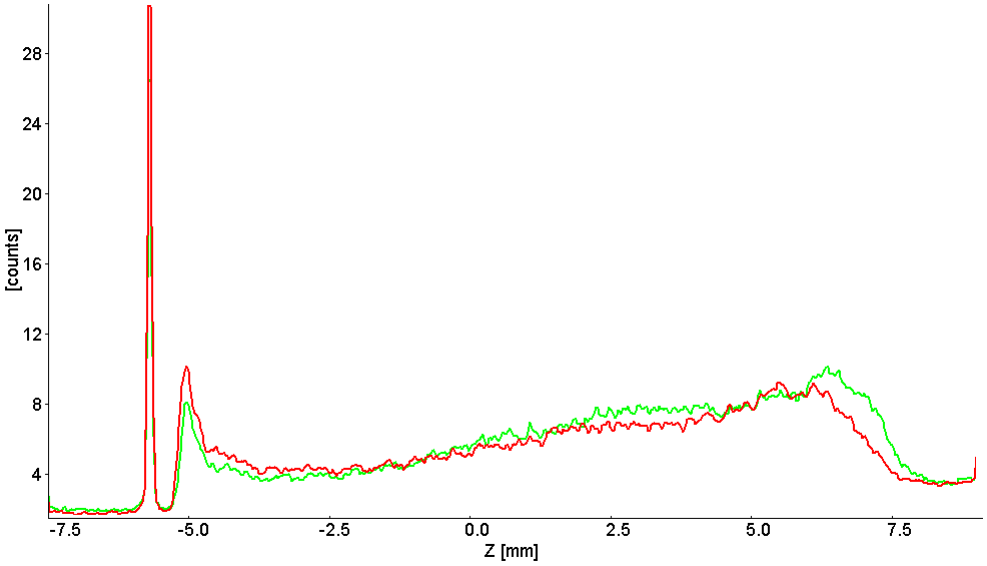

Figure B.2: A typical Laser intensity profile obtained after volume self-calibration.

wall is located at Z = -5.5 which is marked by a drop in the laser intensity. The end of the volume is also marked by a drop in the laser intensity which is recorded at Z = 6. The strong peak in intensity recorded at Z ≈ −6 is an artefact of the reconstruction at the boundary of the volume.

Further, it is observed that close to the wall, the laser intensity is slightly lower compared to the end of the volume. Close to the boundary layer, the density is lower due to which the seeding density close to the wall is also lower. Hence the amount of laser light scattered is lower which is recorded as reduced laser intensity close to the wall in figure (B.2).

The intensity inside the illuminated volume is due to real reconstructed particles and false particles called as ghost particles. The ghost particles arise due to [35]. The intensity outside the volume is purely due to the ghost particles. The reconstruction signal to noise ratio (SNR) is defined as the ratio of the mean intensity inside the illuminated volume to the mean intensity outside the volume. According to Scarano [35] a SNR ≥2 is required for an acceptable reconstruction and a robust correlation. For the present case:

$$\mathrm{SNR} = \frac{7\mathrm{counts}}{3\mathrm{counts}} = 2.33 \tag{B.1}$$

Therefore, the reconstruction quality for the present study is considered acceptable.

B.3 Correlation

The reconstructed volume is divided into a number of smaller sub-volumes called as interrogation volumes, and the process of three dimensional cross correlation is applied to the sub-volumes.

For the correlation of reconstructed volumes, the 'Direct correlation' option in DaVis 8.1.6 was used. The iterative multi-step window approach of Scarano and Riethmuller [36] was used for the correlation. For the first iteration, an interrogation window of size 128 voxel^3 was chosen to capture the large displacements. The interrogation window size was gradually reduced and the final interrogation window size was 48 voxel^3 used. All the steps were performed with a 75% overlap. An example of the DaVis correlation settings is shown in figure (B.3).

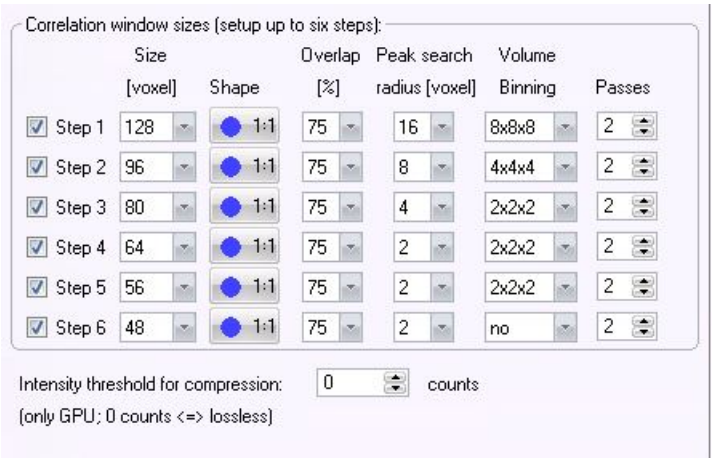

Figure B.3: DaVis settings for correlation

Appendix C

Tomographic-PIV: Validation

To be able to successfully study the separation behaviour of the micro-ramp controlled interaction, it is first important to validate the mean streamwise velocity profiles with the literature. In this appendix the velocity profiles from the present tomo-PIV study for both the uncontrolled interaction and micro-ramp controlled interaction are compared with velocity profiles from Giepman et al. [19] who performed planar-PIV experiments for the same flow conditions. The velocity profiles for the uncontrolled and the micro-ramp controlled interaction are shown in section (C.1) and section (C.2) respectively.

C.1 Mean Velocity profiles for the uncontrolled interaction

Figure (C.1) shows the velocity profiles for the uncontrolled interaction at different streamwise stations, beginning from $x/\delta = -6.2$ to the end of the measurement volume at $x/\delta = -0.02$. It can be seen from this figure that the velocity profiles from tomo-PIV are in very good agreement with the planar-PIV results in the entire measurement region.

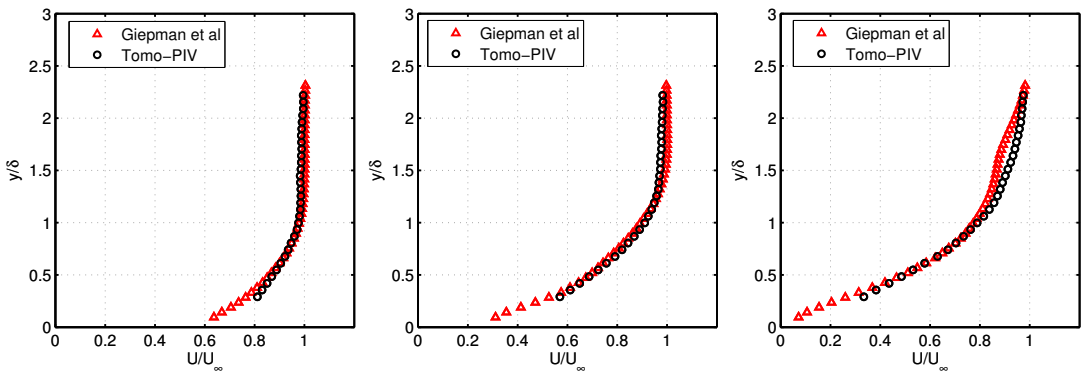

(a) $x/\delta = -6.2$ (b) $x/\delta = -5$ (c) $x/\delta = -4$

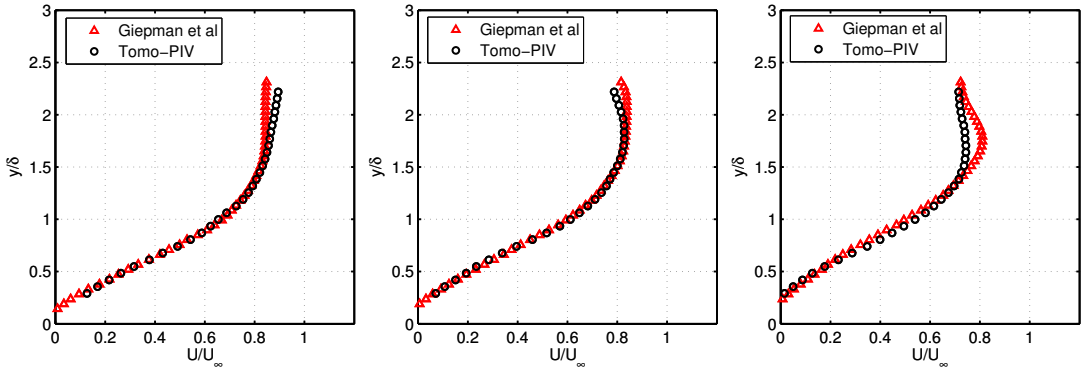

(d) $x/\delta = -3$ (e) $x/\delta = -2.5$ (f) $x/\delta = -2$

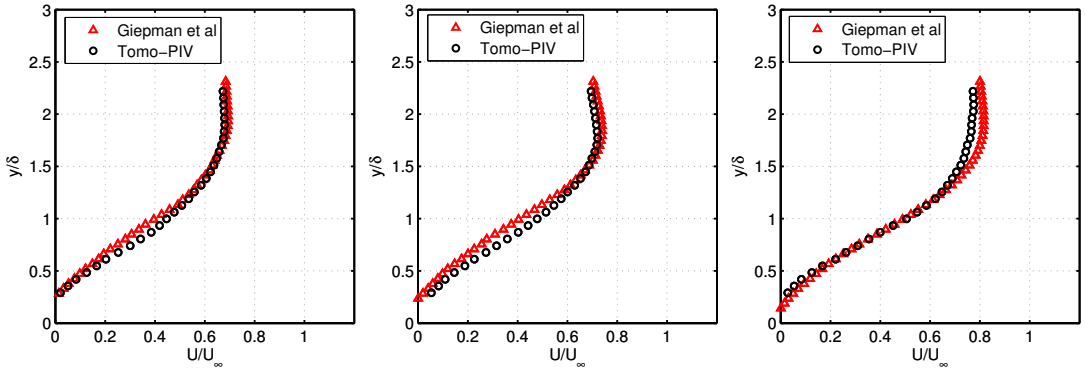

(g) $x/\delta = -1.5$ (h) $x/\delta = -1$ (i) $x/\delta = -0.02$

Figure C.1: Streamwise velocity U/U_∞ profiles at $z/\delta = 0$ with the planar-PIV velocity results of Giepman et al. [19].

C.2 Mean Velocity profiles for Micro-ramp controlled interaction

The mean streamwise velocity profiles for the micro-ramp controlled interaction from the present tomo-PIV investigation are compared to the planar-PIV results of Giepman et al. [19] in figure (C.2). In general all the velocity profiles are in good agreement with the planar-IV results. The velocity profiles at the beginning of the measurement volume in figure (C.2a-c) are in better agreement with the planar-PIV results, than the velocity profiles further downstream.

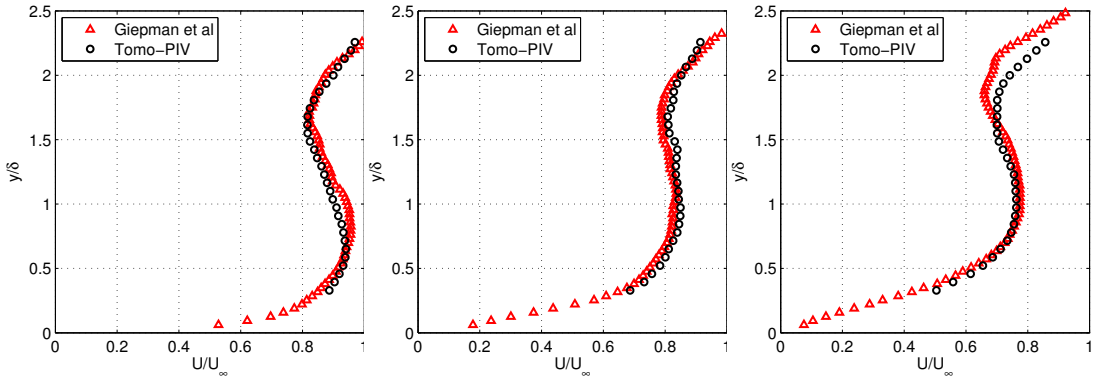

(a) $x/\delta = -6.2$ (b) $x/\delta = -5$ (c) $x/\delta = -4$

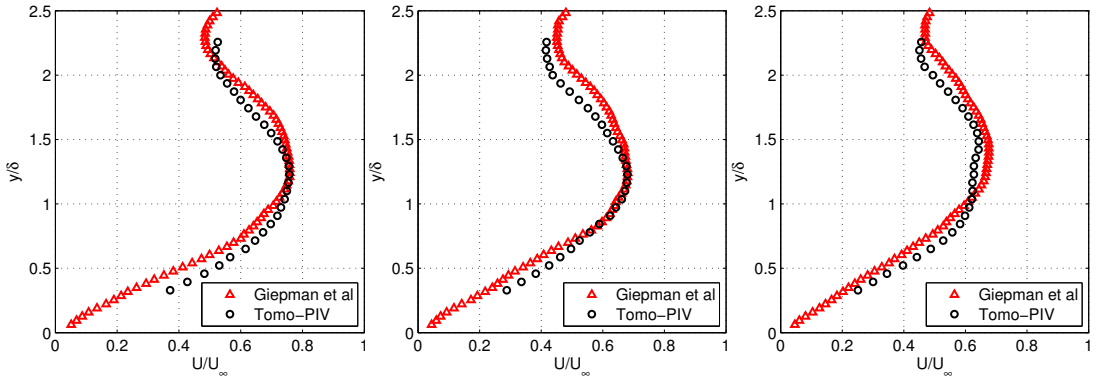

(d) $x/\delta = -3$ (e) $x/\delta = -2.5$ (f) $x/\delta = -2$

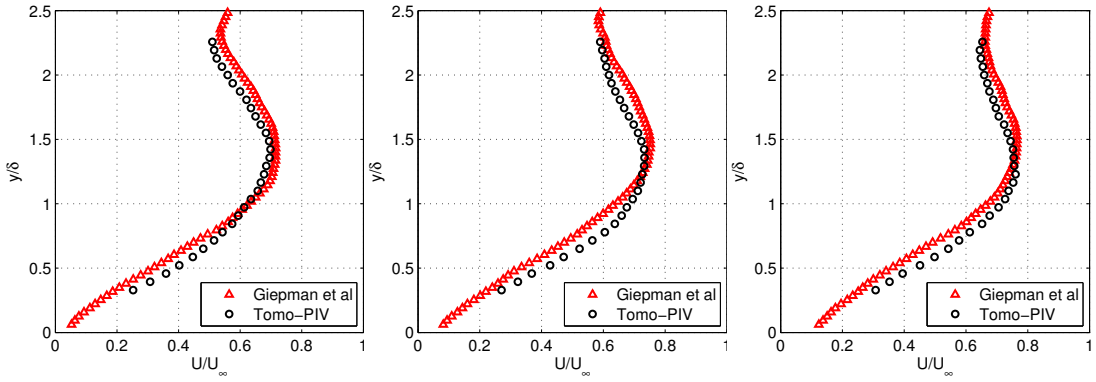

(g) $x/\delta = -1.5$ (h) $x/\delta = -1$ (i) $x/\delta = -0.02$

Figure C.2: Streamwise mean velocity profiles U/U_∞ at $z/\delta = 0$ with planar-PIV velocity results of Giepman et al. [19]. Micro-ramp h = 3mm placed at $x_{MR} = -17.3\delta$